

Micromachined On-Wafer Probes for Characterization of Terahertz Devices and Circuits

A Dissertation

Presented to
the faculty of the School of Engineering and Applied Science
University of Virginia

in partial fulfillment
of the requirements for the degree

Doctor of Philosophy

by

Matthew Bauwens

August

2014

APPROVAL SHEET

The dissertation
is submitted in partial fulfillment of the requirements
for the degree of
Doctor of Philosophy

Matthew F. Bauwens

AUTHOR

The dissertation has been read and approved by the examining committee:

Dr. Robert M. Weikle, II

Advisor

Dr. N. Scott Barker

Dr. James M. Fitz-Gerald

Dr. Avik Ghosh

Dr. Lloyd R. Harriott

Accepted for the School of Engineering and Applied Science:



Dean, School of Engineering and Applied Science

August
2014

To

Megan

Acknowledgments

- I would like to first thank my advisor, Bobby Weikle, not only for his support and patience over the years, but also for his outstanding teaching. His microwave engineering class is the origin of my interest in this field, which set me on the path that led to this work.
- I would like to thank Scott Barker and Art Lichtenberger for countless helpful discussions throughout the entirety of this work.
- I am especially appreciative of the hard work of Chunhu Zhang and Naser Alijabbari in the development and implementation of fabrication processes that made this work possible.
- I would like to thank Acar Isin for his company in the FIR lab throughout the many hours of testing, and for his generous time and effort machining the many miscellaneous parts and fixtures needed for experiments throughout this work.
- I would like to thank the developers of scikit-`rf` for providing an incredibly useful tool that has saved innumerable hours of my time.
- Finally, I would like to thank my family and friends. The time spent with you outside of the lab has been an invaluable part of this journey.

Abstract

The terahertz frequency spectrum (300 GHz - 3 THz) is recognized as a potential tool for many applications, and the development of terahertz integrated circuits promises to unlock this potential. However, the on-wafer measurement infrastructure necessary to accurately characterize integrated circuits and devices in the terahertz regime is largely undeveloped. In addressing this need, the recent development of the micromachined on-wafer probe represented a turning point, establishing a foundation for terahertz on-wafer measurement infrastructure.

In this work, improvements to the micromachined probe design are developed to provide more robust and reliable electrical and mechanical performance. Additionally, the design of a new micromachined probe housing enables increased overall performance of the on-wafer measurement system.

To address emerging measurement needs in the terahertz range, the second part of this work presents the design and characterization of micromachined on-wafer probes for the WR-1.2 (600 - 900 GHz) and WR-1.0 (750 GHz - 1.1 THz) waveguide bands. These designs enable on-wafer measurement capabilities of devices and circuits to 1.1 THz for the first time.

Contents

1	Introduction	1
1.1	On-Wafer Measurements	2
1.2	Micromachined Probes	4
1.2.1	Origin	4
1.2.2	Architecture	5
1.3	Outline of the Thesis	8
2	Robustness and Engineering of Micromachined On-Wafer Probes	10
2.1	Probe Chip Clamping	11
2.2	Oxidation of Probe Housing	15
2.3	Fracturing of the Silicon Substrate	21
2.4	Tip Metallization and Probe Contact Resistance	25
2.5	Improved Probe Housing Architecture	32
2.6	Conclusion	37
3	Design and Characterization of WR-1.2 Micromachined Probes	39
3.1	RF Channel Considerations	40
3.2	Mechanical Design Considerations	42
3.3	Mechanical Simulations	47

3.4	RF Design	51
3.5	Mechanical Characterization	57
3.6	Mechanical Failure	58
3.7	RF Characterization	61
3.8	Conclusion	66
4	Design, Characterization, and Application of	
	WR-1.0 Micromachined Probes	67
4.1	Thin Silicon Drawbacks	68
4.2	RF Channel Design	70
4.3	Bias Filter Design	74
4.4	Waveguide to Coaxial Transition	77
	4.4.1 Backshort Analysis	79
	4.4.2 Capacitive Step Analysis	81
4.5	Coaxial to CPW Transition	85
4.6	Full Simulation	88
4.7	RF Characterization	89
4.8	Diode Characterization	91
4.9	Full Two-Port Calibration	92
4.10	Conclusion	97
5	Conclusion	98
	Bibliography	105
	List of Publications	114
A	WR-1.2 Probe Housing Mechanical Drawings	116

B WR-1.0 Probe Housing Mechanical Drawings	129
C WR-1.0-Microstrip-Design	145

Chapter 1

Introduction

The terahertz frequency spectrum (300-3000 GHz) has been a subject of scientific research for many decades and the unique properties of radiation in this regime provide vast amounts of information in areas such as spectroscopy and radio astronomy [1]. It has also been recognized that the spectrum could potentially be used as a tool for many new and exciting applications. For example, its non-ionizing photon energy and sensitivity to water concentration make the terahertz spectrum an appealing choice for medical imaging of skin irregularities such as burn wounds or cancerous tissue [2]. In addition, its transmissivity through common materials such as clothing could make it suitable for security imaging applications [3]. Many of these applications have yet to come to fruition, however, as the spectrum lies between the traditional electronic and photonics regions making it difficult to create devices for sources and detectors. As a result, the technology to utilize the terahertz spectrum is relatively immature. Nevertheless, recent progress in the fabrication of high-frequency transistors has enabled the development of terahertz monolithic integrated circuits (TMICs) [4–6] that could open the door to many such applications, and terahertz on-wafer probes facilitate that progress.

1.1 On-Wafer Measurements

Over the past 30 years, on-wafer probes have been vitally important for the RF community by dramatically reducing the time and cost to develop new products [9]. Because the calibration reference planes can be placed on-wafer close to the device-under-test (DUT), it is possible to measure the true characteristics of the device itself. In the development stages, on-wafer probes enable accurate validation of models, while on the production line, they enable identification of good die or performance-based sorting prior to packaging.

The frequency range of these probes were limited to 60 GHz by the coaxial input connector until the invention of waveguide input probes in the early 1990s. Prior to the development of micromachined probes, there were only two sources of waveguide-based probes. Examples of current models from each are shown in Fig. 1.1. The Infinity Probe® from Cascade Microtech [11] and the Picoprobe® from GGB Industries, Inc. [12] are similar in the sense that they both use a small, semi-rigid coaxial cable to carry the electromagnetic signal from the waveguide to the probe tips. However, the nature of the probe tips themselves are quite different. For the Infinity, a photolithographically-defined membrane is attached to the end of the coaxial cable. With the Picoprobe, the center conductor of the coaxial cable is shaped to form the center contact, while metal blades are attached to the coaxial outer conductor to form the ground contacts. In both cases, grinding, gluing and/or soldering are required to mount the coaxial cable in the waveguide and to form the tips. The limited precision of these types of processes makes it difficult to scale these technologies to higher frequencies, where variations and tolerances have an increasing detrimental effect.

As a result, research on submillimeter-wave devices and circuits has largely relied

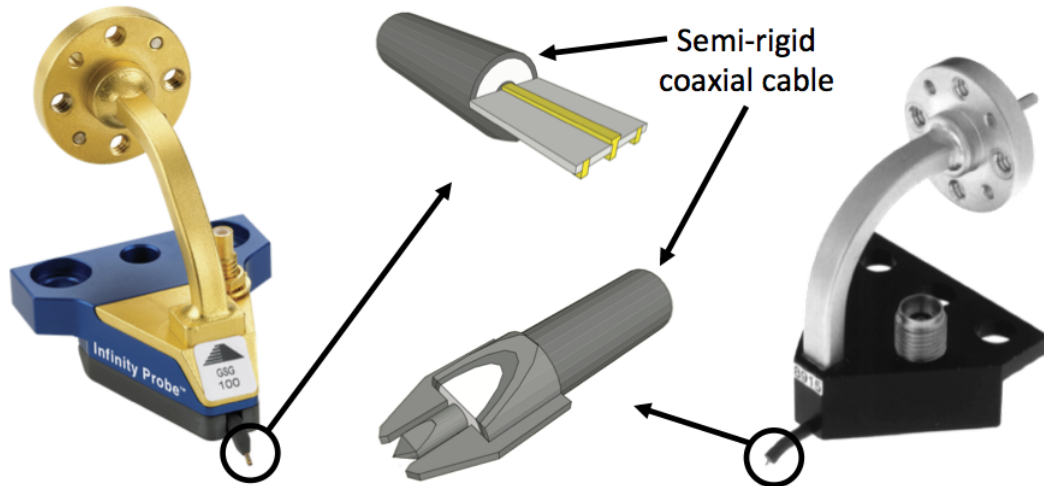


Figure 1.1: Conventional waveguide probe architectures. Left: the Cascade Microtech Infinity Probe®[®], right: the GGB Industries, Inc. Picoprobe®[®]. Images from: [7–9].

on other testing methods, commonly through quasi-optical coupling using antennas or packaging into a test fixture with waveguide flanges in order to interface with test equipment. An illustrative example of a waveguide packaging from the work reported in [10] is shown in Fig. 1.2, where an integrated circuit is mounted, utilizing waveguide probes to couple the RF signal to and from the waveguide channel and wirebonds to circuit traces provide DC bias. A “thru” structure with no active circuitry is also measured to estimate the effects of the waveguide transitions on the native performance of the actual circuit. While this is certainly a practical solution, at submillimeter-wave frequencies there is significant uncertainty and error in such measurements due to limited precision of the test fixtures and assembly process. In addition, the mounting process is difficult, time consuming, and may not permit non-destructive disassembly of the circuit and housing. On-wafer probing is therefore the preferred measurement technique.

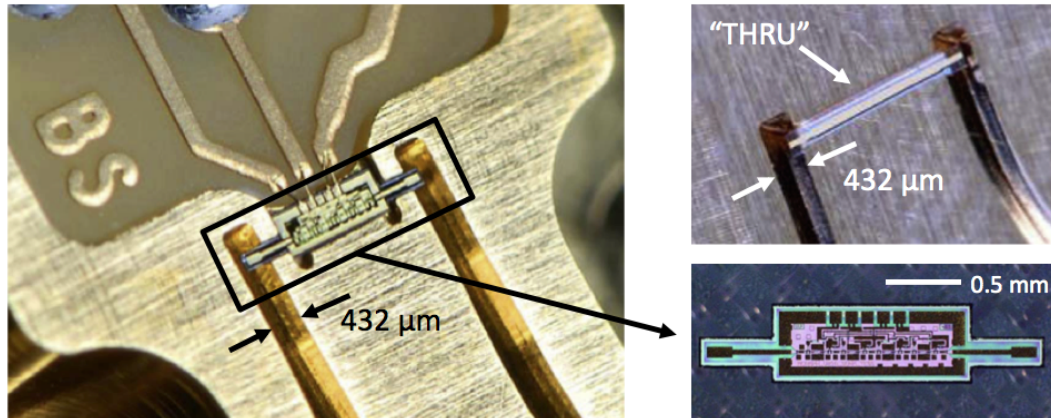


Figure 1.2: Waveguide packaging of submillimeter-wave integrated circuit [10]. Left: the integrated circuit is fixed in place between the input and output waveguide channels and wirebonds to circuit traces provide DC bias. Upper right: a “thru” structure used to estimate the native performance of the integrated circuit.

1.2 Micromachined Probes

This section provides a brief history of the origin and development of micromachined probes, followed by a general description of the micromachined probe architecture, which serves as a foundation for the work described in the rest of this thesis.

1.2.1 Origin

In 2009, Northrop Grumman awarded a subcontract to the University of Virginia to develop submillimeter-wave on-wafer probes in support of the DARPA THz Electronics Program, a three phase program which aimed to develop transistors at 670 GHz, 850 GHz, and 1.03 THz. The research performed at UVa resulted in the development of a new on-wafer probe technology, termed “micromachined probes.” In 2010, demonstration of the micromachined probe was first reported as a proof-of-concept operating in the WR-10 waveguide band (75 - 110 GHz), with performance comparable to existing commercial probes [13]. However, in contrast with existing commercial probes, the design of the micromachined probe is more suitable

for application at submillimeter-wave frequencies. In 2011, a micromachined probe design was implemented and demonstrated in the WR-1.5 waveguide band (500 - 750 GHz) [14, 15], where, at the time, there was no on-wafer measurement infrastructure. That work resulted in the first on-wafer measurements above 500 GHz, including, for example, Northrop Grumman's demonstration of a low-noise amplifier with peak gain of 30 dB at 670 GHz [5]. In 2011, Dominion MicroProbes, Inc., a UVa spin-off company, was founded to make the WR-1.5 probes commercially available.

1.2.2 Architecture

The micromachined probe consists of two parts: a machined E-plane split-block waveguide housing, and a micromachined thin silicon probe chip, as shown in Fig. 1.3. As noted in [13], the microfabrication process for the probe chips builds on the ultra-thin silicon process originally described in [16] and incorporates metalized vias, patterned frontside and backside metallization, and frontside metal beamleads that extend beyond the edge of the silicon, and a silicon substrate of semi-arbitrary shape. With this process, all of the necessary probe circuitry – the waveguide transition, intermediate transmission line, GSG contacts, and DC bias tee – are lithographically-defined and integrated onto this single chip. This precision and integration provides a significant advantage over other contact probe architectures, which often involve processes such as grinding, soldering, and gluing to connect parts of the probe circuitry. In addition, use of high-resistivity silicon ($> 10 \text{ k}\Omega \cdot \text{cm}$) enables low-loss transmission lines, while its high modulus of resilience of 55 MJ/m^3 and yield strength of 5 GPa [17] make it a robust mechanical material.

The waveguide housing is machined from aluminum using a conventional preci-

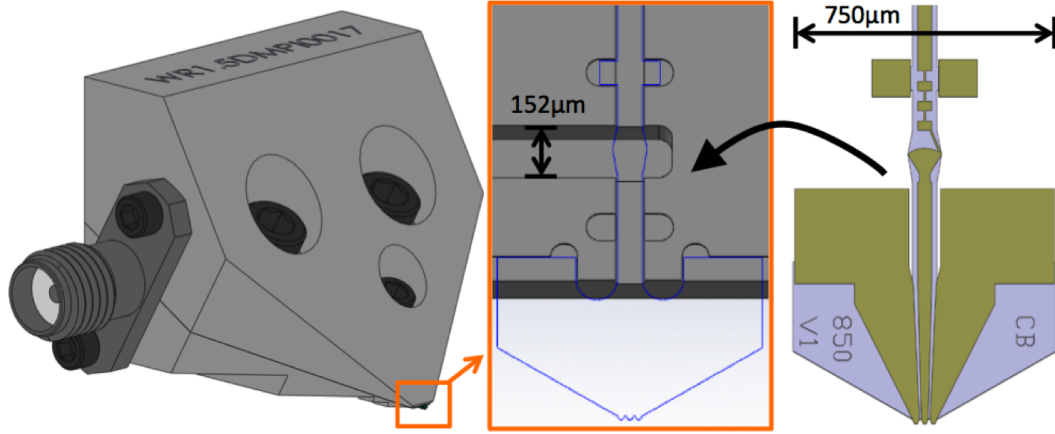


Figure 1.3: Micromachined probe concept (WR-1.2 as shown). Left: machined E-plane split-block waveguide housing. The SMA connector on the left side of the housing allows application of DC bias at the probe tips. Right: micromachined probe chip.

sion computer numerical control (CNC) milling process that allows tolerances down to $\pm 2.5 \mu\text{m}$. The back face of the probe housing features a precision UG-387 rectangular waveguide interface that allows the probe to be connected to waveguide-based sources and receivers. The rectangular waveguide channel carries the RF signal from the interface down to the tip of the housing. Near the tip, there are milled recessions surrounding the waveguide, the dimensions of which match the probe chip geometry, as shown in Fig. 1.3. These recessions serve two purposes: self-alignment and clamping. Because the shape of the silicon matches the shape of the milled recessions, the probe chip “drops in” place, self-aligning the probe chip to the rectangular waveguide channel. After the chip is mounted in the recessions, the halves of the waveguide housing can be mated together, clamping the chip in place. This clamping avoids the need for adhesives and also means the probe can be easily repaired many times if necessary by simply opening the housing and replacing the tip.

In order to make contact with an on-wafer device, the probe chip extends below

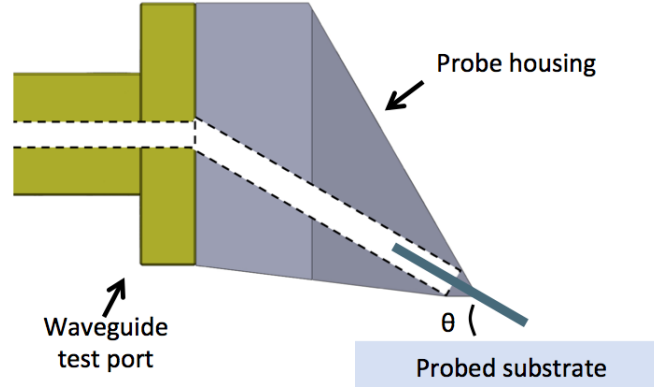


Figure 1.4: The split angle of the waveguide housing affects the coupling into the probe, the available force at the tip, and the coupling to on-wafer circuits.

the bottom of the waveguide housing, as shown in Fig. 1.4. With the probe chip clamped in place, the tip constitutes a cantilever beam, and as the tip is brought into contact with the test wafer, it deflects and generates a force at the contact points, enabling a low-resistance connection ($< 0.1 \Omega$) to the device-under-test (DUT). The angle of the tip with respect to the probed substrate is set by the angle of the split-plane of the waveguide housing. To minimize machining complexity, the split-plane angle is fixed, and the waveguide is cut flush vertically to enable connection to other waveguide components. Choice of this angle has an effect on the discontinuity at the waveguide interface, the mechanical properties of the tip, and electromagnetic coupling from the probe tip to the on-wafer circuitry. Previous work has analyzed the tradeoffs between these aspects and shown that a split angle of 30° provides a reasonable balance [18, 19].

Referring to Fig. 1.5, the general electromagnetic operation of the probe can be described as follows. From the rear face of the housing, the rectangular waveguide channel follows the split plane to the tip of the housing, where after a 90° bend, it terminates in a fixed backshort. A radial stub suspended over the rectangular waveguide channel provides a broadband transition to an intermediate transmission

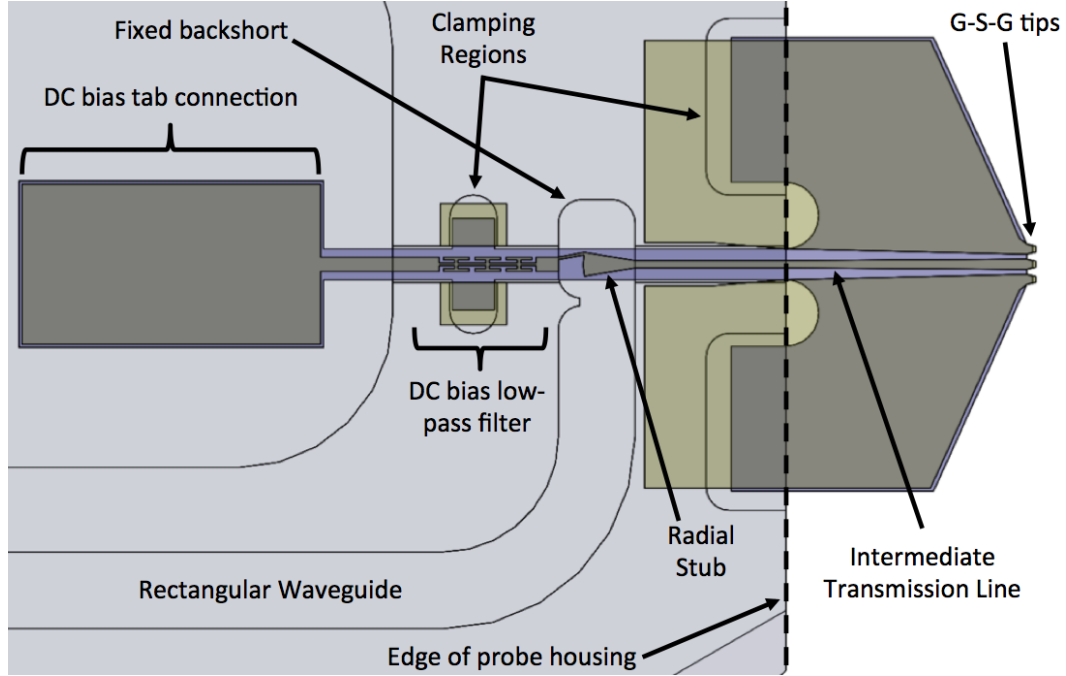


Figure 1.5: Illustration of probe chip mounted in waveguide housing.

line, which carries the electromagnetic signal to the ground-signal-ground (GSG) probe tips. To allow application of DC bias at the GSG tips, a large DC bias tab is connected to the radial stub through a low-pass filter. This filter provides isolation from the RF signal so that the DC connection does not affect the RF performance of the probe. The bias tab is connected to the center pin of an external coaxial connector, such as the SMA shown in Fig. 1.3.

1.3 Outline of the Thesis

The aim of this research twofold: 1) to address issues of concern in the prototype WR-1.5 micromachined probe design to improve robustness to a level competitive with existing probes, and 2) to develop a probe design to address emerging measurement needs in the terahertz range. The work performed in this thesis to achieve

these goals is divided into three parts:

1. Chapter 2 describes four newly-identified critical issues related to the robustness and reliability of micromachined probes. For each issue, the cause is determined and solutions are implemented and tested. Additionally, a new micromachined probe housing is developed to enable increased overall performance of the on-wafer measurement system.
2. Chapter 3 evaluates the feasibility of using thinner silicon substrates for micromachined probes by implementing a design for the WR-1.2 waveguide band (600 - 900 GHz) on 5 μm thick silicon.
3. Chapter 4 presents the design, characterization, and application of a micromachined probe for the WR-1.0 waveguide band (750 GHz - 1.1 THz), which enabled the first on-wafer measurements at 1 THz.
4. Chapter 5 summarizes the contributions of this thesis and offers recommendations for future work.

Chapter 2

Robustness and Engineering of Micromachined On-Wafer Probes

On-wafer probes must be reasonably rugged, robust, and reliable in their electrical and mechanical characteristics. To prove useful as a tool for submillimeter-wave metrology, the mechanical and electrical response of the probe must be repeatable as it makes direct physical contact with the on-wafer DUT. Moreover, the probe must remain rigidly clamped to the probe housing and the probe tips must survive repeated contact to a variety of metals while yielding a low contact resistance. Previously, work has been done to characterize the robustness of micromachined probes, which showed that the micromachined probe tips can sustain at least 20,000 contacts [20,21]. However, a number of other important issues regarding the robustness and reliability of micromachined probe have been previously unrecognized. These issues relate to the design, fabrication, and use of the probes and are therefore important considerations for all future design and use of micromachined probes. This work identifies four robustness issues relating to: clamping of the probe chip, oxidation of the probe housing, fracturing of the silicon substrate, and probe tip

metallization. The cause of each issue is determined and solutions are developed and tested.

2.1 Probe Chip Clamping

As previously described, to allow assembly of the micromachined probe without the need for adhesives, the micromachined probe tip is intended to be clamped in place between the two halves of the split block waveguide housing. When clamped, the tip constitutes a cantilever beam that generates contact force as designed, enabling repeatable, low-resistance contacts to the DUT. If the chip is not properly clamped, the vertical displacement of the probe tip, known as “overtravel,” required to reach a particular contact force could be excessive and could vary significantly between probes. In addition, if the chip is not properly clamped, it could move within the waveguide housing, perturbing the RF characteristics of the probe and potentially causing non-repeatable errors that could degrade measurement quality. Secure clamping of the tip is therefore required to provide consistent mechanical and electrical behavior.

While studying the mechanical properties of micromachined probes, it was observed that the tips exhibited a non-linear force-displacement curve at low overtravel, as shown in Fig. 2.1a. Beyond some overtravel threshold, typically 15-25 μm , the force-displacement would become linear. This “hinged” force-displacement curve was not expected based on mechanical simulations. After observing this effect repeatedly, it was thought that it may have been a result of a fault in the measurement setup. To verify the setup, the force-displacement test was repeated without the silicon probe tip present, with the load cell applying force to the probe housing instead. In that test, the force-displacement curve was linear, indicating that the

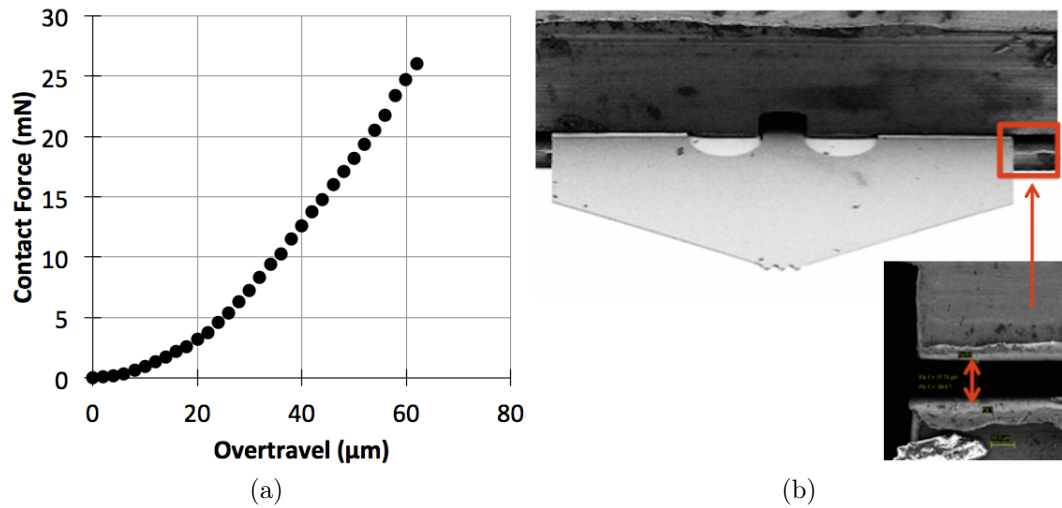


Figure 2.1: (a): “Hinged” force-displacement curve characteristic of poorly-clamped probe chips. (b): SEM image of assembled waveguide housing illustrating an $18 \mu\text{m}$ gap between the two halves of the housing near the clamping region.

hinged force-displacement curves were associated with the silicon probe tips.

To more closely examine the mounted probe chip, the tip of an assembled probe was inspected using scanning electron microscopy (SEM). As shown in Fig. 2.1b, the SEM revealed an $18 \mu\text{m}$ gap between the two halves of the waveguide housing that were expected to be flush. It was suspected that this gap was the cause of the “hinged” force-displacement curve, with the hypothesis being that when the chip is poorly clamped, it “pivots” on initial contact with a device until it eventually contacts the upper side of the block where it becomes secure and begins to deflect linearly with increasing overtravel distance. If we assume that the chip is clamped internally at the alignment tabs in the bias channel, the pivot point would be offset from the clamping regions by $760 \mu\text{m}$, and offset from the probe tip contact points by 1.2 mm . Given this geometry and the contact angle of 30° , a overtravel of approximately $14 \mu\text{m}$ would be required before the probe chip contacts the upper half of the block, which is close to what has been observed in the hinged force-

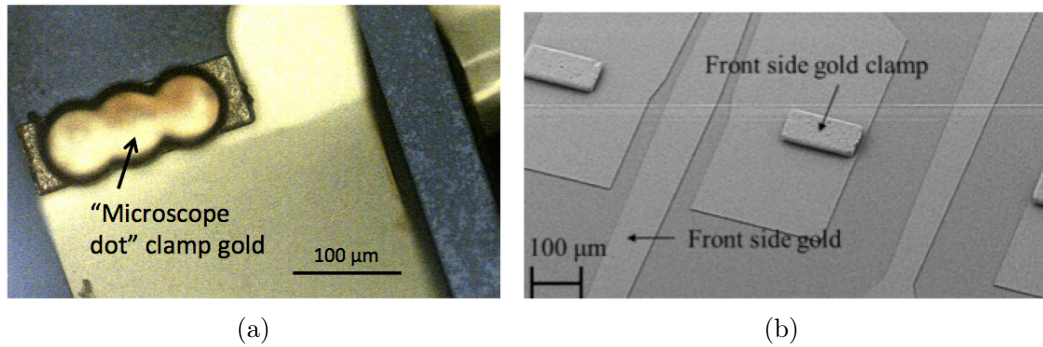


Figure 2.2: Clamp gold structures. (a): Micrograph of manually-added clamp gold through “microscope dot” photolithographic exposure. (b): SEM image integrated clamp gold structures during probe chip fabrication (SEM image courtesy of Naser Alijabbari).

displacement curves.

To test this hypothesis, a method to eliminate the gaps in the milled probe housing was required. It is not possible to mechanically hold or force the gap shut, as it is located at the thin, tip edge of the block. Therefore, attempts were made to add material to the clamping regions to fill the gap. Small amounts of superglue were applied to the clamping regions, but it is difficult to apply a controlled amount in a uniform fashion. As a result, the probe chip is displaced from the clamping regions on closure of the housing. It was acknowledged that use of an epoxy would be ideal in the sense that it would only fill the required space and would not disturb alignment of the probe chip. This method was not pursued further, however, as it would be permanent and negate the ability to replace the probe tip.

A more controllable method was needed, which was addressed by additional gold plating in the clamping regions of the probe chips. This process was implemented through a “microscope dot” exposure method by Zhang [22] on completed probe chips. In this method, small cylinders of gold are plated onto existing probe chips by patterning photoresist through exposure with a focused spot of light from a

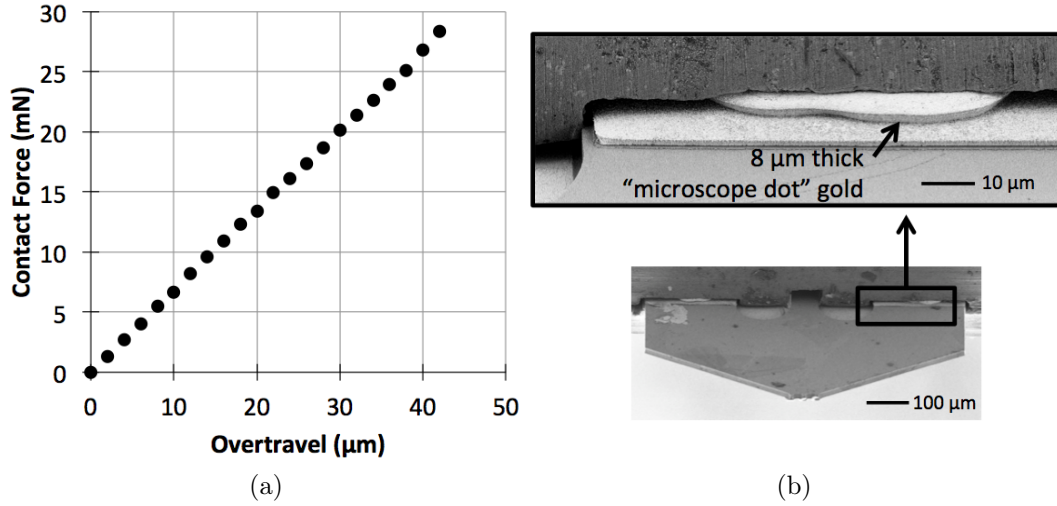


Figure 2.3: (a): Linear force-displacement curve characteristic of well-clamped probe chips. (b): SEM image of assembled probe chip showing the 8 μm clamp gold structure in direct contact with the clamp region of the probe block housing.

high-magnification microscope. This opens a region of approximately $2 \times 10^3 \mu\text{m}^2$ that can be electroplated to add additional gold for clamping. The finished result is shown in Fig. 2.2a, where three cylinders of 15 μm thick gold have been electroplated onto one of the clamping regions.

After this modification, the force-displacement test was repeated, and the result is shown in Fig. 2.3a. The modified probe chip exhibits the expected linear force-displacement relation, confirming the gap as the cause. To allow the possibility of gaps between the halves of the probe block housing, the probe chip fabrication process was modified to integrate a thick layer of “clamp gold”, shown in Fig. 2.2b. The drawback to the approach is that if the gap is small, the clamp gold may “wedge” the block open, raising concerns over the potential for RF performance degradation. To investigate this effect, a 20 μm gap is added to the simulation model of the WR-1.0 coaxial to CPW transition, as shown in Fig. 2.4a. The simulation results, shown in Fig. 2.4b, illustrate that the gap has little effect on RF performance, and the

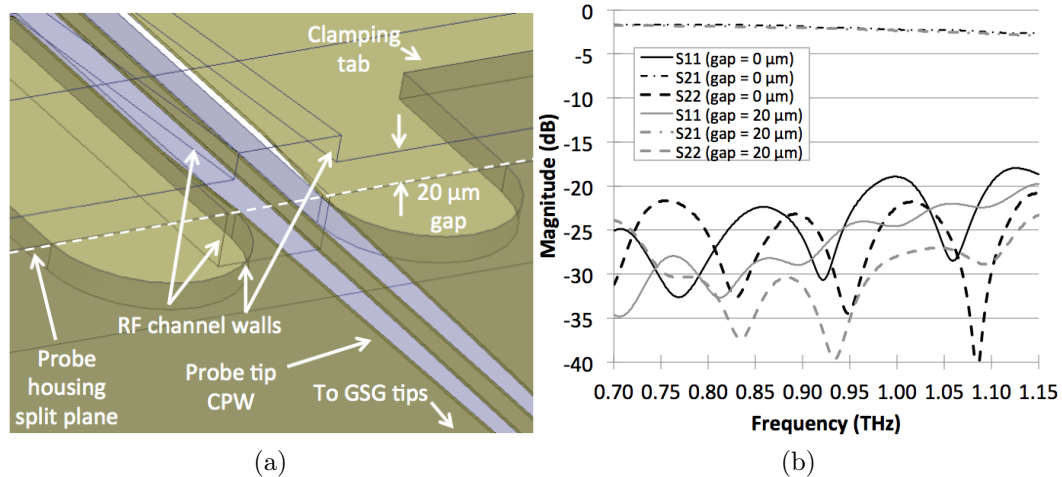


Figure 2.4: (a): HFSS simulation model of WR-1.0 coaxial CPW transition including 20 μm gap (b): Simulated S-parameters illustrating small effect of gap.

WR-1.0 probes, described in Chapter 4, which implement these thick clamp gold features in the presence of a relatively small gap, show outstanding performance. These measurements show that, given the issues created by poor clamping, and the fact that a gap resulting from excess clamp gold has minor electrical impact, thick clamp gold should be a standard feature on micromachined probes.

2.2 Oxidation of Probe Housing

Wafer probes are used for the development and characterization of planar devices, where characterization of the device’s response under different bias conditions is often necessary for building measurement-based models of the device. To accommodate characterization of devices under different DC bias conditions, wafer probes typically include a bias circuit, or “bias tee,” which is a structure designed to provide a DC connection to the probe tips without interfering with the RF performance of the probe.

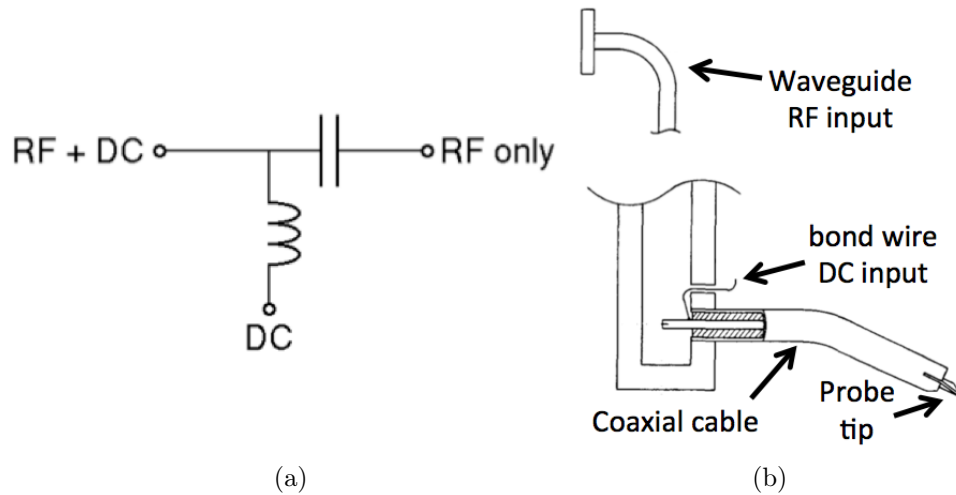


Figure 2.5: (a): Lumped element circuit diagram of low-frequency bias tee (b): Illustration of conventional probe bias circuit [12].

At low frequencies, a bias tee can be implemented using lumped components such as inductors and capacitors, as shown in Fig. 2.5a. This circuit combines the RF and DC signals, while isolating each at the source node. In conventional waveguide-based probes, the RF source is inherently DC isolated by the waveguide. To isolate the DC source, a thin bond wire is connected to the coaxial center conductor of the waveguide transition, as shown in Fig. 2.5b. This wire provides inductance to block the RF signal and is connected to a convenient low-frequency coaxial output on the probe body. The micromachined probe isolates the DC connection through the use of a low-pass filter that provides isolation over the operating band of the waveguide (the design and performance of this filter is described in Chapter 4).

Regardless of the implementation method, the bias at the DC input and the RF signal from the waveguide are combined through the probe's bias circuit and presented to the DUT at the probe tips. By providing DC bias directly at the device, on-wafer probes eliminate the need to make separate DC connections through wire bonds or DC probes, greatly reducing the time and cost to characterize new devices

and freeing up wafer real estate which would otherwise be required for DC pads.

Clearly, to be useful in this sense, it is critical that the probe be able to supply DC bias in a stable, reliable fashion. That is, repeated contacts to a device should result in the same bias conditions, and once a bias level is established, it should not fluctuate. For devices that draw current, fluctuations in the series resistance of the bias circuit, either between subsequent contacts or during a single contact, will cause variations in the bias point of the device, and as a result, introduce errors in modeling of the device. While attempting to characterize submillimeter-wave devices being developed at the University of Virginia, it was discovered that the original micromachined probe design did not provide DC contact in the stable, reliable fashion described above. To more closely examine the performance of the probe bias circuit, an experiment was setup to monitor the resistance and contact force as the probe makes contact.

The experimental setup to monitor the bias circuit during a contact cycle is shown in Fig. 2.6a. A load cell with digital readout (Futek model FSH0234) is mounted to a precision motor stage (Newport model MFA-CC), which provides electronically controlled movement in the vertical direction. A sample with a uniform film of electroplated gold $1.5 \mu\text{m}$ thick is mounted to the load cell, and the probe tip is positioned over the sample. The stage is raised in $2 \mu\text{m}$ increments toward the probe tips. After each stage step, the contact force is recorded from the load cell and the bias tee resistance is recorded from a digital multimeter. This step is repeated until the contact force reaches 20 mN, at which point the motor stage is lowered to its starting position, completing a contact cycle.

The contact cycle was repeated ten times, and the measurement result is shown in Fig. 2.6b. It is important to first note that the DC isolation between the G-S-G tips is non-zero due to the resistivity of the silicon substrate ($> 10 \text{ k}\Omega \cdot \text{cm}$), resulting

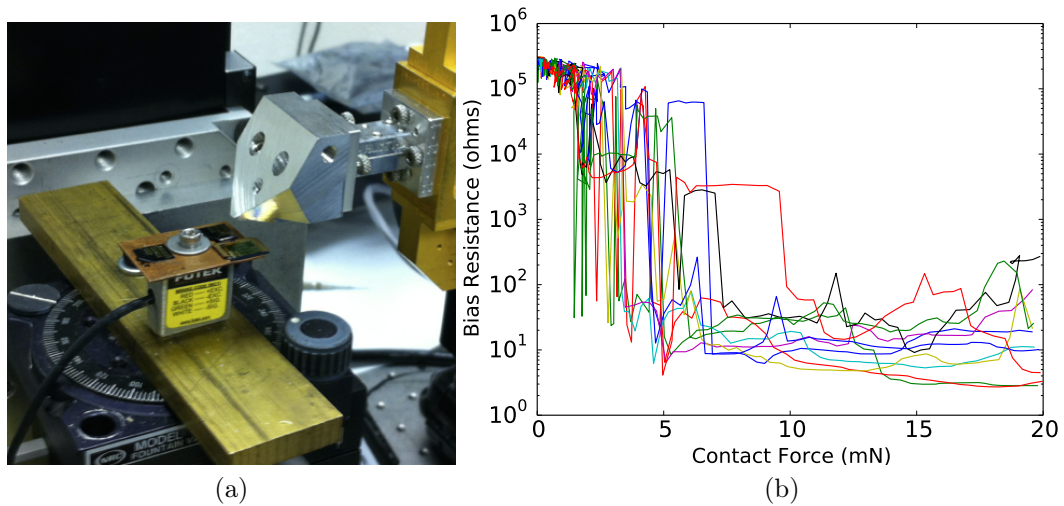


Figure 2.6: (a): Experimental setup for measurement of bias circuit resistance during contact cycles (b): Resistance measured at the bias circuit input during 10 contact cycles.

in a bias resistance on the order of $100\text{ k}\Omega$ when the probe tips are open-circuited (zero contact force). When the probe tips are landed on a uniform gold film, the G-S-G the tips are short-circuited. It is anticipated that this would present a low resistance at the DC bias input. However, as seen in Fig. 2.6b, shorting the tips in this fashion yields variable results: 1) the required force to achieve a relatively low resistance at the bias tee input varies significantly on each contact cycle, 2) at a given contact force, variation in the bias circuit resistance is typically not less than an order of magnitude, and 3) once a relatively low resistance contact is established, a small increase in contact force could change the bias tee resistance by as much as three orders of magnitude.

To measure a short at the bias circuit input, current must flow through one or both ground-signal pairs of the G-S-G tips. Therefore, to determine if the irregular resistance measurements were due to one or more particular tips, the experiment was repeated using a sample with patterned areas of gold shown in Fig. 2.7a. A

wire is connected to each of the three individual gold traces, allowing the resistance between the gold and each of the three tips to be monitored independently. In this experiment, the resistance between the gold film and each of the ground tips showed the same behavior illustrated in Fig. 2.6b, while the signal tip consistently produced a resistance of several ohms that remained steady as the contact force increased. This experiment showed that the DC ground paths are responsible for the observed irregular contact resistance. Referring to Fig. 2.7b, we see that the DC ground path relies on connection of the probe chip beamleads to the probe block housing. At this point, it was surmised that the native aluminum oxide on the surface of the probe block may be preventing a low-resistance connection to the ground beamleads to the probe housing.

To test this hypothesis, several experiments were conducted to evaluate methods for improving the conductivity between the ground beamleads and the probe housing. These approaches included adding a conductive “shim” of material, (i.e. a manually folded gold beamlead, or indium solder ball, shown in Fig. 2.8a) between the probe housing and the probe chip ground beamlead. Other methods, such as

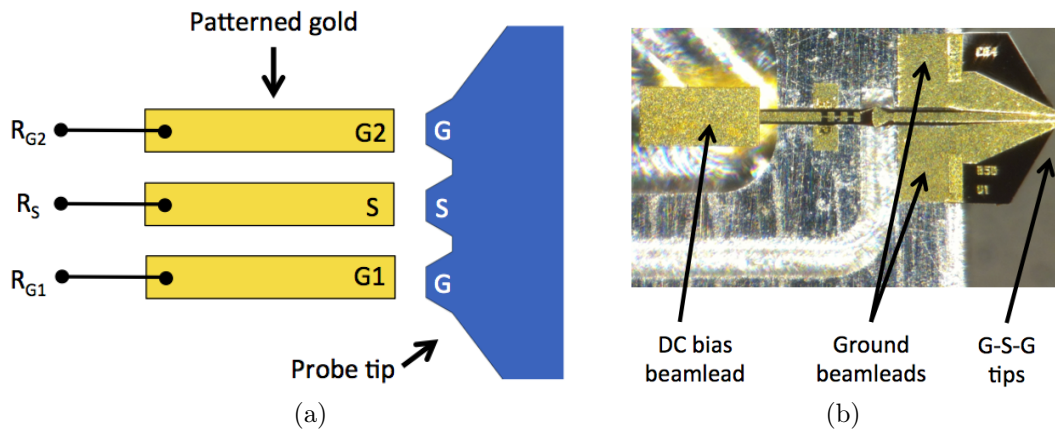


Figure 2.7: (a): Isolated on-wafer traces for independent tip resistance measurement. (b): Mounted probe chip illustrating the ground beamlead reliance on the probe housing surface for ground.

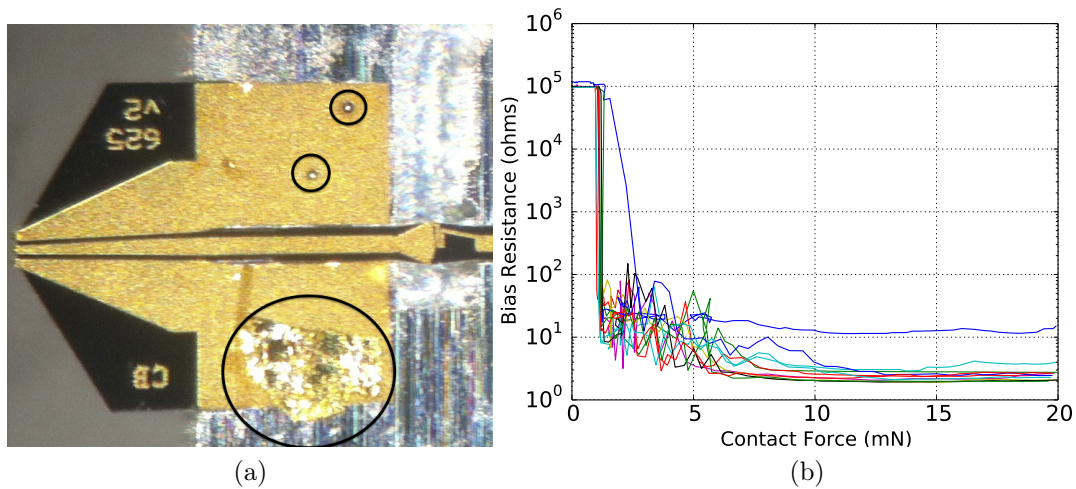


Figure 2.8: (a): Illustration of attempted grounding fixes: two indium solder balls (above), folded gold beamlead (below). (b): Improved bias resistance measurement results.

using a conductive epoxy are possible. However, concern over permanent damage to the probe housing and the ability to replace probe chips eliminated this approach from consideration. Repeating the DC contact experiments with the gold or indium shims in place showed some improvement, as shown in Fig. 2.8b. However, the assembly process was problematic, as it was difficult to place the solder ball or beamleads precisely without causing misalignment of the probe chip. Given that such methods were unreliable and ineffective, a more robust solution was sought.

To provide a conductive, non-oxidizing surface for the DC ground path, fixtures were designed and machined to hold the probe block halves for sputter deposition of a thin layer of gold (approximately $1 \text{ k}\text{\AA}$) to be deposited on the internal surfaces of the probe housing, as shown in Fig. 2.9a. After sputter deposition of gold on the block halves, the DC test was repeated and the results, shown in Fig. 2.9b, exhibit stable and repeatable DC contact resistance. On each contact cycle, the bias resistance is below 3.1Ω at 1.5 mN contact force, where it remains throughout the

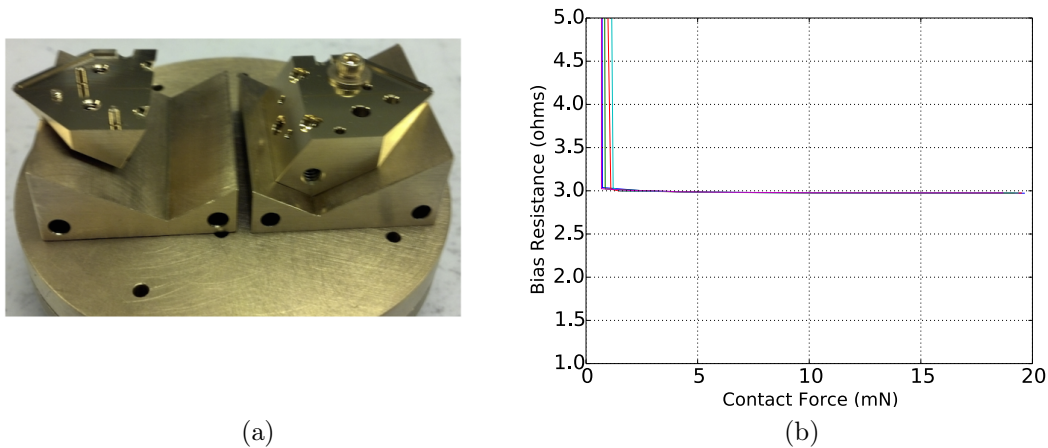


Figure 2.9: (a): Probe housings mounted to the sputtering fixture after deposition of gold. (b): Measurement results of bias resistance test using gold sputtered probe blocks.

contact cycle. These experiments show that the aluminum surface of the waveguide housing does not provide a sufficiently reliable electrical for the micromachined probe chips and as a result, a non-oxidizing, low resistivity material such as gold should be used to coat the inner surface of the probe block housings.

2.3 Fracturing of the Silicon Substrate

An additional behavior observed during use of the probe was fracturing of the silicon near the “neck” where the probe emerges from the housing, as shown in Fig. 2.10a. It was discovered that this fracturing always occurred on the initial contact cycle of a newly assembled probe and it occurred consistently in the same location. The force displacement curve shown in Fig. 2.10b shows such a contact cycle where the point of fracture occurs at approximately 4 mN contact force. An image of a probe chip after fracture is shown in Fig. 2.11a. Fracture at this location seemed unusual, as the simulated stress profile of the probe chip when subjected to a 4 mN load at

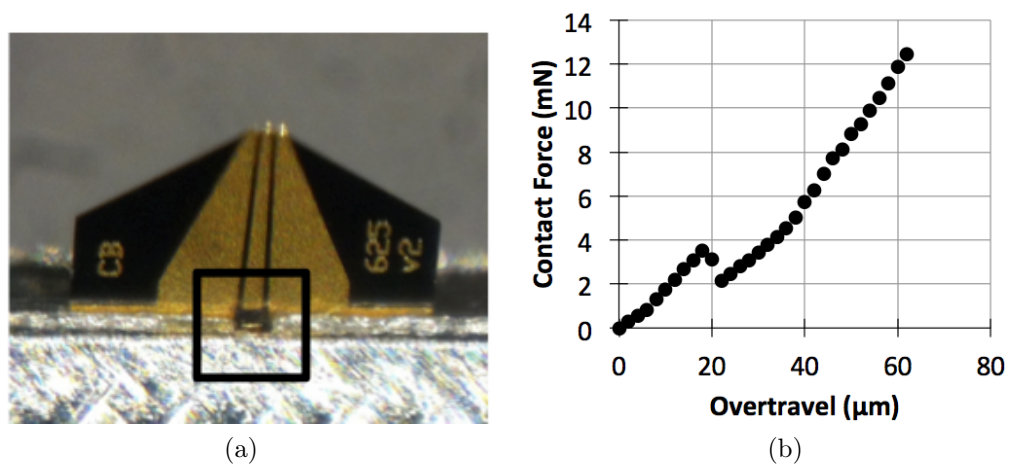


Figure 2.10: (a): Mounted of probe chip after single contact cycle illustrating cracked “neck.” (b): Force-displacement curve of a single, first contact.

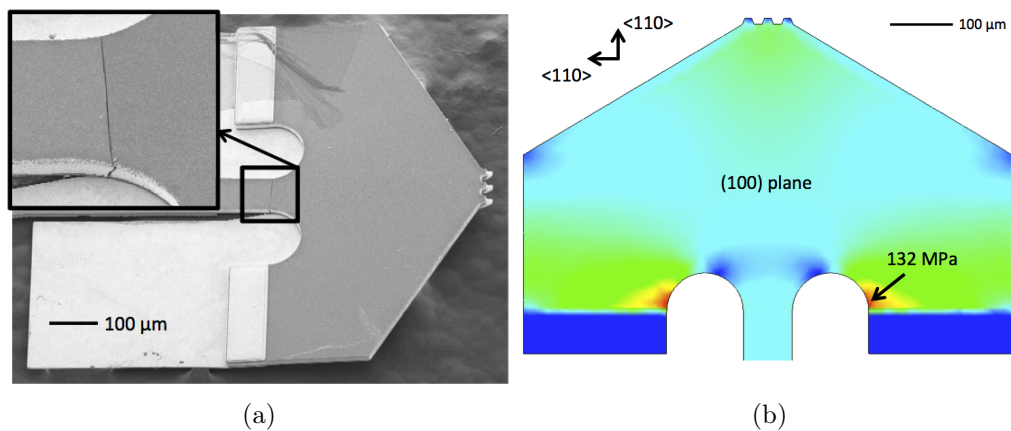


Figure 2.11: (a): SEM of probe tip after fracture (b): Simulated stress profile of micromachined probe tip under 4 mN load. The maximum is indicated by the marker.

the tip, shown in Fig. 2.11b, shows the maximum stress to be near the fillets where the probe is clamped to the housing.

In [17], Li et al. measure the fracture stress of thin silicon films micromachined on the (100) wafer plane. As shown in Fig. 2.12a, a load lever applies a tensile stress in the $\langle 110 \rangle$ direction, resembling the loading configuration of the micromachined probe (noted in Fig. 2.11b). The measurement results of their experiment, shown

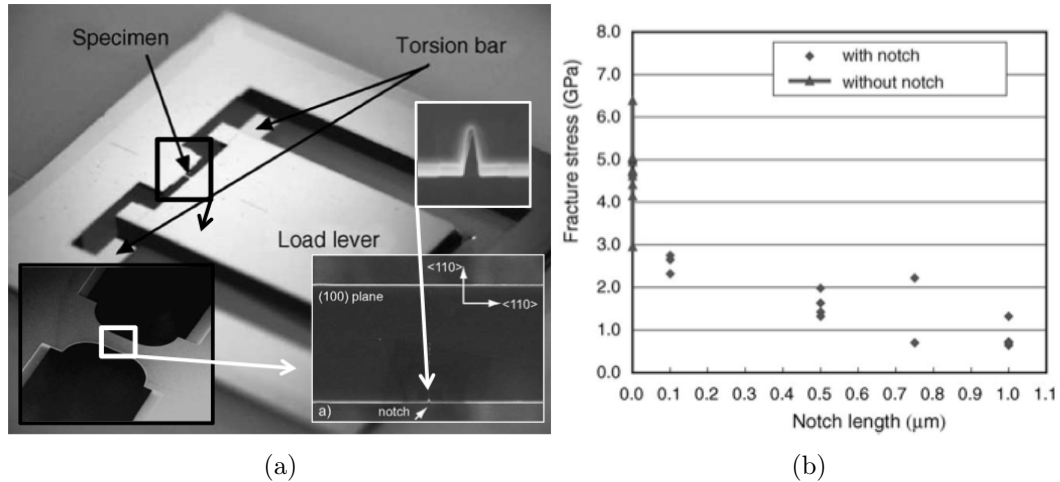


Figure 2.12: Micromachined thin silicon fracture experiment by Li et al. [17]. (a): SEM images illustrating $1.0 \mu\text{m}$ notch in thin silicon beam sidewall. (b): Decreased fracture stress associated with notch length. Figures from [17].

in Fig. 2.12b, indicate a dramatic reduction in fracture stress to an average of 850 MPa for a $1.0 \mu\text{m}$ notch length. While the geometry of the probe chip at the point of fracture is different ($75 \mu\text{m}$ wide \times $15 \mu\text{m}$ thick), this study illustrates the mechanical sensitivity of micromachined silicon structures to defects. It was suspected that perhaps there were irregularities in the silicon sidewalls of the probe chip that could be causing this failure.

To investigate this hypothesis, probe chips were examined using SEM prior to the use for probing. While no irregularities were observed in the silicon sidewalls, an unusual feature was observed in the vicinity of the failure point. Shown in Fig. 2.13, a small “rim” of silicon remains along the base edge of the main silicon body. It was suspected that this rim was the root cause of the failure. The gold beamlead is not fixed at the point where it intersects the rim (the probe neck and failure point). Because the silicon rim is thin, it can easily crack due to movement of the beamleads during the fabrication release process and/or during the probe assembly process. Under load, the crack in this thin silicon rim can then propagate into the

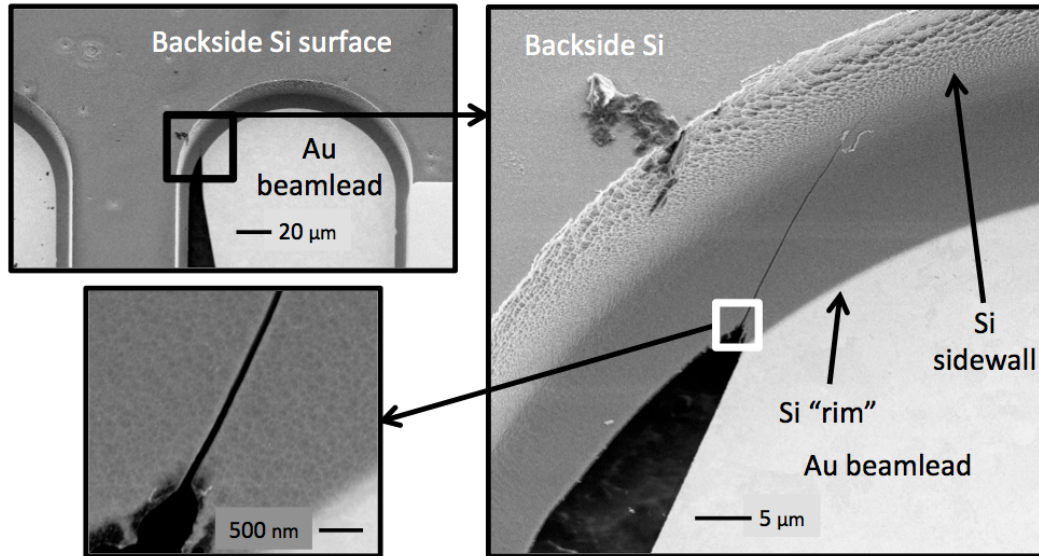


Figure 2.13: SEM image illustrating fracture mechanism. The gold beamlead is not rigidly fixed and small movement creates a “seed” crack in the silicon “rim” where they intersect. In the case of this chip, the fracture has already propagated slightly into the sidewall of the main silicon body.

silicon substrate, causing fracture at the probe neck.

To further investigate this hypothesis, a probe was assembled and was subjected to a single contact cycle. Measurement of force-displacement indicated a typical fracture characteristic as observed in previous measurements. The probe was then carefully disassembled, with the goal of removing the probe chip intact. This probe chip was examined under SEM, and the images are shown in Fig. 2.14. The observed continuity of the fracture line between the rim and the probe neck strongly suggests that a small seed crack in the silicon rim will propagate and cause the fracture. This experiment initiated fabrication of a new set of probe chips utilizing an extended silicon etch process to ensure removal of any residual silicon rim [22]. Under SEM inspection, the new set of chips showed no visual evidence of a silicon rim. During testing, these chips did not show the characteristic fracture point in the force-displacement curve and were not observed to have fractured at the neck after

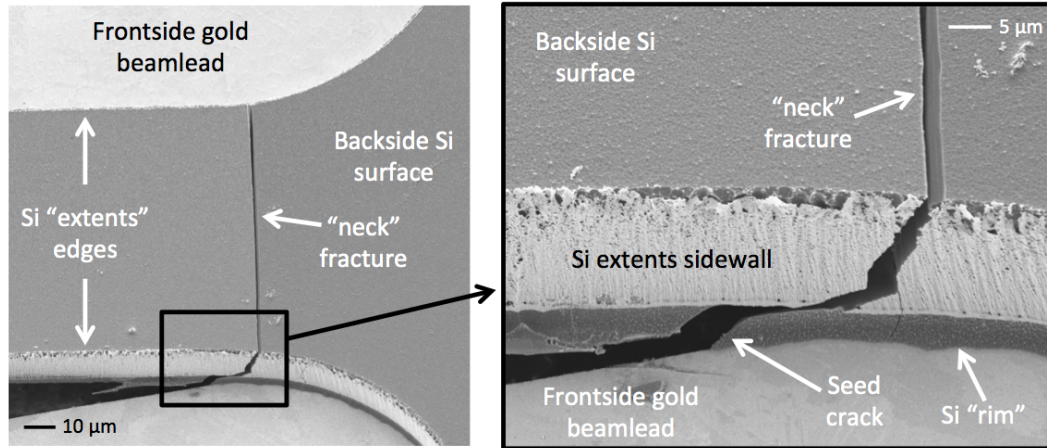


Figure 2.14: SEM image of intact probe chip after silicon fracture

use. These experiments and measurements demonstrate the importance of close inspection and verification of edges during fabrication of silicon micromechanical components.

2.4 Tip Metallization and Probe Contact Resistance

The soft gold-plated probe tip contacts implemented in the original prototype micromachined probes were not robust and did not exhibit long lifetime, as the gold proved to be completely worn off after 10,000 contacts [14]. To improve the lifetime of the probe tips, the soft-gold metallization was replaced with a hard gold formulation through the use of Technic Orosene 990HS gold plating solution, which includes a cobalt hardening additive. This change significantly improved the lifetime of the probe tips, which showed no measurable degradation in performance after 20,000 contacts, and only moderate wear [20, 21]. While this was a marked improvement in potential lifetime, a different critical failure mechanism related to the tip metallization was subsequently discovered.

As the micromachined probes saw greater use in on-wafer characterization of

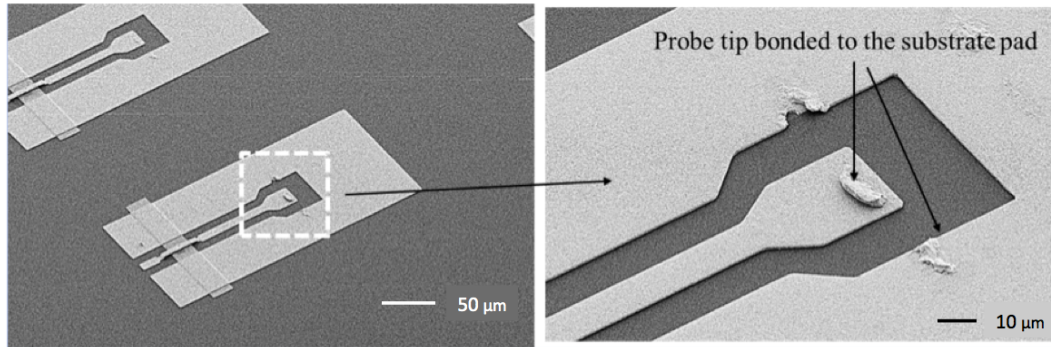


Figure 2.15: SEM image of on-wafer probe pads showing fragments of the gold probe tip stuck to the pads (image courtesy of N. Alijabbari).

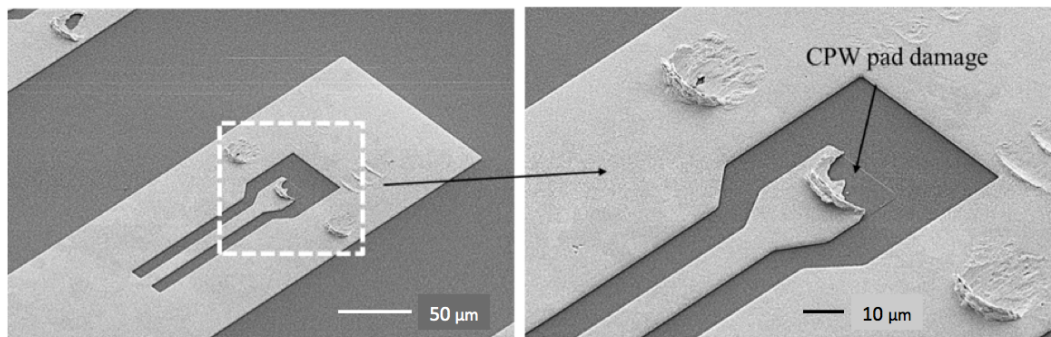


Figure 2.16: SEM image of on-wafer probe pads showing removal of part of the pads (image courtesy of N. Alijabbari).

various submillimeter-wave circuits and devices, a new issue became apparent. As shown in Figs. 2.15 and 2.16, it was observed that the probes would frequently deposit or remove material from the device-under-test (DUT) contact pads. In cases where the DUT circuitry is formed on a dielectric polymer, the dielectric material itself was often removed as well, as shown in Fig. 2.17. Moreover, Fig. 2.17 illustrates that the on-wafer pad is not simply displaced by the probe tip, but is attached to it. Because the three probe tips are not independently compliant, the probe tips and contact pads must each be coplanar for the probe to make contact. As a result, in these cases, bonding of the DUT pad metal to the probe represented failure. This proved to be a significant problem, as it not only permanently damaged

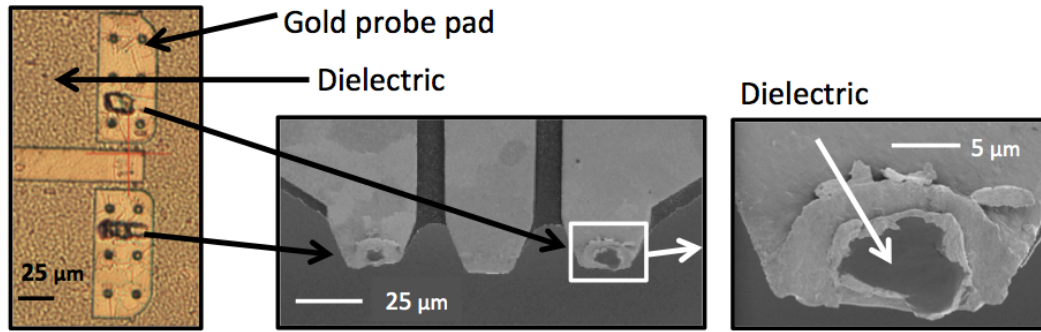


Figure 2.17: Micrograph showing delamination of probe pad and underlying dielectric polymer.

the probe tip, but it also was destructive to the DUT.

Referring to the lightly used probe tip shown in Fig. 2.18, if we take the deformed area of the tips to correspond to the approximate contact area, we estimate the effective contact area of the three tips to be on the order of $360 \mu\text{m}^2$. At a typical measurement contact force of 10 mN, this results in an average contact pressure of 28 MPa. In [24], Whitesides et al. report on cold welding of gold films under ambient laboratory conditions with small loads ($< 10\text{-}20 \text{ Pa}$). Because it is not possible to mechanically remove the gold material from the probe tip or the DUT, it is believed that this bond is effectively a cold weld between the gold tips and the DUT gold pad. While this problem was initially believed to simply be a matter of poor adhesion between the substrate and contact pad metallization that could be resolved through fabrication improvements, after observing the problem on a variety of samples, it became clear that it would be more reliably addressed through a change in the probe tip metallization.

Table 2.1 lists several potential probe tip metals. Nickel and rhodium are both used commercially for probe tip contacts and based on its increased hardness and conductivity over nickel, rhodium would be preferred. However, it is difficult to electroplate crack-free rhodium films, and as a result, nickel, which is readily integrated

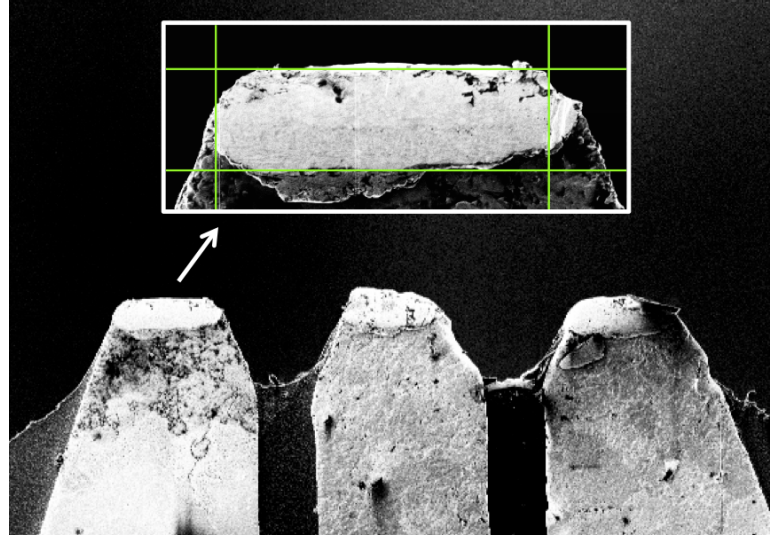


Figure 2.18: SEM image of a probe tip after several hundred contacts. Shown in the inset, the deformed area indicated by the markers is approximately $20\ \mu\text{m} \times 6\ \mu\text{m}$.

Table 2.1: Conductivity and hardness comparison of potential probe tip metals [23]

Material	Conductivity (S/m)	Hardness (Mohs Scale)
Gold	4.4×10^7	2.5
Nickel	1.3×10^7	4.0
Rhodium	2.3×10^7	6.0

into the probe fabrication process, was adopted for probe tip metallization. Due to its relatively low conductivity, however, the $1.0\ \mu\text{m}$ thick nickel layer is deposited only over a small area near contact points, as illustrated in Fig. 2.19a [25].

To evaluate the contact repeatability of the nickel tips on gold pads, the nickel-tipped probes were repeatedly contacted to a gold film using $10\ \mu\text{m}$ of fixed over-travel (approximately $7\ \text{mN}$ contact force) and the resistance at the probe bias port input was recorded. The results of these measurements are shown in Fig. 2.19b, indicating excellent repeatability, with a standard deviation of less than $1\ \text{m}\Omega$ over 50 contact cycles. Additionally, as intended, delamination of the probe tips or gold DUT contact pads has not been observed, with typical marks shown in Fig. 2.20.

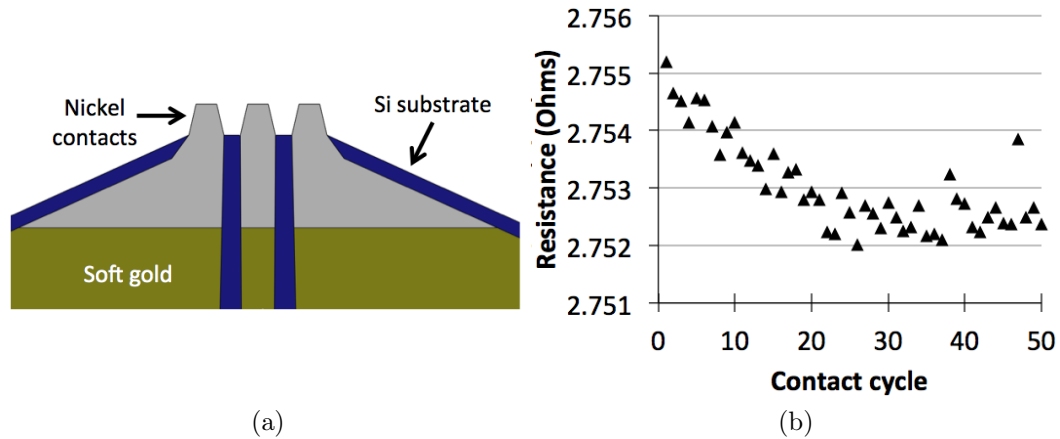


Figure 2.19: Nickel probe tips. (a): graphic illustrating localized application of nickel over the contact area. (b): DC contact repeatability of nickel tips on gold using fixed 10 μm overtravel, as measured as the bias tee input.

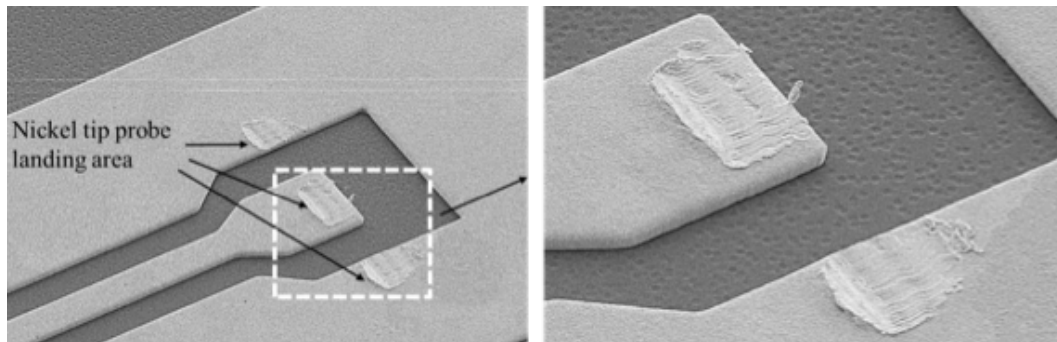


Figure 2.20: Nickel probe tip marks on gold pads (image courtesy of N. Alijabbari).

As an additional benefit, use of a harder contact material may enable contact to devices with aluminum probe pads. This is important because millimeter and submillimeter-wave circuits are increasingly implemented in CMOS-based processes where aluminum pads are often used. Because aluminum forms a hard, electrically insulating oxide at room temperature, gold-tipped probes are not able to penetrate the surface and produce a low-resistance contact to the underlying aluminum. To evaluate the suitability of nickel contacts for aluminum pads, the contact repeatability experiment was repeated, contacting an aluminum sample instead of gold. As expected, it was found that greater force was required to make a low-resistance

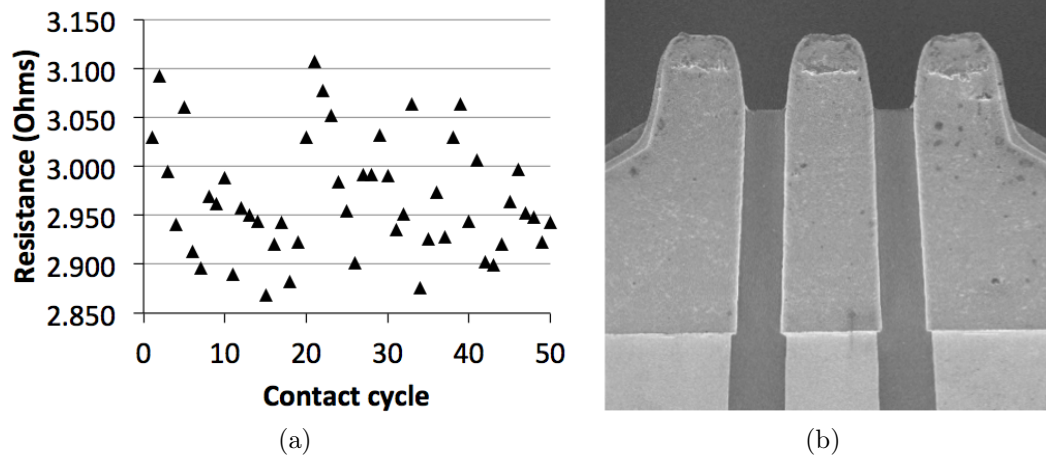


Figure 2.21: Nickel probe tip contact on aluminum. (a): DC contact repeatability of nickel tips on aluminum using fixed $35\ \mu\text{m}$ overtravel. (b): SEM image of probe tips after approximately 200 contacts cycles.

contact to the aluminum film and the experiment was conducted using $35\ \mu\text{m}$ of fixed overtravel (approximately 25 mN contact force). The results are shown in Fig. 2.21a and illustrate reduced repeatability compared to gold. The standard deviation over 50 cycles is $59\ \text{m}\Omega$, while the mean resistance is $215\ \text{m}\Omega$ higher than on gold. As wear of the nickel tips due to this relatively high contact force is a concern, an additional 150 contacts were made and the tips were inspected in SEM. Shown in Fig. 2.21b the SEM images illustrates that, despite use of a much higher force of approximately 25 mN, after 200 contacts, wear of the nickel tips is not yet evident, in contrast with the cobalt-hardened gold tips shown in Fig. 2.18.

The previously described resistance measurements include the series resistance of the bias circuit itself. To isolate the resistance between the on-wafer metal and the probe tip, a probe chip for four-point measurement, shown in Fig. 2.22, is used to repeat to contact resistance tests. The single probe tip has two on-chip electrical connections: one is used to flow current through the tip onto the wafer, the other is used to sense to voltage at the probe tip. Two needle probes are placed

on-wafer to sink the current and sense the voltage on-wafer near the probe tip. This measurement of the voltage drop across the probe tip allows in-situ isolation of the contact resistance. The result of the measurements on both gold and aluminum are shown in Fig. 2.23. The mean four-point contact resistance on gold is $36 \text{ m}\Omega$ and on aluminum is $214 \text{ m}\Omega$, while the standard deviation for each is $3 \text{ m}\Omega$ and $61 \text{ m}\Omega$, respectively.

While more repeatable contact on aluminum is desired, the implementation of nickel contacts was nonetheless an important improvement, achieving the desired goal of preventing damaging delamination of the probe tips and DUT contact pads. In addition, initial data suggest that the increased hardness of the nickel may offer increased lifetime over the hard gold tips.

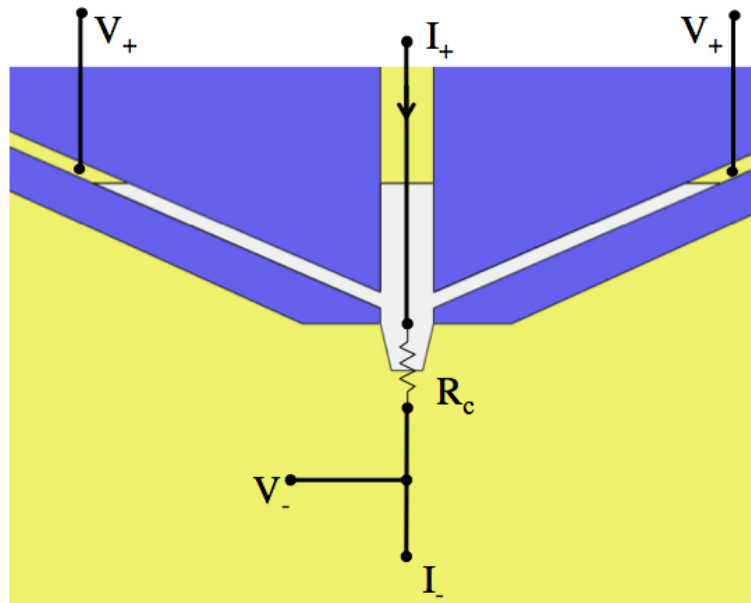


Figure 2.22: Four point contact resistance measurement configuration.

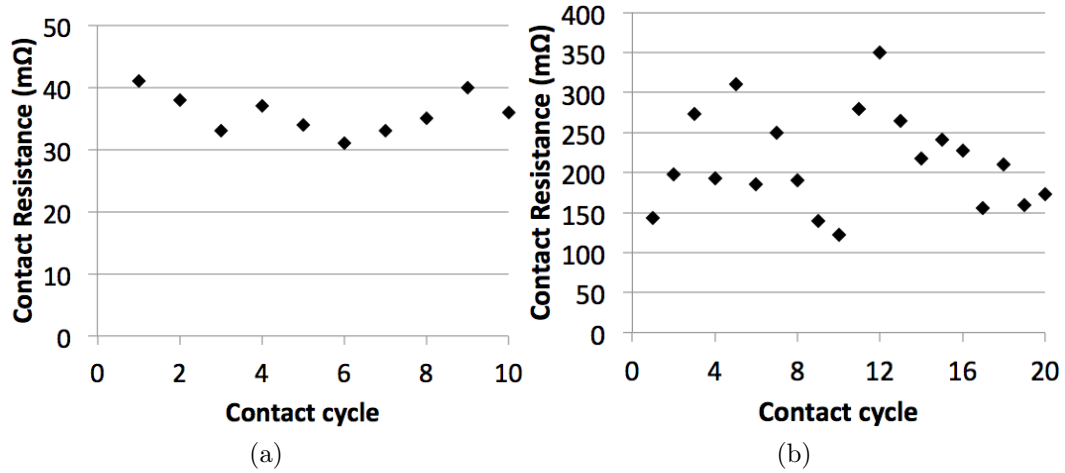


Figure 2.23: Four point contact resistance measurements of nickel tip to (a): gold, and (b): aluminum.

2.5 Improved Probe Housing Architecture

While the original micromachined probe housing functions as intended, the layout of the housing results in several of disadvantages. In the original architecture, the probe tip angle must equal the split angle of the waveguide housing, and as a result, a compromise must be made between electrical and mechanical performance, the details of which have been analyzed in previous work [14, 15]. The implications of this compromise are that the waveguide angle is fixed, a waveguide twist is required, and discontinuity exists at the probe waveguide input.

At submillimeter-wave frequencies, waveguide loss is substantial. For example, in WR-1.0 waveguide (750 GHz - 1.1 THz), the attenuation is approximately 1.6 dB/cm at the center frequency of 925 GHz. Therefore to minimize loss in the measurement setup, the length of waveguide between the probe tip and signal sources and receivers should be minimized. However, due to the orientation of the original micromachined probe waveguide channel, the minimum required length is significant. As shown in Fig. 2.24, a waveguide “S-bend” (3.6 cm path length) is required

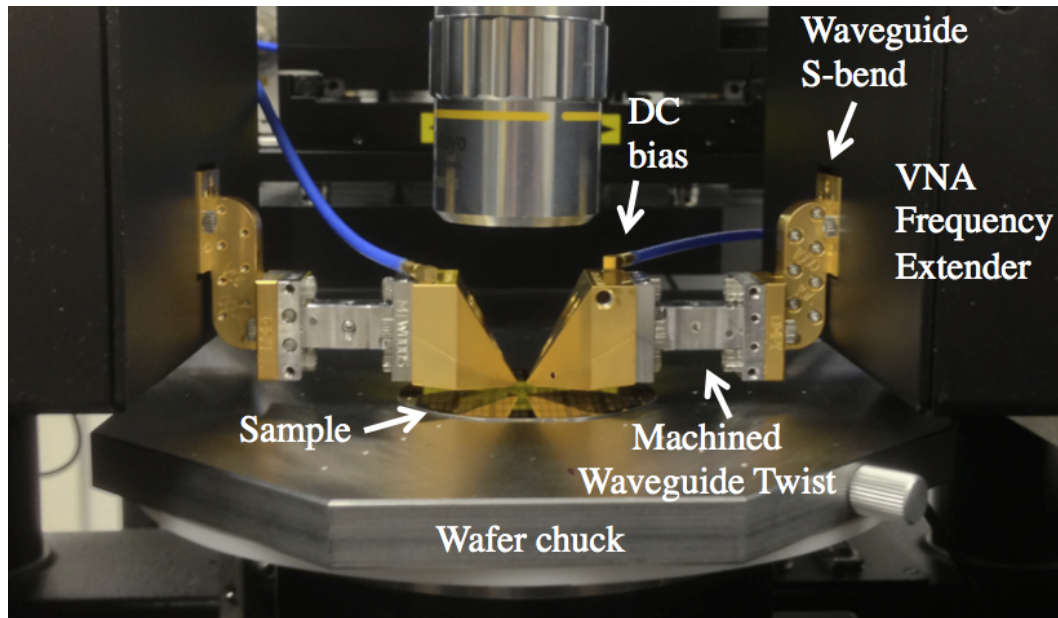


Figure 2.24: Micromachined probe station measurement setup.

to lower the probe tip below the bottom of the frequency extender to enable contact with the sample. A 2.5 cm long waveguide twist is used to connect the probe to the S-bend. Finally, a 2.0 cm section of waveguide carries the signal from the probe waveguide input to the tip of the housing at a 30° angle. Thus, to implement a WR-1.0 measurement setup in the configuration shown in Fig. 2.24, the 8.1 cm waveguide path length between the frequency extender output and probe tip waveguide transition contributes approximately 13 dB of loss at 925 GHz.

The 2.0 cm length of the probe waveguide channel is already at the minimum required to enable connection to the waveguide interface. To ensure a smoothly rotating waveguide channel necessary for high return loss, the twist is machined over a 2.5 cm length. Finally, the minimum S-bend length is set by the distance between the waveguide output of the frequency extender and the bottom of the frequency extender enclosure. Therefore, the overall waveguide length of the original micromachined probe configuration shown in Fig. 2.24 cannot be significantly reduced.

To allow reduction in the overall length, a new probe housing should implement two properties: (1) the new housing must not require the use of a waveguide twist, and (2) the design should not require a fixed waveguide angle.

It is important to acknowledge that the micromachined waveguide twist shim [26] is an alternative option to the machined twist at submillimeter-wave frequencies. It is compact (380 μm length for WR-1.5), and achieves excellent peak performance (e.g. < 0.4 dB insertion loss and > 25 dB return loss at 625 GHz). However, the design is relatively sensitive to misalignment associated with the waveguide interface, which typically results in reduced performance near the waveguide frequency band edges. The machined twist is therefore preferred, in general, for its broadband performance.

A new probe housing is developed that meets the above requirements. A comparison of simulation models for the original and improved design is shown in Fig. 2.25, which best illustrates the electromagnetic change. The waveguide channel of the original housing is rotated upwards by 90° about the axis of the RF channel, which eliminates the need for the waveguide twist. The backshort is split from the main waveguide channel, such that the probe chip can be clamped in place. Finally, in this configuration, note that it is possible to change the angle of the waveguide using E-plane bends, which provides potential for path length minimization and also permits elimination of the waveguide discontinuity that occurs at the waveguide interface of the original probe housing.

A proof-of-concept is implemented in the WR-5 waveguide band (140 - 220 GHz), and a model of the improved housing is shown in Fig. 2.26. It must be noted that the disadvantage of this approach is increased machining complexity: the improved probe housing consists of three separate pieces instead of two. The waveguide channel is E-plane split in two mirror-symmetric sections (upper right

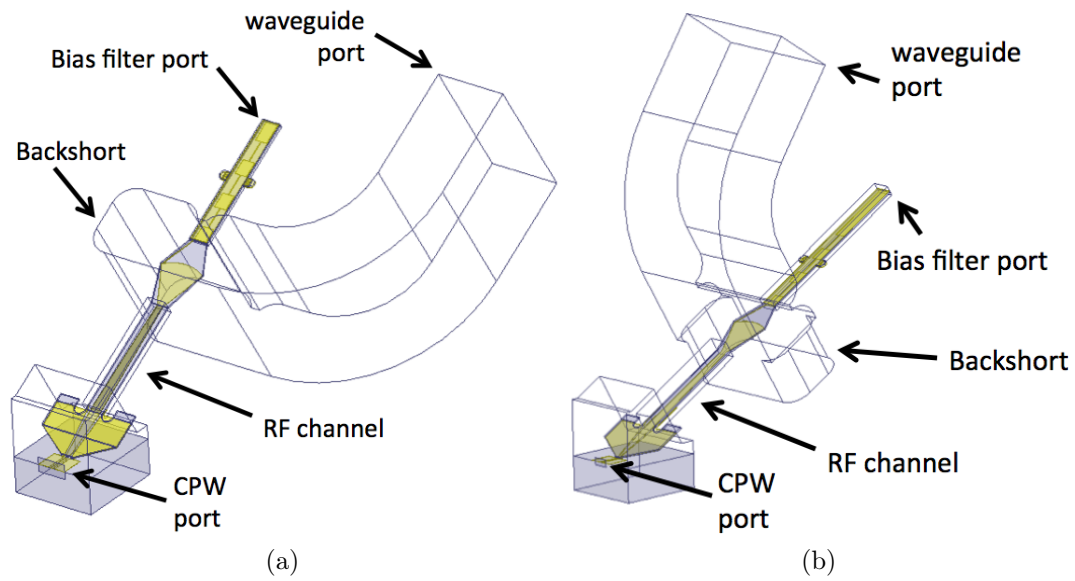


Figure 2.25: Simulation model comparison of micromachined probe housing architectures. (a) Original micromachined probe configuration. (b): Improved micromachined probe configuration.

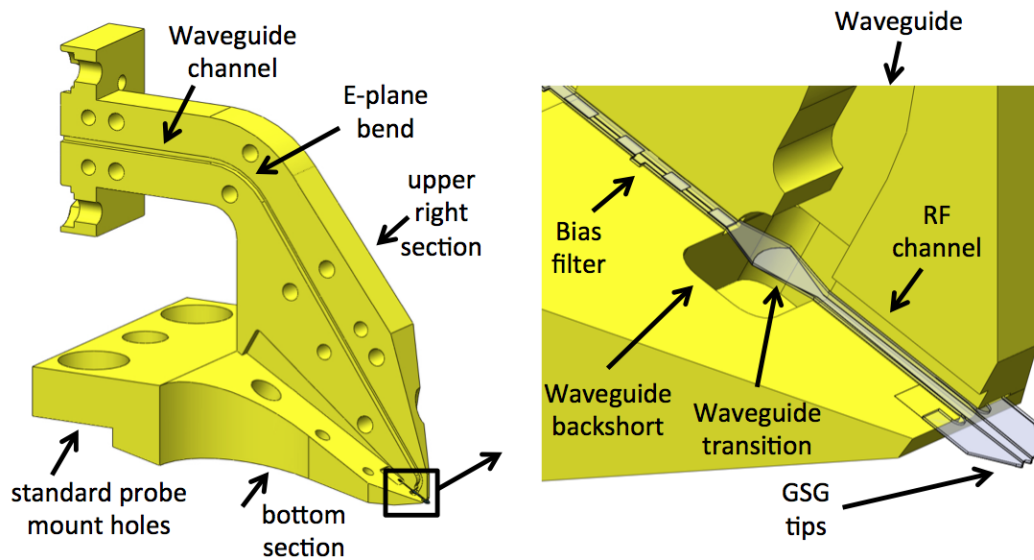


Figure 2.26: 3D model layout of improved probe housing. The upper left section is mirror-symmetric to the upper right and is removed to illustrate the waveguide channel.

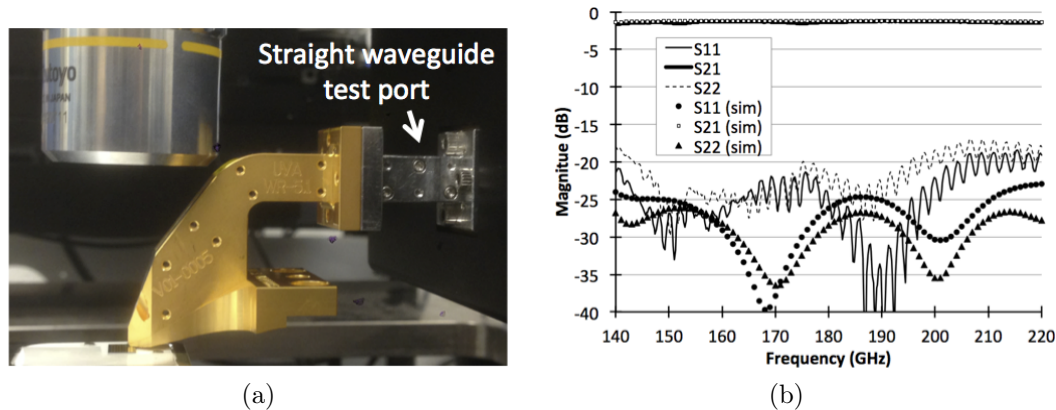


Figure 2.27: Test of improved probe housing proof-of-concept (a) On-wafer test setup. (b): Measured probe S-parameters.

and upper left), while the backshort is formed in the bottom section, which clamps the probe chip in place. The path length between the probe waveguide input and the waveguide transition at the tip is 5.3 cm.

The RF test setup for the improved housing is shown in Fig. 2.27a. It should be noted that for the purposes of determining the probe S-parameters, it is connected to the frequency extender through a section of straight waveguide. However, because the improved housing does not require an S-bend or waveguide twist, it is possible to remove the straight waveguide section and connect the probe directly to the waveguide output of the frequency extender. In this configuration, the overall waveguide length is 5.3 cm, a 35% reduction over the minimum required by the original housing. Additionally, the proof-of-concept includes mounting holes (noted in Fig. 2.26) that are standardized for on-wafer probing at frequencies below 330 GHz. At submillimeter-wave frequencies, this mount could be removed, permitting further reduction of the overall waveguide length. A comparison of the measured and simulated RF performance is shown in Fig. 2.27b. The measured insertion loss is less than 1.7 dB and the measured return loss is greater than 17 dB across the

full band, which agrees well with simulation and illustrates the success of the new housing design.

2.6 Conclusion

The work described in this chapter identified four critical previously unobserved issues related to the robustness and reliability of micromachined probes. First, it was shown that the micromachined probes did not produce a linear force-displacement curve as intended, the cause of which was identified as poor clamping of the chip by the machined housing. Use of an integrated thick “clamp gold” layer, which is readily added to the fabrication process, was shown to eliminate this problem. Based on the results of the WR-1.0 probes described Chapter 4, this structure does not degrade RF performance of probe.

Second, it was shown that the micromachined probes did not provide reliable DC contact to on-wafer samples. The cause of this phenomena was determined to be the native oxide on the surface of the aluminum probe block housing, on which the probe relies for DC grounding. It was shown that deposition of a thin layer of gold onto the aluminum surface prevented this problem.

Third, it was observed that the micromachined probes would frequently fracture on the first contact cycle at low contact force. The fracture occurred consistently in the same location and was shown to be caused by a thin “rim” of silicon remaining along the base of the silicon sidewall after etching. Extending the duration of the silicon etching during fabrication, along with close inspection prior to release, was shown to eliminate this problem.

Fourth, it was shown that use of the probes for repeated measurement of devices was often problematic, as this frequently resulted in removal and accumulation of

material from the DUT pads, rendering the probe and/or DUT destroyed. It was shown that this removal and accumulation was not simply displacement of gold, as it could not be removed through mechanical abrasion afterwards. Considering the contact pressure of approximately 30 MPa, it is thought to be a cold weld between the gold probe tips and DUT pads. To address this problem, the probe tip metallization was augmented with nickel plating, which resulted in repeatable contact on gold pads without any observed delamination issues. Moreover, due to the increased hardness of the nickel tips, it was shown for the first time that micromachined probes could make contact to DUTs with aluminum pads, an increasingly important capability at millimeter and submillimeter-wave frequencies. The contact to aluminum is substantially less repeatable than that on gold, warranting further work on the tip metallization as discussed in Chapter 5.

Finally, a new micromachined probe housing architecture is developed. The improved housing design significantly reduces the minimum required waveguide length between the waveguide output of the frequency extender and the probe waveguide transition and eliminates the H-plane waveguide junction discontinuity at the probe waveguide input.

The issues identified in this chapter are critical aspects related to the reliability and robustness of micromachined probes and their use as the basis for high frequency device characterization. The solutions identified are readily integrated into the fabrication of the probe chips and waveguide housing, and do not degrade performance or increase difficulty of assembly. Identification and solution to these problems is an important engineering contribution that enable use of micromachined probes in characterization of millimeter- and submillimeter-wave circuits.

Chapter 3

Design and Characterization of WR-1.2 Micromachined Probes

Earlier analysis of micromachined probes suggested that the silicon substrate thickness should be reduced to $5\ \mu\text{m}$ or less to avoid substrate mode excitation and enable low-loss operation to 1 THz and beyond [18]. However, thinning the probe tip substrate reduces the force that can be generated at the on-wafer contacts which, at some point, reduces the ability to make a low-resistance contact to an on-wafer device. As a result, there is an inherent tradeoff between the electrical and mechanical performance of the probe with respect to substrate thickness.

This chapter presents the electrical and mechanical design and characterization of a micromachined probe implemented on $5\ \mu\text{m}$ thick silicon to cover the WR-1.2 waveguide band (600 - 900 GHz). This work serves three purposes: 1) to evaluate the feasibility of using thinner silicon substrates for micromachined probes, 2) to investigate the effectiveness of using wider probe chips to mitigate the reduced spring constant resulting from the thinner substrate, and 3) to build on previous micromachined probe work at WR-1.5, expanding on-wafer measurement infrastructure

to enable testing up to 900 GHz for the first time.

3.1 RF Channel Considerations

The RF channel is a trench milled into the waveguide housing, creating a connection between the external probe contacts and the rectangular waveguide. As shown in Fig. 3.1, with the probe chip installed in the housing, a rectangular coaxial transmission line is formed in this channel, which allows the signal to be coupled from the waveguide to the probe tips. The signal conductor is part of the probe chip and is supported by the probe substrate, while the walls of the RF channel serve as the ground shielding. At sufficiently high frequency, this structure can also be viewed as a dielectric-loaded waveguide capable of supporting high-order propagation modes in addition to the quasi-transverse electromagnetic (TEM) coaxial mode. To prevent loss of energy to these modes, the channel should be designed such that the cutoff frequency for the first higher-order mode is above the probe's operating frequency. To ensure that this condition is satisfied, the cutoff frequency of the first higher-order mode is determined through electromagnetic finite element

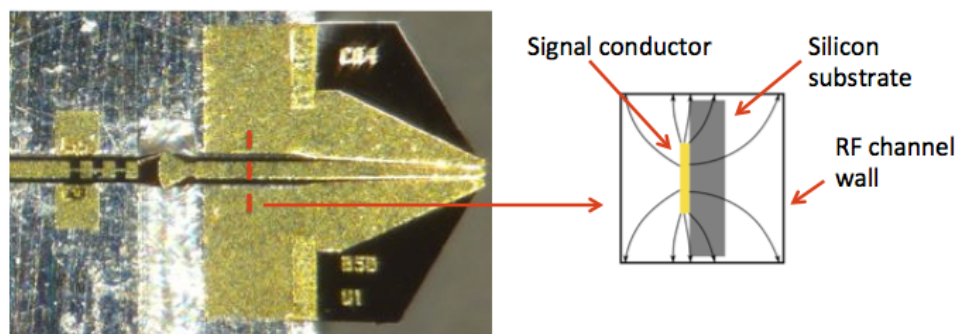


Figure 3.1: (left) Micrograph of a WR-1.2 probe chip mounted in one half of the split-block waveguide housing, prior to being clamped in place. The dashed red line marks the section view shown at right.

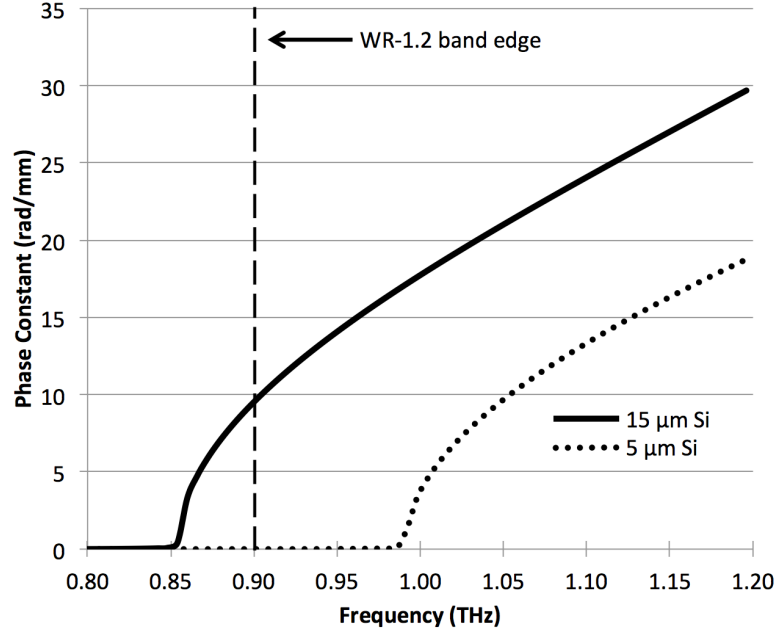


Figure 3.2: Cutoff frequency of the first spurious mode in the coaxial channel for 15 μm and 5 μm thick silicon substrates. Note that the upper edge of the WR-1.2 waveguide band is at 900 GHz.

simulation using ANSYS High Frequency Structure Simulator (HFSS).

The cutoff frequency of the higher-order modes depends on the substrate thickness and channel size. Reducing either dimension decreases the electrical size of the channel, thereby increasing the cutoff frequency of the higher-order modes. However, the minimum allowable channel width is limited by the smallest diameter endmill available to the machinist, which for this work, is 75 μm . To provide some margin over this requirement, the RF channel width is set to 80 μm . For this channel geometry, the phase constant for the first higher-order mode is determined through finite element simulation for both 15 and 5 μm substrates and the results are shown in Fig. 3.2. The first higher-order mode for a 15 μm substrate begins propagating within the WR-1.2 band, while for a 5 μm substrate, the first higher-order mode does not begin propagating until nearly 1 THz, providing a safety margin of ap-

proximately 10% over the WR-1.2 waveguide upper band edge (900 GHz). This analysis demonstrates that a 5 μm silicon substrate is electrically suitable for the RF channel of a WR-1.2 probe.

3.2 Mechanical Design Considerations

While electromagnetic simulation demonstrates that a 5 μm silicon substrate is electrically suitable for a WR-1.2 probe, the substrate must also satisfy mechanical requirements given that it forms the probes' contact points which physically touch the on-wafer device. The mechanical design requires: (1) the probe tip be long enough to extend below the bottom of the waveguide block housing with sufficient clearance to contact the on-wafer device and (2) that when the tip is brought into contact with the on-wafer device, the deflection generates sufficient force ($> 1\text{mN}$ per tip [13]) to create a low-resistance path between the probe and the on-wafer device. As the probe tip is rigidly fixed to the probe housing at one end, we may consider the probe tip as an end-loaded cantilever beam to evaluate the geometrical effects on the available contact force. For an end-loaded cantilever, a small deflection of the free end of the beam is defined by [27]:

$$d = \frac{F_{norm} l^3}{3 E I} \quad (3.1)$$

where F_{norm} is the normal force applied to the end of the beam, l is the length of the beam, E is the Young's modulus of silicon (185 GPa [17]), and I is the area moment of inertia, defined for a beam of rectangular cross section as:

$$I = \frac{w t^3}{12} \quad (3.2)$$

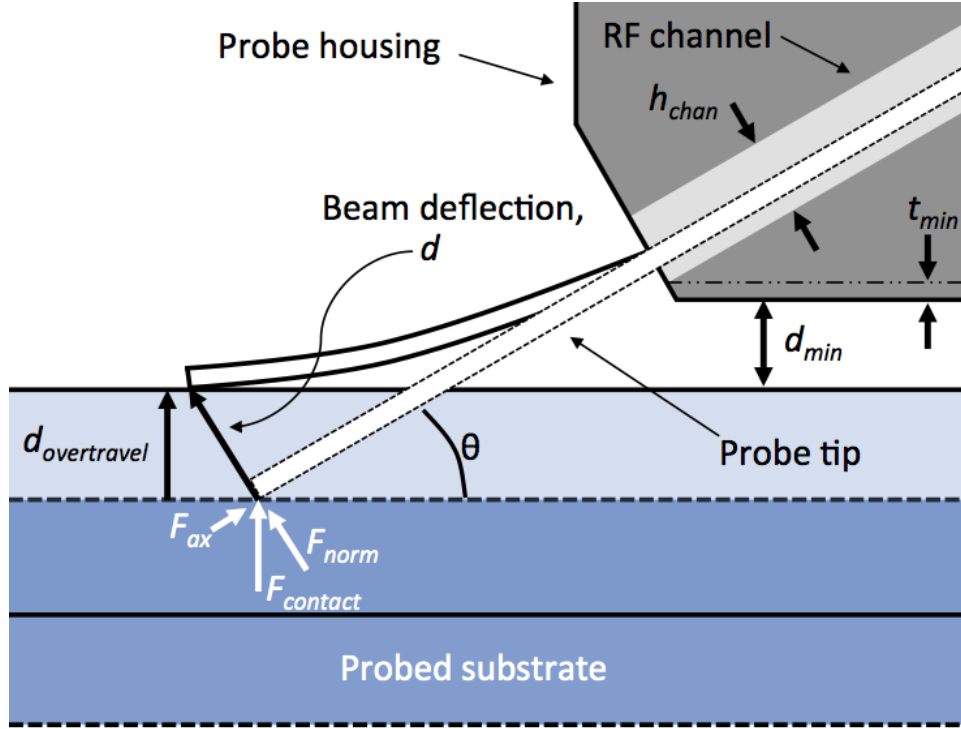


Figure 3.3: Profile view of probe contacting wafer on initial contact (dotted outlines) and after deflection (solid outlines).

where w is the beam width and t is the beam thickness. Because the probe contacts the test wafer at an angle θ , as shown in Fig. 3.3, the force normal to the beam is a component of the contact force, $F_{contact}$, where:

$$F_{norm} = F_{contact} \cos(\theta) \quad (3.3)$$

In using the probe for on-wafer measurements, we are interested in the force applied to the contact pads as the probe is brought into contact with the sample. Because contact is controlled through vertical relative movement of the sample stage or probe and the contact pads are parallel to the substrate surface, we are interested in the relationship between the vertical components of force and displacement. Therefore, referring to Fig. 3.3, we define the spring constant of the probe as the relation

between the vertical components:

$$k = \frac{F_{contact}}{d_{overtravel}} \quad (3.4)$$

where $d_{overtravel}$ is related to the deflection by:

$$d_{overtravel} = d \cos(\theta) \quad (3.5)$$

By combining Eqs. 3.1 through 3.5, the spring constant of the probe tip can be expressed as:

$$k = \frac{E w}{4 \cos^2(\theta)} \left(\frac{t}{l} \right)^3 \quad (3.6)$$

It is important to note that there is an axial component of force along the length of the probe tip. However, for the purposes of this analysis, this force is neglected as the compressive stress is assumed to be small and have a negligible effect on the deflection. This assumption will be verified through finite element simulation.

From Eq. 3.6, it is expected that simply reducing the substrate thickness t from 15 μm to 5 μm will reduce the spring constant of the tip by a factor of 27. Given that micromachined probes fabricated on 15 μm substrates exhibit a spring constant of approximately 0.7 milliNewtons per micrometer ($\text{mN}/\mu\text{m}$), it is expected that a micromachined probe fabricated on a 5 μm substrate in the same geometry will exhibit a spring constant of approximately 0.03 $\text{mN}/\mu\text{m}$. This would require a probe overtravel of 100 μm to reach the desired contact force of 1 mN per tip, which is approaching the maximum available overtravel of 110 μm , depicted in Fig. 3.3. As a result, the mechanical design involves optimization of the tip geometry to maximize the available contact force.

Eq. 3.6 shows that for a beam of fixed thickness, the length and width of the tip

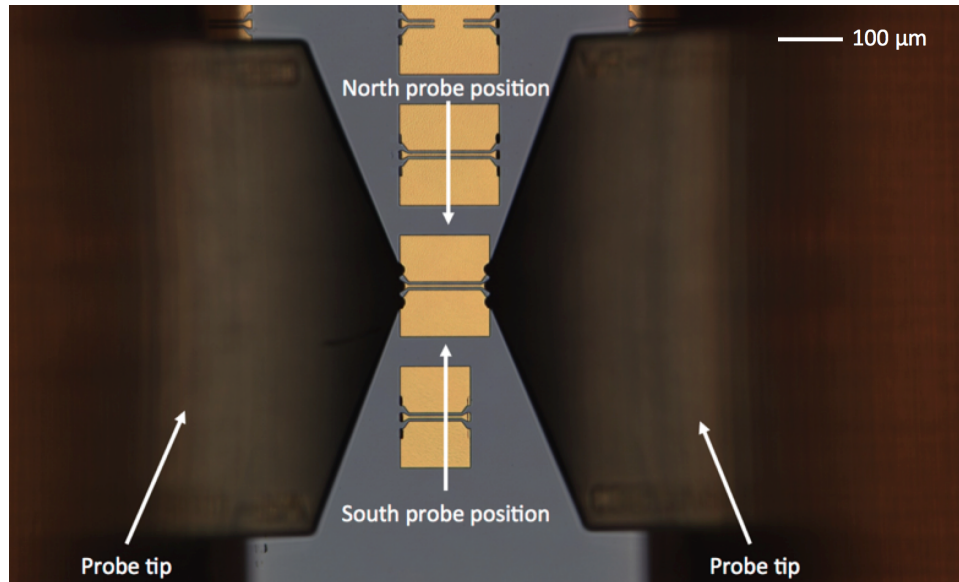


Figure 3.4: On-wafer view of micromachined probe tips contacting a CPW thru line. For some DUTs, low-frequency or DC probes may be needed in the North and/or South positions.

will control the spring constant. However, practical limitations exist with respect to both the length and width of the tip. From a practical standpoint, it is desirable to limit the probe tip width for several reasons. From a fabrication perspective, wide chips may result in low yield due to the larger amount of wafer real estate required as well as increased likelihood of damage while handling the chips. From a usage perspective, wide chips may limit accessibility to the on-wafer device by other probes (e.g. “north/south” DC bias probes), as illustrated in Fig. 3.4. Wider chips would also obstruct view of the wafer, possibly reducing on-wafer viewing image quality.

Reducing the probe tip length will also increase the spring constant, however there is a limitation in this parameter. Shortening the tip brings the bottom of the waveguide block closer to the probed substrate. This reduces the distance the tip can deflect before the block contacts the substrate and therefore reduces the

maximum force that can be generated at the tip. It is anticipated that there would therefore be an optimal length that maximizes the available contact force.

To analyze the available contact force, we consider the contact geometry shown in Fig. 3.3. The maximum overtravel is limited by the geometry of the probe tip and housing and can be expressed as:

$$d_{max} = l \sin(\theta) - t_{min} - \frac{h_{chan}}{2} \cos(\theta) - d_{min} \quad (3.7)$$

where l is the tip length, θ is the contact angle, t_{min} is minimum thickness of the waveguide block, h_{chan} is the RF channel height. To prevent the waveguide block from contacting and damaging the wafer sample, we allocate a minimum clearance, d_{min} , between the housing and the wafer when the maximum overtravel is used. By combining Eqs. 3.7 and 3.6, the maximum contact force for a given tip geometry can then be expressed as:

$$F_{max} = k d_{max} = \frac{E w t^3}{4 \cos^2(\theta)} \left[\frac{\sin(\theta)}{l^2} - \frac{t_{min} + \frac{h_{chan}}{2} \cos(\theta) + d_{min}}{l^3} \right] \quad (3.8)$$

By differentiating Eq. 3.8 with respect to l to find the maximum F_{max} , we find that the maximum available contact force occurs for a tip length of:

$$l_{opt} = \frac{3}{2} \frac{t_{min} + \frac{h_{chan}}{2} \cos(\theta) + d_{min}}{\sin(\theta)} \quad (3.9)$$

For this work, θ is 30° , t_{min} is $40 \mu\text{m}$, h_{chan} is $80 \mu\text{m}$, and d_{min} is $25 \mu\text{m}$, resulting in an optimal length of $299 \mu\text{m}$ and, from Eq. 3.7, a maximum overtravel of $42 \mu\text{m}$. Evaluating Eq. 3.6 under these conditions, a beam $5 \mu\text{m}$ thick and $750 \mu\text{m}$ wide would result in a spring constant of $0.26 \text{ mN}/\mu\text{m}$. To confirm Eq. 3.9, we plot

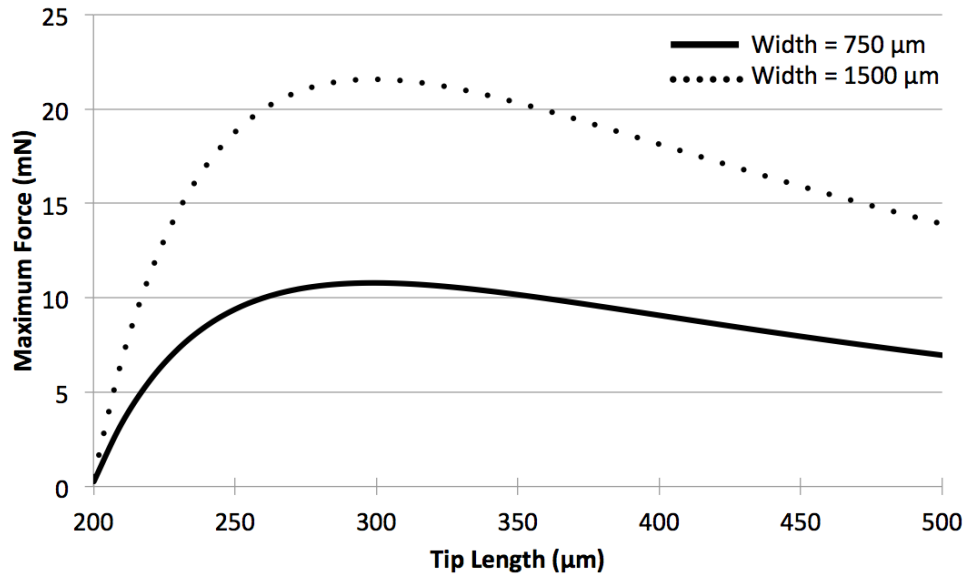


Figure 3.5: Maximum available contact force (Eq. 3.8) versus beam length. Beam widths of 750 and 1500 μm are shown.

the maximum force versus tip length, shown in Fig. 3.5, which confirms that the optimal length is approximately 300 μm .

While this beam analysis provides insight into the probe tip mechanics, because the probe tip is tapered, the spring constant is only an approximation. To take into account the true geometry of the probe chip, the mechanical design proceeds through finite element simulation using this analysis as a starting point.

3.3 Mechanical Simulations

Before proceeding with the probe chip design, we verify finite element simulations against the rectangular beam analysis. To make this comparison, in the simulation model, a vertical force of 1mN is applied to the end of an angled rectangular beam, as shown in Fig. 3.6, and the resulting vertical displacement used to calculate the spring constant (Eq. 3.4). The simulation is repeated for several tip lengths,

widths, and angles, and the spring constants are compared against the calculated values (Eq. 3.6) in Fig. 3.6, which indicate good agreement over various geometries. Note that a larger probe chip angle is not under consideration for this design due to impact on the waveguide interface discontinuity discussed in Chapter 1. However, it is included in this analysis to further confirm the angular dependence of the spring constant.

In the beam analysis discussed in the previous section, the axial force was neglected on the assumption that it has little effect on the spring constant and induces little additional stress. To verify this assumption, we repeat the spring constant simulation with only the normal force applied. For comparison, the beam geometry is set to $w = 750 \mu\text{m}$, $l = 250 \mu\text{m}$, and $\theta = 30^\circ$. At this contact angle, a vertical force of 1 mN has a normal component of 0.866 mN. With only this normal component applied, simulation shows a vertical deflection of $2.56 \mu\text{m}$ and a maximum stress of 61.6 MPa. This compares closely with the results of 1 mN vertical force, which

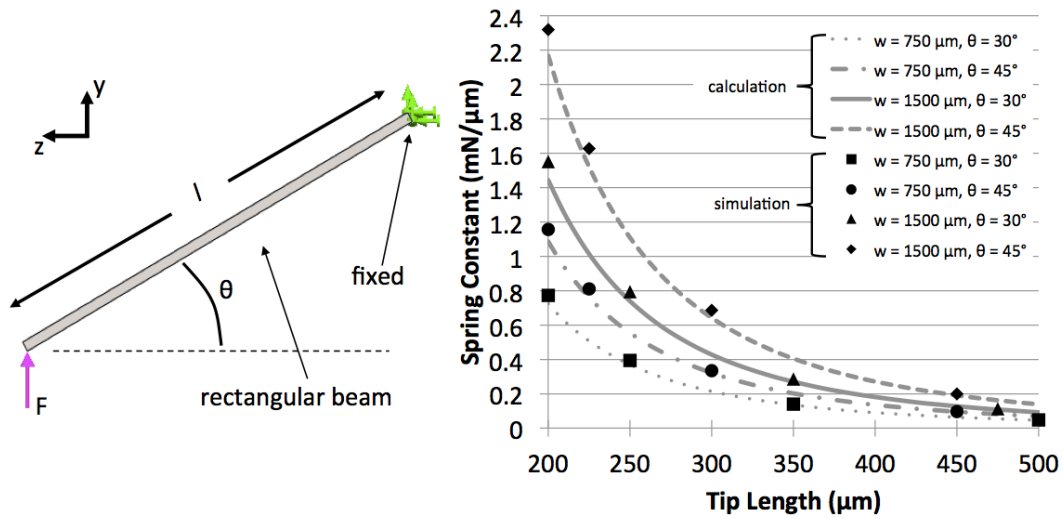


Figure 3.6: Comparison of calculated and simulated vertical spring constants for angled rectangular beam. Left: simulation model, where the beam width, w , lies along the x -direction. Right: calculated and simulated results for various beam geometries.

produces a vertical deflection of $2.55 \mu\text{m}$ and a maximum stress of 61.7 MPa . This confirms that the axial force has little impact on the vertical spring constant and may be neglected for the rectangular beam analysis.

Finite element simulation is now used to capture the effect of the true probe chip geometry. Shown in Fig. 3.7, the tip includes a taper and fillets are used to isolate the intermediate transmission line from the clamping regions. The spring constants for various tip lengths and widths are determined through finite element simulation and are shown in Fig. 3.8 along with the corresponding maximum force. The results show that optimum lengths occur in the vicinity of 400 and $450 \mu\text{m}$ for tip widths of 750 and $1500 \mu\text{m}$, respectively. For simplicity of design and use, however, a single tip length is desired. The tip length is chosen to be $400 \mu\text{m}$, which provides 5.4 mN maximum force for the $750 \mu\text{m}$ wide tip. At double the width, the $1500 \mu\text{m}$ wide tip provides a modest one-third increase, providing 7.2 mN of maximum force. Note the impact of choosing a single length is small: the difference in these maximum forces from the optimal values is less than 0.2 mN .

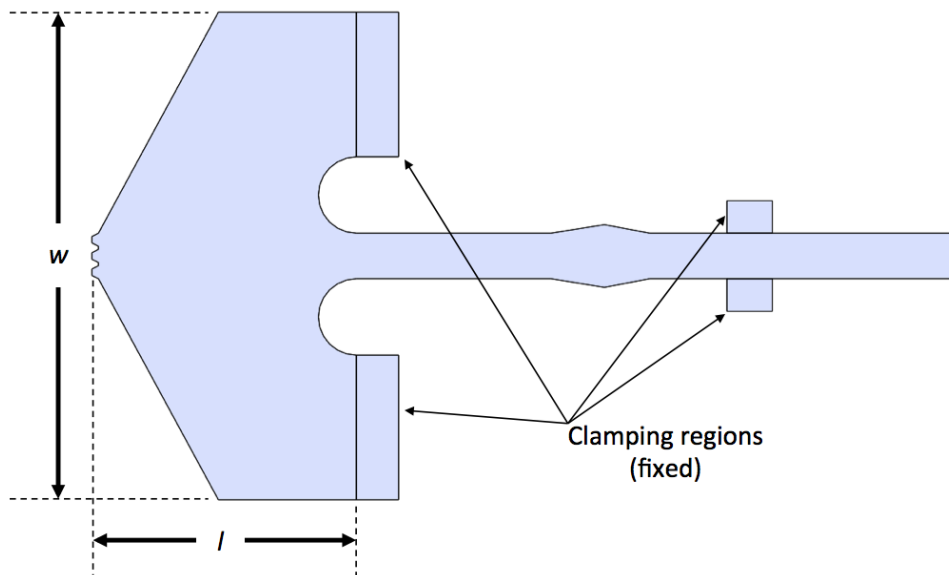


Figure 3.7: Probe tip geometry for finite element simulation.

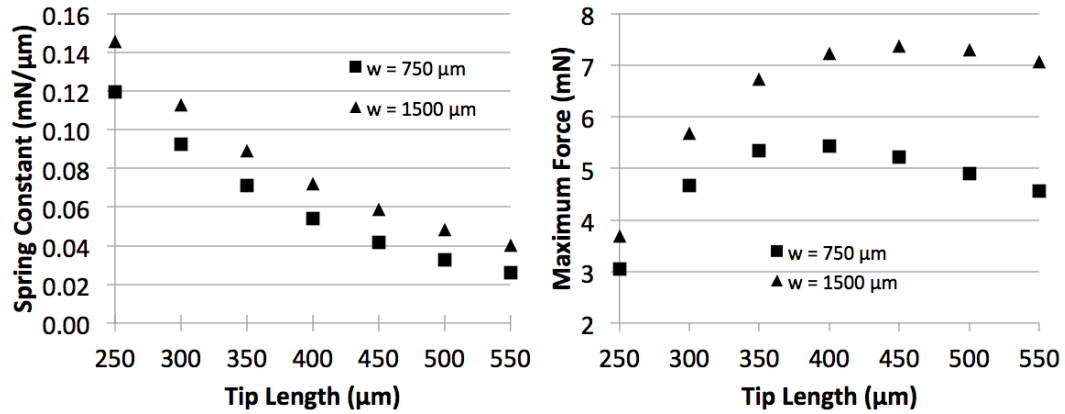


Figure 3.8: Finite element simulation results for probe tips widths of 750 and 1500 μm . Left: spring constant versus tip length. Right: maximum force versus tip length.

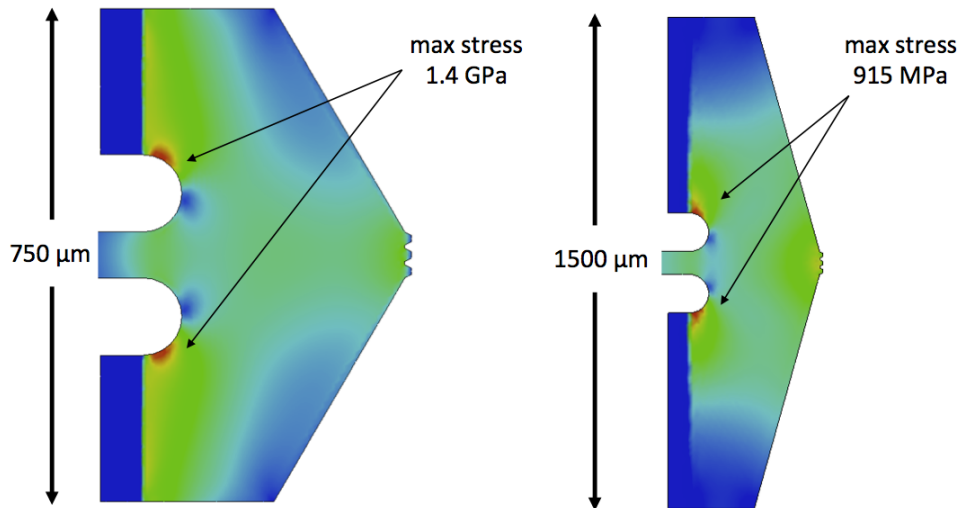


Figure 3.9: Stress profiles from finite element simulation. Left: 750 μm wide x 400 μm long probe chip under 5.4 mN load. Maximum stress marker indicates 1.4 GPa. Right: 1500 μm wide x 400 μm long probe chip under 7.2 mN load. Maximum stress marker indicates 915 MPa.

To verify that the stresses resulting from these contact forces are below the yield strength, the maximum force is applied vertically to the probe tip through simulation. Fig. 3.9 shows the stress profiles of the 750 μm and 1500 μm wide tip under 5.4 and 7.2 mN loads, respectively. The markers indicate a maximum stress

of 1.4 GPa for the 750 μm wide tip, and 915 MPa for the 1500 μm wide tip. The maximum of 1.4 GPa is 3.5 times lower than the yield strength of approximately 5 GPa [17], suggesting the designs can withstand the maximum force.

3.4 RF Design

The RF design of the probe is performed through finite element simulation using HFSS. Initially, the waveguide to coaxial transition, which utilizes a radial stub due to its broadband characteristics [28], is optimized. The stub radius, stub angle, and waveguide backshort length, shown in Fig. 3.10, are iteratively varied to minimize the insertion loss and maximize the return loss of the transition. After optimization, the stub radius is chosen to be 75 μm , the stub angle 40°, and the waveguide backshort distance 120 μm . Finally, simulations are performed in two frequency ranges: 500 - 750 GHz (WR-1.5) and 750 - 975 GHz (WR-1.0) to permit comparison with measured data, as described in the RF measurement section. For all of the

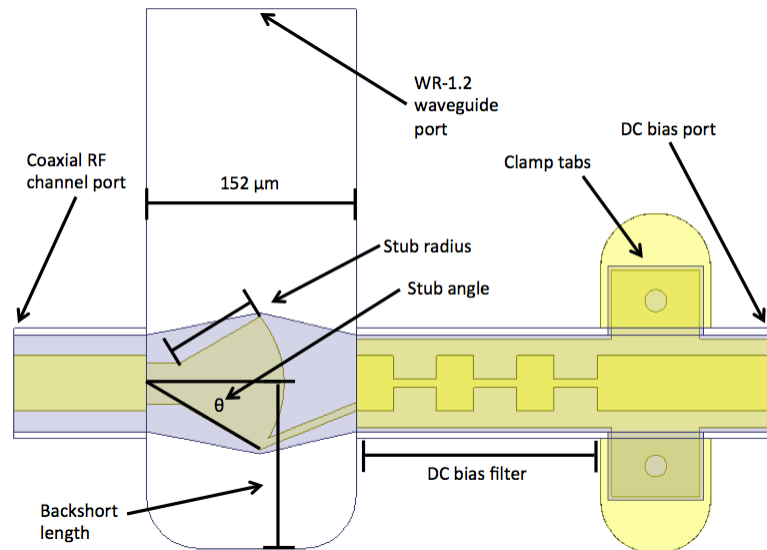


Figure 3.10: HFSS simulation model for the WR-1.2 waveguide to coaxial transition.

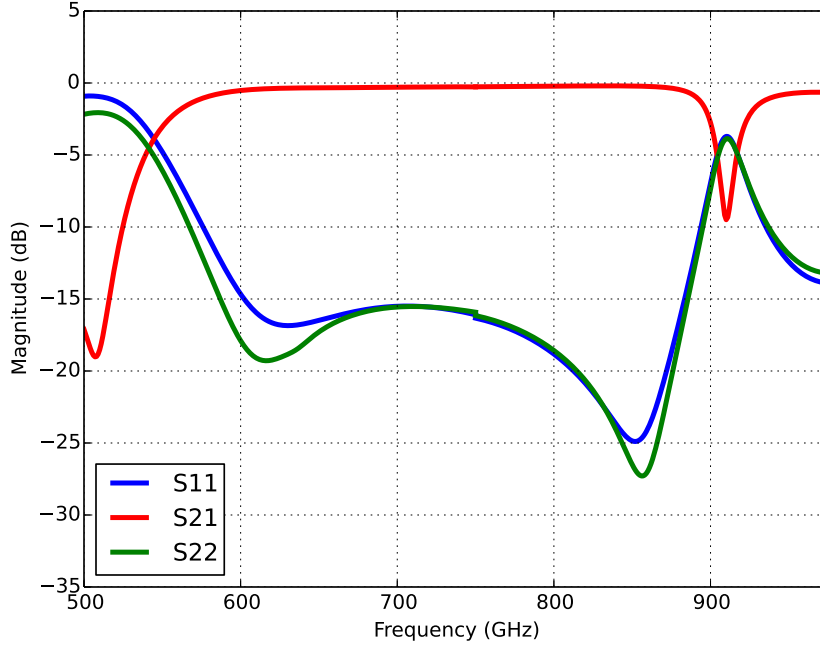


Figure 3.11: HFSS simulation results for the WR-1.2 waveguide to coaxial transition. Port 1 is the WR-1.2 waveguide, Port 2 is the coaxial channel. Note the simulation is limited to 975 GHz to maintain single-mode propagation in the WR-1.2 waveguide.

WR-1.2 simulations, the probe chip metallization is $1.0 \mu\text{m}$ of soft gold capped with $1.0 \mu\text{m}$ cobalt-hardened gold. Measurements of the conductivities of these metals were performed in the University of Virginia cleanroom [25] and were reported to be 3.2×10^7 Siemens per meter (S/m) and 5.8×10^6 S/m, respectively. The on-wafer CPW is $1.0 \mu\text{m}$ of soft gold and the waveguide channel housing walls are aluminum alloy 6061-T6 with conductivity of 2.5×10^7 S/m and surface roughness of 100 nm, based on the RMS value obtained from a Veeco NT1100 optical profilometer. The simulated S-parameters are shown in Fig. 3.11, indicating a return loss from the waveguide and CPW ports (S_{11} and S_{22}) greater than 15 dB for most of the WR-1.2 waveguide band. The resonance in the insertion loss (S_{21}) just above 900 GHz is due to the floating ground of the microstrip DC bias filter. Because the filter is

suspended in the channel, the ground metallization on the probe chip only contacts the housing at the clamping tab regions. As a result, there are standing wave effects on the microstrip ground that cause periodic resonances. By reducing the distance between the waveguide and the clamp tabs, the electrical length between the beginning of the filter and the grounding point at the clamp tabs decreases, increasing the resonant frequency. However, moving the clamp tabs too close to the waveguide disturbs the performance of the transition and filter. This effect was not well understood at the time of the design, and despite the close proximity of the resonance to the 900 GHz WR-1.2 band edge, it represented the best performance achieved at the time. Based on this effect, it is recommended for future designs that the filter be designed without an on-chip floating ground. As discussed in Chapter 4, the WR-1.0 probe implements such a filter, and does not show this type of resonance.

The coaxial to on-wafer CPW transition portion of the probe chip is designed

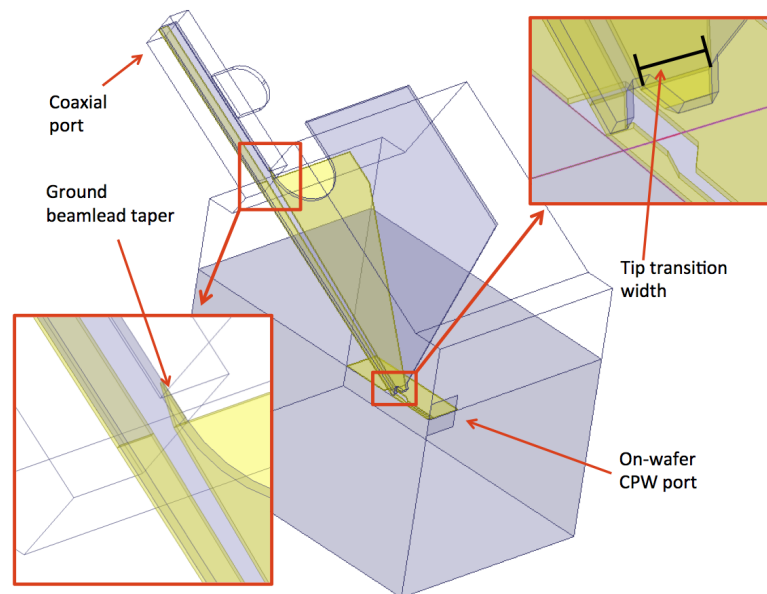


Figure 3.12: HFSS simulation model for the WR-1.2 coaxial channel to on-wafer CPW transition.

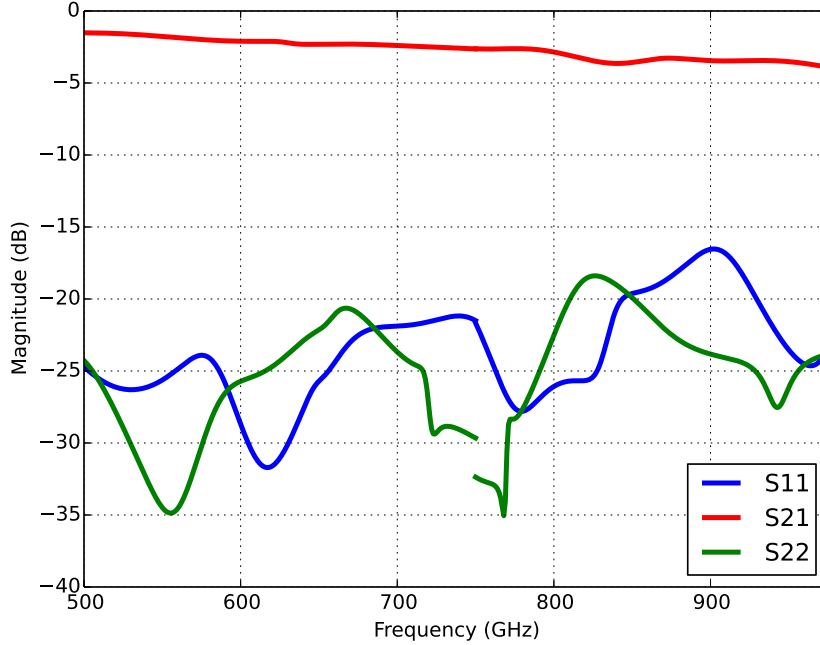


Figure 3.13: HFSS simulation results for the WR-1.2 coaxial to on-wafer CPW transition. Port 1 is the coaxial channel, Port 2 is the on-wafer CPW. The discontinuity at 750 GHz is due to combining two simulation sweeps (500-750 and 750-975 GHz). Numerically, the discontinuity step size is quite small and is considered to be an acceptable level of simulation error.

through finite element simulation. The simulation model is shown in Fig. 3.12, where symmetry is exploited and half of the full model is analyzed. Due to the symmetrical geometry of the tip, the model can be divided in half by placing a magnetic conducting boundary condition along the symmetry plane. Radiation boundary conditions are applied around the remaining surfaces to account for any radiation losses. To optimize this transition, two features are considered. First, there is a discontinuity where the tip emerges from the channel as the field components can no longer terminate on the waveguide block housing. To reduce the reflection at this discontinuity, a smooth taper of the ground beamleads is implemented as shown in Fig. 3.12. In addition, small tuning of the CPW tip transition

width can improve coupling to the $50\ \Omega$ on-wafer CPW environment. After optimization, the tip transition width is $20\ \mu\text{m}$ and the ground beamlead taper is $7\ \mu\text{m}$ wide by $20\ \mu\text{m}$ long, and the simulated performance of the transition is shown in Fig. 3.13.

The last segment of the RF simulation concerns the rectangular waveguide channel and interface, and while it is not a design aspect, it has a significant effect on performance of the probe. Shown in Fig. 3.14a, the rectangular waveguide channel follows the E-plane split of the waveguide housing. Because it would be difficult or complex to machine a waveguide bend along the split plane, the probe waveguide channel is simply cut flush vertically at the waveguide interface. As a result, there is a 30 degree H-plane junction, creating a step discontinuity. Fig. 3.14a shows a simulation model of this junction, where the waveguide port is de-embedded by 20

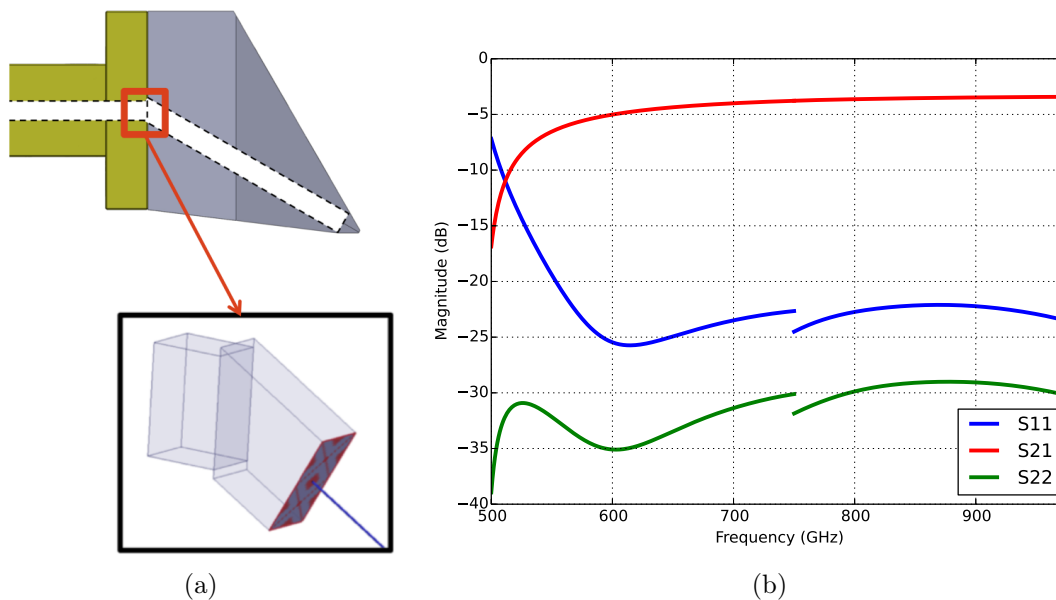


Figure 3.14: HFSS simulation of WR-1.2 H-plane junction (a) simulated model, (b) Simulated response. Port 1 is the test port (either WR-1.5 or WR-1.0), probe WR-1.2 waveguide. The discontinuity at 750 GHz is expected as the mismatch between probe's WR-1.2 waveguide input and a WR-1.5 or WR-1.0 test port is different.

mm. The simulation captures two important effects. The first is that it accounts for the loss of the waveguide section between the probe waveguide interface and waveguide transition at the tip. Second, while the mismatch is relatively small (return loss less than 22 dB across the band) it does have a noticeable impact on the probe S-parameters due to the standing wave it m,creates between the interface and radial stub waveguide transition.

By combining the previous three simulation results, the expected full performance of the probe is obtained and is shown in Fig. 3.15. The simulated insertion loss is less than 10.0 dB and the simulated return loss is greater than 11.8 dB over the WR-1.2 band.

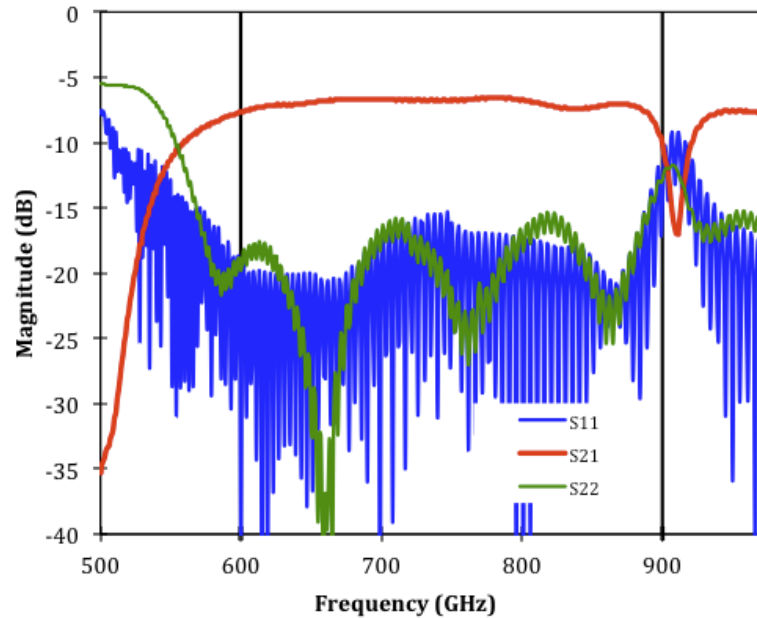


Figure 3.15: HFSS simulation results for the full WR-1.2 probe. Port 1 is the WR-1.2 waveguide input of the probe, Port 2 is the on-wafer CPW.

3.5 Mechanical Characterization

As described previously, when the probe chip is clamped between the two halves of the split-block housing, the tip constitutes a cantilever beam. As the tip is brought into contact with the test wafer, it deflects and generates a force at the contact points. To determine the effective spring constant of the tip, an experimental setup utilizing a load cell (Futek[®] FSH0234) and precision motor stage is used. A diagram of this setup is shown in Fig. 3.16a. The motor stage is raised in 2 μm increments. After each step, the force reading from the load cell and the position of the precision motor stage are both recorded. As the test wafer makes contact with the probe tip, both the load cell and the probe tip deflect, representing two series-connected springs. By separately measuring the spring constant of the load cell, k_2 , the spring constant of the probe tip, k_1 , can be determined. The results of this experiment are shown in Fig. 3.16b, which indicate that the probe tip spring constant

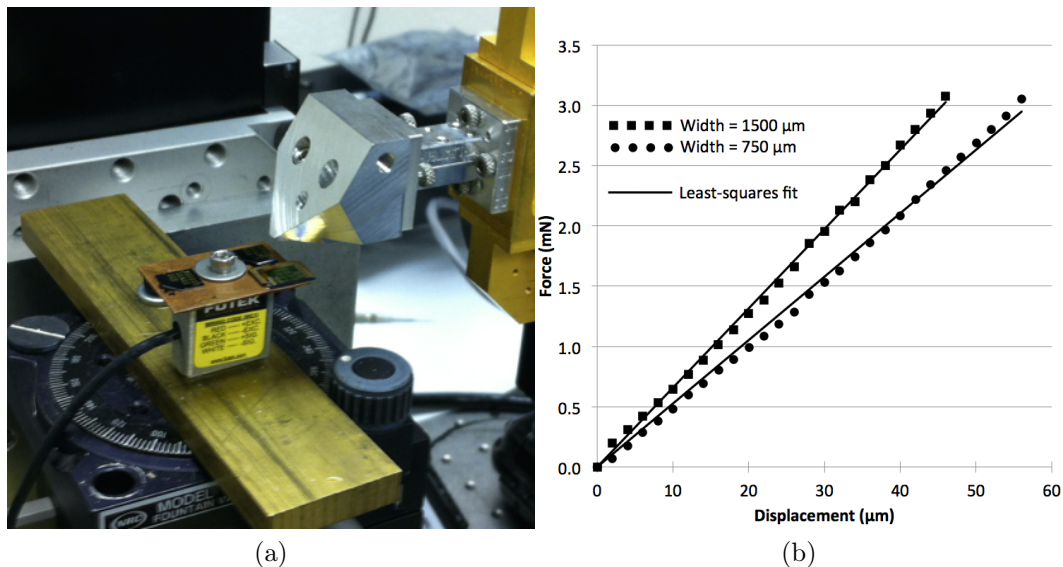


Figure 3.16: Mechanical test setup. (a) Mechanical test setup used to determine the effective spring constant of the probe tip. (b) Measurement results of the spring constant mechanical test.

Table 3.1: Comparison of spring constants (mN/ μm)

	w = 750 μm		w = 1500 μm	
	t = 5.5 μm	t = 5.0 μm	t = 5.5 μm	t = 5.0 μm
Beam Calculation	0.098	0.074	0.196	0.147
ANSYS Simulation	0.058	0.044	0.068	0.052
Measurement	0.053 \pm 0.00084		0.066 \pm 0.00081	

is $k_1 = 0.053 \pm 0.00084$ mN/ μm for the 750 μm wide tip and $k_1 = 0.066 \pm 0.00081$ mN/ μm for the 1500 μm wide tip. Shown in Table 3.1, the measured values are significantly lower than simulated values, assuming a 5.0 μm substrate thickness. To determine the actual thickness, the probe chips substrate was measured using a Veeco NT1100 optical profilometer and found to be approximately 5.5 μm thick (within the manufacturer's specification of 5.0 \pm 0.5 μm).

To take this thickness into account, the finite element simulations and beam calculations were also performed assuming a 5.5 μm substrate thickness and these results are shown in Table 3.1. The measured and simulated spring constant values agree well for the case of 5.5 μm substrate thickness. Additionally, the improved spring constant of the 1500 μm wide tip is in agreement with prediction. However, the values from the beam calculation are higher than the measured values as unlike the simulations, the beam calculations do not capture the effect of the tapered tip. This discrepancy is attributed to the fact that the probe tip is not actually a rectangular beam and that the tapered width reduces the spring constant.

3.6 Mechanical Failure

To test the failure point of the 5.5 μm silicon tip, the force-displacement test described in the previous section is repeated with the 750 μm wide probe tip. To do so, the probe tip is positioned at approximately 50 - 100 μm from the edge of the

test wafer, as shown in Fig. 3.17. This is to compensate for the fact that when the probe housing is positioned normally over a test wafer, the $400\ \mu\text{m}$ long tip results in a maximum vertical displacement of $125\ \mu\text{m}$ before the bottom of the probe housing contacts the wafer. By placing the tip at the edge of the wafer, displacements greater than $150\ \mu\text{m}$ are possible.

The result of the force-displacement test is shown Fig. 3.18, which indicates failure at approximately $24\ \text{mN}$ contact force and $260\ \mu\text{m}$ displacement. For comparison, a finite element simulation is run with a force of $24\ \text{mN}$ applied to the tip. The resulting stress is $5.1\ \text{GPa}$ at $351\ \mu\text{m}$ vertical deflection, shown in Fig. 3.19. This stress values agrees well with published values of approximately $5\ \text{GPa}$ yield stress [17]. However, the figure shows that this deformation is not possible unless there is no overlap between the tip and the probed substrate and the discrepancy in displacement is therefore attributed to the fact that the probe tip is not precisely at the edge of the wafer. Referring to Fig. 3.17, as the deflection increases, the corner of the substrate will at some point contact the probe tip, effectively creating

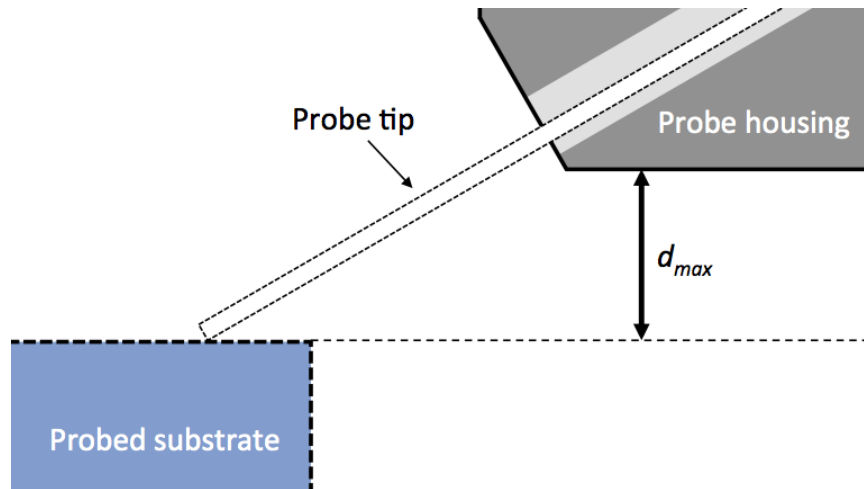


Figure 3.17: Test setup for mechanical failure. Landing the probe tip at the edge of the wafer allows for vertical displacements greater than the initial clearance between the probe housing and probed substrate, d_{max} .

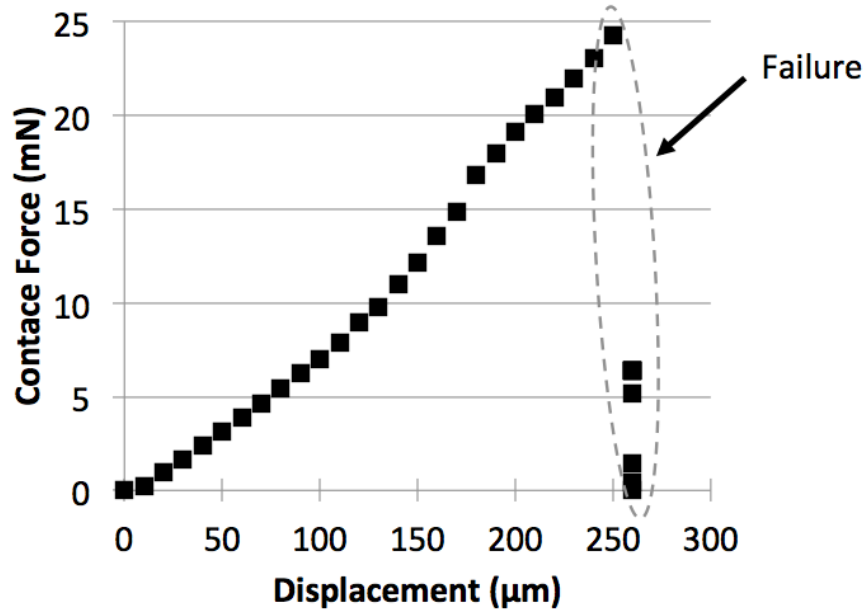


Figure 3.18: Force-displacement curve for failure of $750\ \mu\text{m}$ wide probe chip, which occurs at approximately 24 mN.

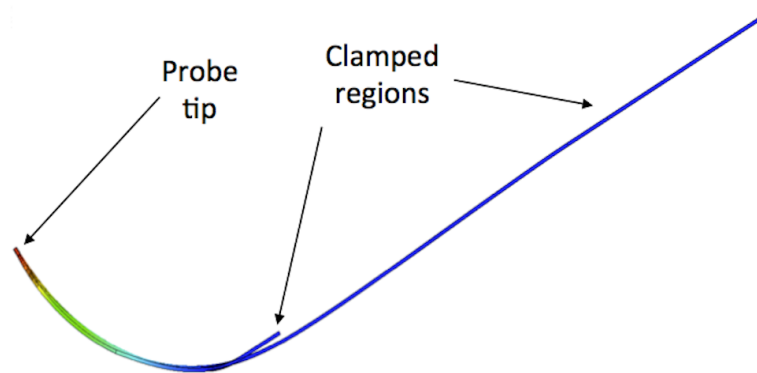


Figure 3.19: True scale profile view of probe tip under 24 mN load indicating $351\ \mu\text{m}$ deflection.

a shorter tip length and thereby increasing the spring constant. In addition, the probed substrate was a silicon fragment that was cut with a dicing saw. As a result, the probed substrate edge was irregular, the effect of which would be difficult to take into account.

3.7 RF Characterization

Because WR-1.2 is a “cross band” (overlapping the WR-1.5 and WR-1.0 bands), frequency extension modules for S-parameter measurements in this band are not common and the University of Virginia does not house a WR-1.2 frequency extension module. To test the WR-1.2 probe, separate measurements are performed in the WR-1.5 (500 - 750 GHz) and WR-1.0 (750 - 1100 GHz) waveguide bands to characterize the probe over the full 600 - 900 GHz range. As a result, the 30 degree H-plane junction described in the previous section is not between two WR-1.2 waveguide sections, but rather between the probe’s WR-1.2 waveguide and the frequency extender’s WR-1.5 or WR-1.0 waveguide. The return loss due to this mismatch is less than 22 dB across the WR-1.2 band and the effect is included in both measured and simulated data. To determine the probe’s full two-port S-parameters with a one-port measurement setup, a two-tier calibration technique [29, 30] is utilized. This technique consists of performing calibrations at reference planes on each side of the device.

The one-port S-parameter measurement setup is shown in Fig. 3.20a and consists of a Virginia Diodes, Inc. (VDI) vector network analyzer extension module connected to an Agilent PNA-X (N5245A) vector network analyzer (VNA). The frequency extender is mounted to a Cascade Microtech PA200 commercial probe station for positioning. The polarization of the probe’s waveguide input is at a 90 degree angle relative to the that of the frequency extender’s waveguide output. Thus, to couple the signal from the frequency extender to the probe, a micromachined 90 degree WR-1.2 waveguide twist (illustrated in Fig. 3.20b) is used to rotate the polarization. The waveguide twist design has been described previously [26] and was was designed and fabricated for the WR-1.2 work by Qiang Yu and Naser Ali-

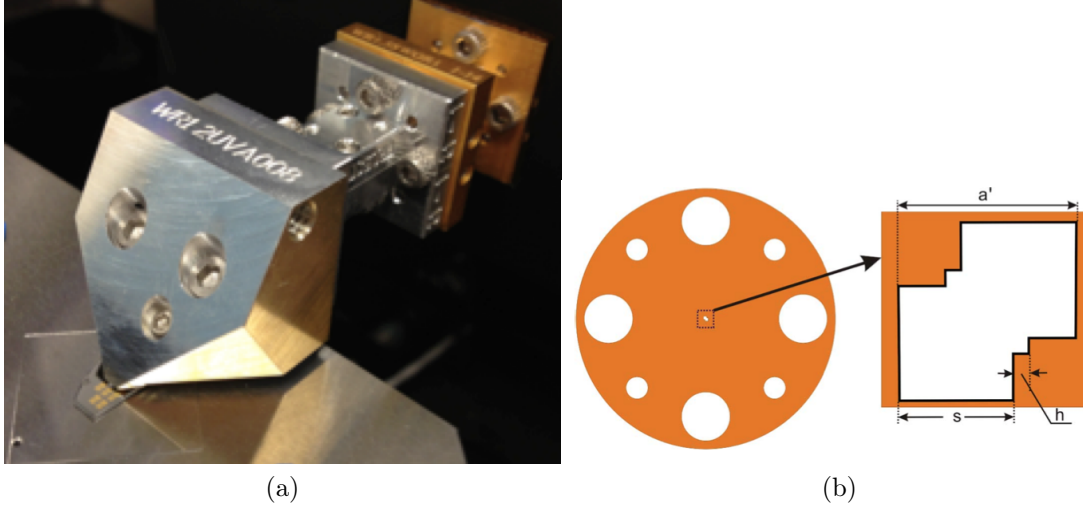


Figure 3.20: (a) The WR-1.2 micromachined probe mounted to the VDI frequency extender. The probe is contacting the calibration substrate for the on-wafer second tier calibration. (b) WR-1.2 waveguide twist shim diagram ($s = 75 \mu\text{m}$, $h = 21 \mu\text{m}$, $a' = 253 \mu\text{m}$, thickness = $198 \mu\text{m}$).

jabbari.

The first tier calibration is performed at the waveguide test port output of the frequency extender using a waveguide short, delay short, and precision load from the VDI waveguide calibration kit. The calibration error model is shown in Fig. 3.21, where the measured reflection coefficient of each standard can be expressed in terms of the complex error coefficients:

$$\Gamma_{meas} = e_{00} + \frac{e_{10}e_{01}\Gamma_{true}}{1 - e_{11}\Gamma_{true}} \quad (3.10)$$

where Γ_{meas} is the measured reflection coefficient, Γ_{true} is the true reflection coefficient, e_{00} is the directivity error, $e_{01}e_{10}$ is the reflection tracking error, and e_{11} is the source match error. Eq. 3.10 can be rewritten as :

$$e_{00} - \Delta_e \Gamma_{true} + e_{11}\Gamma_{true}\Gamma_{meas} = \Gamma_{meas} \quad (3.11)$$

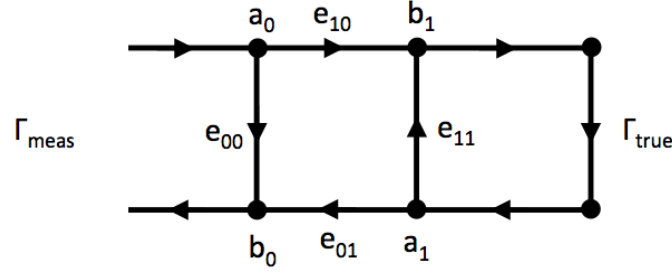


Figure 3.21: One port calibration error model. GA is the true reflection coefficient of the DUT, which is distorted by imperfect directivity (e_{00}), source match (e_{11}), and reflection tracking ($e_{10} \cdot e_{01}$).

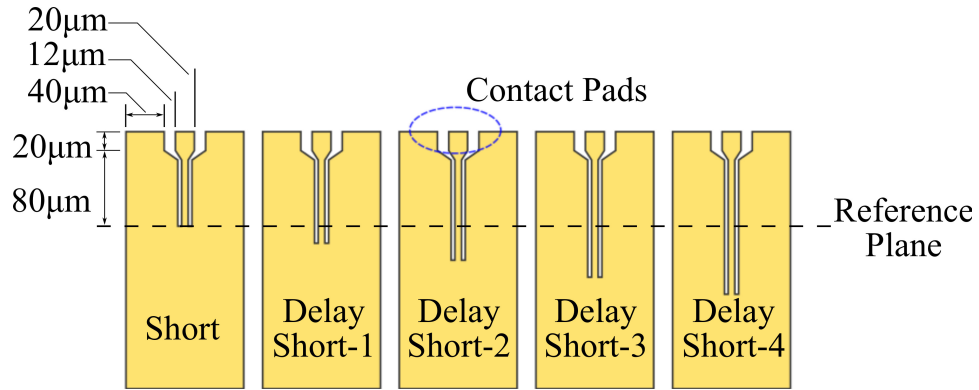


Figure 3.22: Layout of the CPW calibration standards. The CPW gap width is $5 \mu\text{m}$ and the signal line width is $10 \mu\text{m}$.

where:

$$\Delta_e = (e_{00}e_{11} - e_{10}e_{01}) \tag{3.12}$$

Measuring the response of the three known standards yields three equations, allowing the three unknown error coefficients e_{00} , Δ_e , and e_{11} to be determined. After determining the error coefficients, the measured reflection coefficient of a device can be transformed to its true reflection coefficient using Eq. 3.10.

After the waveguide calibration, the probe is attached to the waveguide test port for the second-tier calibration, which is performed on-wafer. The calibration

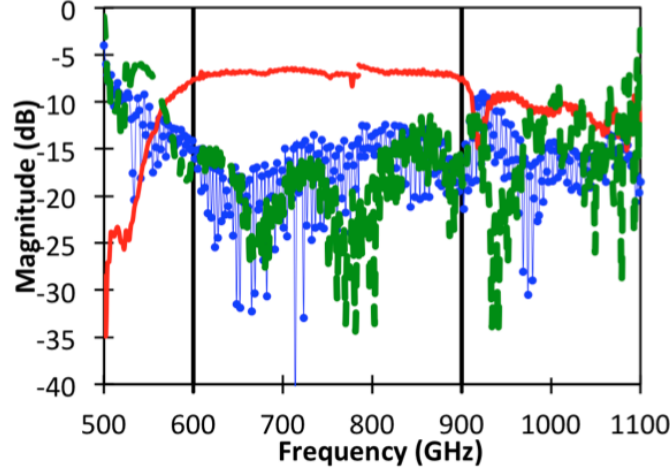


Figure 3.23: De-embedded probe S-parameters combined from the WR-1.5 and WR-1.0 calibrations. The vertical bars indicate the WR-1.2 frequency band edges. The calibrations are combined at 780 GHz, resulting in a discontinuity at that frequency point.

Table 3.2: Loss breakdown @ 750 GHz

	Loss (dB)
20.3 mm WR-1.2 waveguide	3.8
Waveguide to coax transition	0.3
Coax to on-wafer CPW transition	2.6
Total	6.7
Measured	7.2

standards consist of a CPW short and four delay shorts, as shown in 3.22, which are fabricated with $1.2 \mu\text{m}$ of electroplated soft gold metallization on a $275 \mu\text{m}$ thick, high resistivity ($>10 \text{ k}\Omega\text{-cm}$) silicon substrate. The reference plane is offset from the contact pads by $60 \mu\text{m}$, and each delay short is $15 \mu\text{m}$ longer than the previous. Electrically, this $15 \mu\text{m}$ length represents 35° at 750 GHz so that the longest delay short is 140° long at 750 GHz. To accommodate the probe tip pitch of $25 \mu\text{m}$, the contact pads have a center width of $16 \mu\text{m}$ and a gap width of $9 \mu\text{m}$. After measuring each standard, a least-squares fit [29, 31] is used to calculate the second tier error terms, which are the S-parameters of the network between the waveguide

test port and the on-wafer reference plane, in other words, the probe. To cover the WR-1.2 frequency range, this two-tier process is performed twice: first with a WR-1.5 frequency extension module (VDI WR1.5-VNAX TxRx), then second with a WR-1.0 module (VDI WR1.0-VNAX TxRx). The results from these two measurement setups are combined and are shown in Fig. 3.23. Over the 600 – 900 GHz frequency range, the measured insertion loss is less than 8.4 dB and the measured return loss is greater than 11.4 dB. Table 3.2 illustrates the sources of loss from the previously described simulations at 750 GHz. As shown, the measured loss is within 0.5 dB of the anticipated total.

As a verification of the calibration and probe performance, the on-wafer calibration standards are re-measured. The error-corrected responses are shown in Fig. 3.24 and agree well with the ideal response.

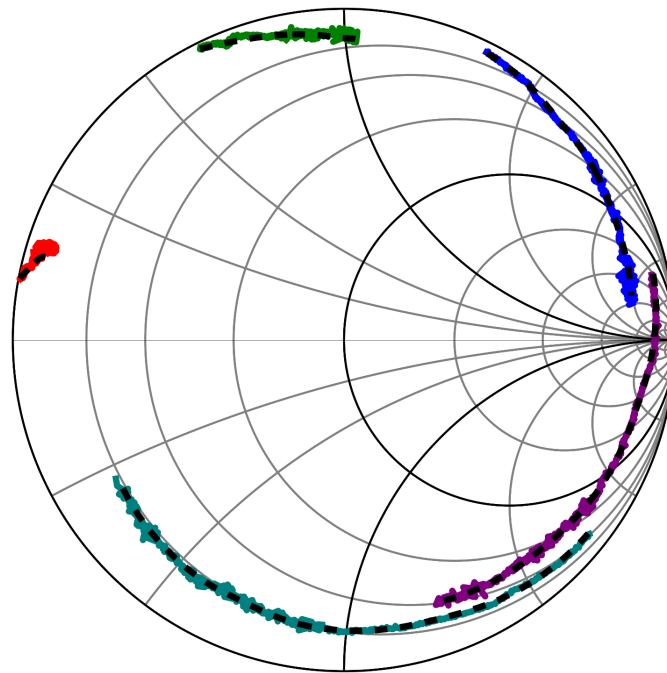


Figure 3.24: Re-measured S-Parameters of the on-wafer calibration standards from 600 – 900 GHz. The dashed dark lines indicated the ideal response.

3.8 Conclusion

A micromachined on-wafer probe has been demonstrated for the WR-1.2 waveguide band (600 - 900 GHz) on a 5 μm silicon substrate. The RF performance of the probe agrees well with simulation, yielding a measured insertion loss of less than 8.5 dB, and a return loss of greater than 11.4 dB over the full waveguide band. The mechanical performance of the probe tip also agrees well with simulation, exhibiting an effective spring constant of 0.053 and 0.066 mN/ μm for the 750 and 1500 μm wide chips, respectively. This work contributes: (1) the design of an on-wafer probe for WR-1.2 waveguide, which enabled on-wafer measurements above 750 GHz for the first time and (2) demonstration for the first time the use of a 5 μm silicon substrate as a mechanical substrate for submillimeter-wave contact measurements, and (3) analysis for maximization of available contract force. This work represents an important step towards extending on-wafer measurements to terahertz frequencies.

Chapter 4

Design, Characterization, and

Application of

WR-1.0 Micromachined Probes

Substantial progress has been made recently in the development of integrated circuits in the WR-1.5 waveguide band [4–6, 32, 33]. To enable continued development of such circuits in the 750 GHz to 1.1 THz frequency range, an on-wafer probe for the WR-1.0 waveguide band is developed for the first time. While work on the WR-1.2 probes demonstrated that it is possible to implement micromachined probes on a thinner silicon substrate, there are a number of drawbacks associated with thinner substrates. To address these issues, the WR-1.0 (750 GHz - 1.1 THz) probe design process closely analyzes the electrical requirements to assess the feasibility of using thicker substrates. This chapter presents the results of this study, the design and characterization of the first WR-1.0 on-wafer probe, and demonstration of the first on-wafer measurements above 1 THz.

4.1 Thin Silicon Drawbacks

There are a number of drawbacks with using thin substrates for micromachined probes, as discussed in detail below.

1. Increased deflection of the tip: With any on-wafer probe, as the tip makes contact with the on-wafer device, it deflects and moves forward, or “skates”, along the contact pads. This distance the tip travels along the pad is often called the “scrub length” or “skate length.” At a given contact force, thinner silicon probe tips exhibit more skate due to the increased deflection that results from the lower spring constant. Skate is desirable to an extent, as it provides the user with direct visual feedback that the probe has made contact with the wafer. However, too much becomes problematic as it results in a length of open-circuited CPW behind the probe tips, as shown in Fig. 4.1. At submillimeter-wave frequencies, the electrical length of this stub is non-negligible. For example, in CPW on a silicon substrate at 1 THz, a 1 μm length of transmission lines represents approximately 3° of electrical length. This stub length can reduce electrical performance of the probe itself and analysis has shown that variation in this length is the dominant source of unbiased on-wafer measurement error [20, 34].
2. On-wafer contact pad metallization: While the 5 μm silicon was able to make low-resistance contacts to gold contact pads, other metals such as aluminum, copper, and aluminum-copper alloys are being used as contact pad materials increasingly at higher frequencies [35–37]. Unlike gold, these other metals have native oxides which can be very hard. For example, aluminum oxide is widely used industrially as an abrasive due to its hardness, 9 on Mohs scale (from 1 to 10). As a result, it has been found that a minimum contact

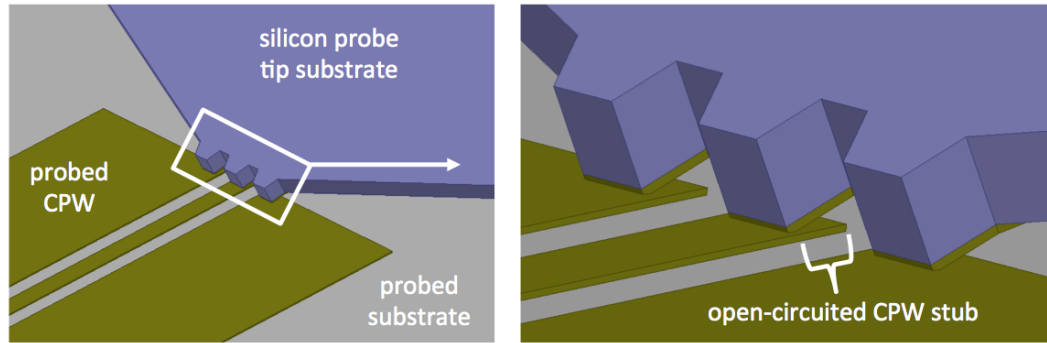


Figure 4.1: Micromachined probe tip landed on CPW transmission line, illustrating the CPW stub behind the contact point.

force of approximately 25 mN is required for micromachined probes to make a low-resistance contact (less than 1Ω) to aluminum pads, as described in Chapter 2.

3. Scratch marks: Traditionally, on-wafer probes make scratch marks on the contact pads of the DUT, providing visual confirmation of contact, as well as feedback regarding planarization of the probe tips. Typical scratch marks made by micromachined probes utilizing $15 \mu\text{m}$ thick silicon substrates are shown in Fig. 4.2. Due to the low contact force and large deflection of the $5 \mu\text{m}$ Si tips, scratch marks are usually not seen, eliminating this as a diagnostic or indicator of electrical contact.
4. Machining: The clamping regions become increasingly difficult to machine for thinner substrates, as the actual depth is approaching the tolerance limit for state-of-the-art CNC milling machines. For example, the smallest tolerance that can be achieved is approximately $\pm 2.5 \mu\text{m}$, resulting in a clamping region depth specification of approximately $7.5 \pm 2.5 \mu\text{m}$ for the WR-1.2 probes. Assembly is also more difficult, as the thinner chips do not tend to “drop in” place because the clamp regions are so shallow.

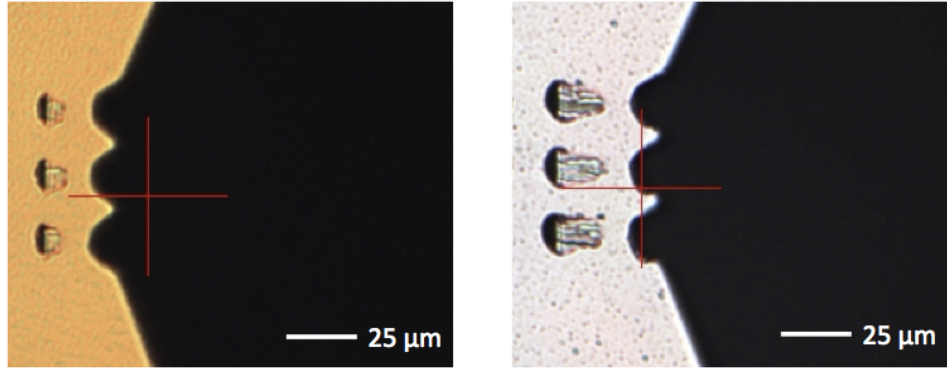


Figure 4.2: Typical scratch marks left on gold (left) and aluminum (right) films by $15\ \mu\text{m}$ thick silicon micromachined probes tips.

5. Design sensitivity: The probe is fabricated on a silicon-on-insulator substrate where the tolerance on the thickness of the device layer silicon is $\pm 0.5\ \mu\text{m}$ for both $5\ \mu\text{m}$ and $15\ \mu\text{m}$ device layer thicknesses. As a result, the RF performance of a design on $15\ \mu\text{m}$ silicon is less sensitive to this tolerance, an increasing concern at higher frequencies.

For these reasons, it is preferable to implement the WR-1.0 probe design on a $15\ \mu\text{m}$ silicon substrate. To determine if this is possible, we start with the design considerations of the RF channel.

4.2 RF Channel Design

In implementing the WR-1.0 probe design, sensitivity of RF performance due to machining tolerances is a primary concern. To address this, two designs are implemented: one utilizing a coaxial transmission line and a second using a microstrip transmission line. While the coaxial line exhibits lower attenuation, the microstrip line is expected to be less sensitive to variations in machining because the fields are largely confined within the substrate. To accommodate both designs, the RF

channel is designed such that the first higher-order (non-TEM) mode is suppressed in both types of structures.

Fig. 4.3(i) shows the first high-order mode patterns in both the microstrip and coaxial channels. Note that for the microstrip channel, the ground plane confines the fields to the lower half of the channel and the higher order mode is therefore not sensitive to the depth of the upper half of the channel, c . The cutoff frequency, f_c , for the TM_{10}^y mode may be calculated using the method of transverse resonance by solving the transcendental equation [38]:

$$\begin{aligned} \varepsilon_r \sqrt{\omega_c^2 \mu_0 \varepsilon_0 - \left(\frac{\pi}{a}\right)^2} \tan \left[(b-h) \sqrt{\omega_c^2 \mu_0 \varepsilon_0 - \left(\frac{\pi}{a}\right)^2} \right] = \\ - \sqrt{\omega_c^2 \mu_0 \varepsilon_r \varepsilon_0 - \left(\frac{\pi}{a}\right)^2} \tan \left[h \sqrt{\omega_c^2 \mu_0 \varepsilon_r \varepsilon_0 - \left(\frac{\pi}{a}\right)^2} \right] \end{aligned} \quad (4.1)$$

where ε_r is the relative dielectric constant of the substrate, $\omega_c = 2\pi f_c$ is the angular frequency, a is the channel width, b is the lower channel depth, and h is the substrate thickness. For the coaxial channel, application of the transverse resonance method for the TE_{01}^y mode yields the transcendental equation [38]:

$$\begin{aligned} \sqrt{\varepsilon_r} \tan [k_c (b-h)] + \tan (\sqrt{\varepsilon_r} k_c h) + \sqrt{\varepsilon_r} \tan (k_c c) = \\ \varepsilon_r \tan (k_c c) \tan (\sqrt{\varepsilon_r} k_c h) \tan (k_c (b-h)) \end{aligned} \quad (4.2)$$

where the cutoff wavenumber $k_c = \sqrt{\varepsilon_0 \mu_0} 2\pi f_c$, and c is the upper channel height.

Note that while the WR-1.2 machining constraints limited the RF channel width to 80 μm , improvements in machining capabilities permit smaller channels for the WR-1.0 design. On the other hand, a larger channel width would still be preferred, if possible, to ease machining and reduce fragility of the probe chips that must fit

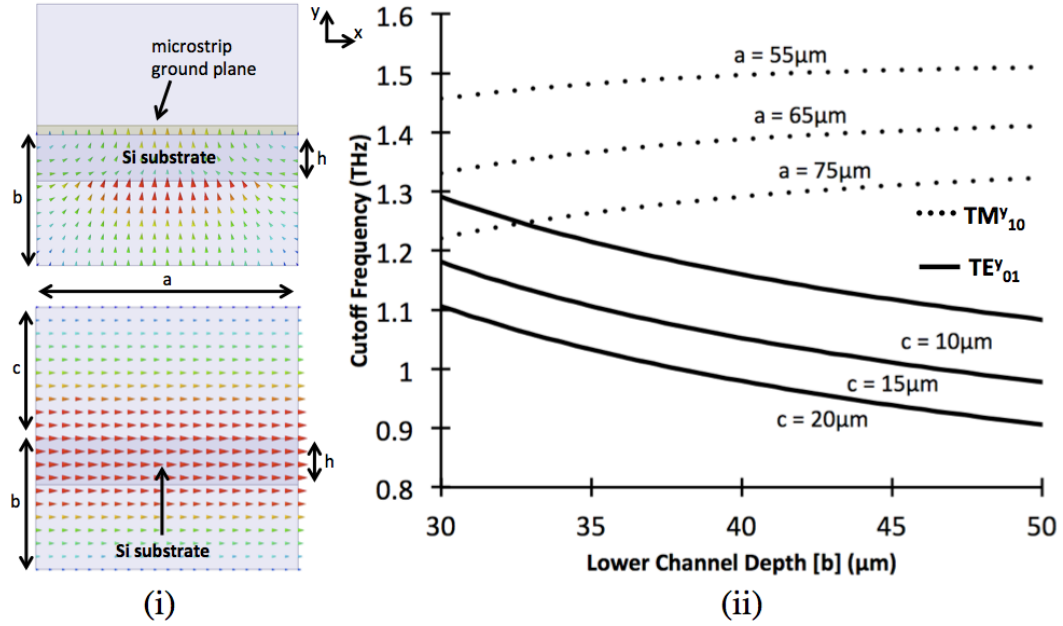


Figure 4.3: (i): Section view of electric field patterns for higher-order modes in RF channel: TM_{10}^y mode in microstrip channel (above), TE_{01}^y mode in coaxial channel (below), (ii): cutoff frequency for each of the two modes as a function of the channel geometry.

between the side walls of the channel. In addition, to prevent electrical shorting, the upper and lower channel depths must be large enough to ensure that, under worse case tolerances, there is sufficient clearance between the coaxial or microstrip signal conductors and the top or bottom walls of the RF channel. To accommodate the $\pm 2.5 \mu\text{m}$ machining tolerances, the channel dimensions should set the nominal cutoff frequencies of the high-order modes are approximately 1.2 THz or higher.

To choose the dimensions for the RF channel, Eqs. 4.1 and 4.2 are used to generate plots of the cutoff frequencies for the microstrip TM_{10}^y and coaxial TE_{01}^y modes. The results are shown in Fig. 4.3(ii) and illustrate a competing effect with respect to the lower channel: reducing the depth increases the cutoff frequency of the coaxial TE_{01}^y mode, but decreases the cutoff frequency of the microstrip TM_{10}^y mode. By choosing a channel width (a) of $75 \mu\text{m}$, a lower channel depth (b) of

30 μm , and an upper channel depth (c) of 15 μm , all mechanical requirements are satisfied, and the resulting cutoff frequencies are $f_{c,TE_{01}^y} = 1181$ GHz and $f_{c,TM_{10}^y} = 1221$ GHz.

To confirm this analysis, the cutoff frequencies for the microstrip TM_{10}^y and coaxial TE_{01}^y modes are determined through finite element simulation for the chosen geometry. The results agree quite well, with simulation indicating $f_{c,TE_{01}^y} = 1181$ GHz and $f_{c,TM_{10}^y} = 1222$ GHz, as shown in Fig. 4.4. In reality, the channel structures include the signal conductors, as well as air gaps between the silicon and channel walls, which perturb the TE_{01}^y and TM_{10}^y modes. By including these details in the simulations, as illustrated in Fig. 4.4, we see that these modes are further suppressed, increasing f_{c,TE_{01}^y} to 1388 GHz and f_{c,TM_{10}^y} to 1278 GHz.

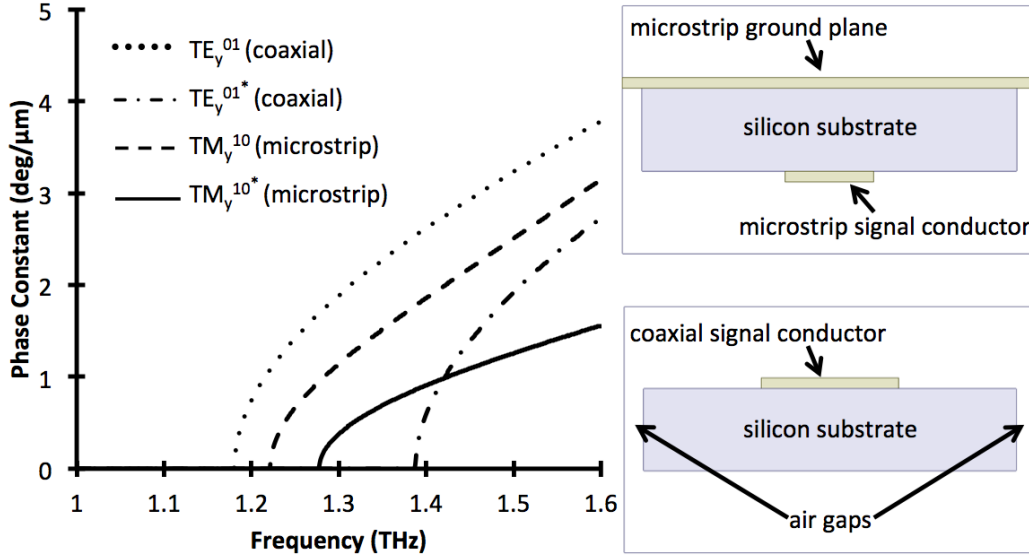


Figure 4.4: Plot of the phase constant from finite element simulation for the first waveguide modes in the coaxial and microstrip channels. The asterisk denotes inclusion of the signal conductors and air gap between the silicon substrate and channel walls, as shown at right.

4.3 Bias Filter Design

Having chosen the dimensions of the RF channel, we now consider the DC bias tee filter. As described in Chapter 3, the ground plane of the microstrip filter in the WR-1.2 probe design is floating, which caused a resonance just above the operating frequency. To prevent this phenomena in the WR-1.0 probe design, the bias filter should be designed without an on-chip ground plane. The most straightforward design change would be to simply remove the ground plane, which would result in a rectangular coaxial stepped impedance filter where the bias channel walls form the ground. This structure was initially chosen for the WR-1.0 probe and the design is shown in Fig. 4.5.

As performance sensitivity is a general concern for the WR-1.0 probe design, we investigate the effect of the substrate position in the bias channel. To allow for the machining tolerance of $\pm 2.5 \mu\text{m}$ on the width of the bias channel, a $5 \mu\text{m}$ nominal air gap is included on either side of the substrate. As a result, the chip can move laterally $\pm 5 \mu\text{m}$ in bias channel in the nominal case. To view the effect of this movement on the filter performance, we compare the simulation results of the filter with and without a $5 \mu\text{m}$ lateral offset. As shown in Fig. 4.6a, this type of filter is unacceptably sensitive to lateral position offsets, where a $5 \mu\text{m}$ offset causes loss of

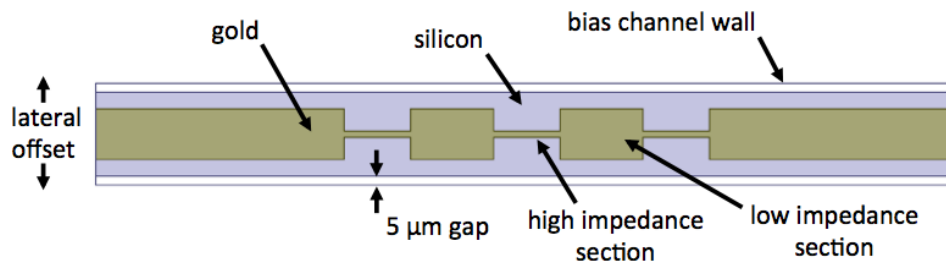


Figure 4.5: Coaxial stepped impedance filter structure. The potential lateral offset of the probe chip due to the air gap is nominally $5 \mu\text{m}$.

isolation in the upper half of the WR-1.0 band. This sensitivity is attributed to the fact that the stepped impedance filter response depends strongly on the electrical length and characteristic impedance of each section, both of which change as the substrate moves in the bias channel. It is suspected that, as the chip moves laterally, the dominant change is an increase the distributed capacitance, especially for the low impedance sections (due to the proximity of the conductor to the channel walls, which serve as the RF ground). Finite element simulation supports this hypothesis, indicating a decrease in both wavelength and characteristic impedance of the coaxial mode with a $5\ \mu\text{m}$ lateral offset as shown in Fig. 4.6b. To overcome this sensitivity, a different type of filter structure is required.

The hammerhead filter [39] is well-known for its ability to produce high levels of isolation over broad bandwidths while occupying a relatively small area [40]. However, due to the lack of an equivalent circuit model or other analytical design

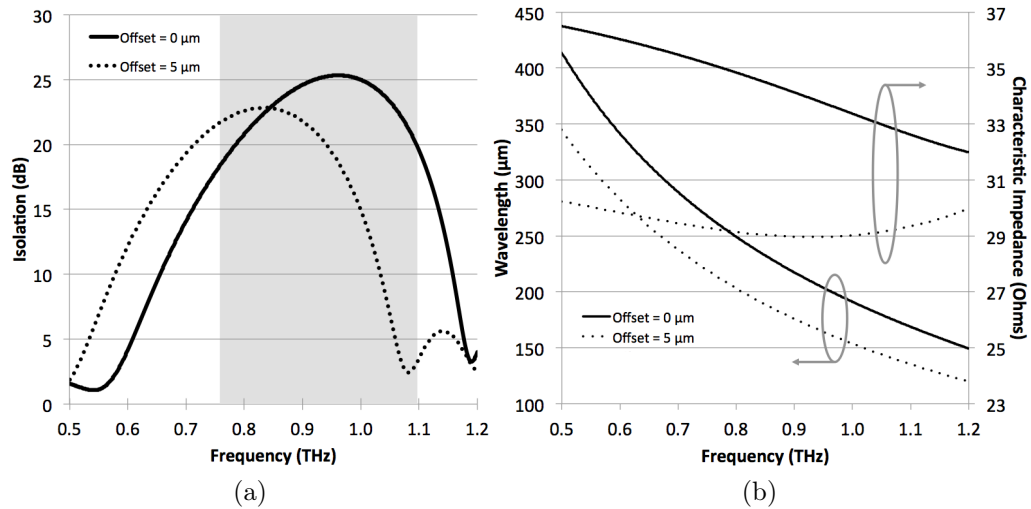


Figure 4.6: Stepped impedance coaxial filter simulations: (a) Shift in frequency response of isolation due to lateral offset (shaded area indicates WR-1.0 frequency band), (b) Reduction in coaxial mode wavelength and characteristic impedance of the low impedance section due to lateral offset.

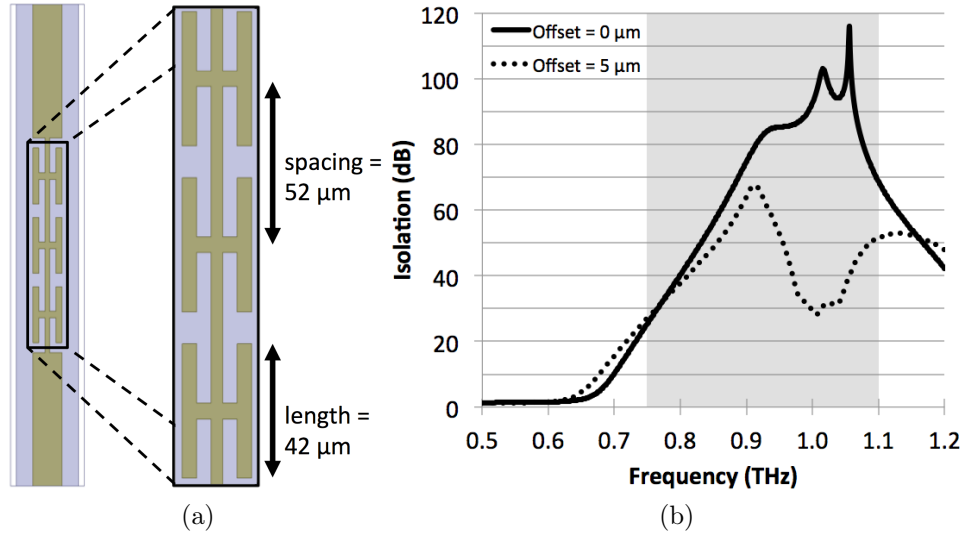


Figure 4.7: Hammerhead filter design: (a) layout of hammerhead structure, (b) sensitivity of isolation to lateral offset (shaded area indicates WR-1.0 frequency band).

tools, its use has not been widespread [41]. To investigate its application for the WR-1.0 probe, a design is implemented through finite element simulation and the simulation model is shown in Fig. 4.7a. To minimize any possible effects due to lateral offsets, the structure is kept as narrow as possible. For this work, due to the relatively large size of the probe chips, the minimum line and gap widths for fabrication are set to $5 \mu\text{m}$. After optimization, the head length and spacing, indicated in Fig. 4.7a, are $42 \mu\text{m}$ and $52 \mu\text{m}$, respectively. The simulated isolation, shown in Fig. 4.7b, is greater than 30 dB across the full WR-1.0 band.

To compare the offset sensitivity of the hammerhead filter to the coaxial filter, the simulation is repeated with a $5 \mu\text{m}$ lateral offset and the result is shown Fig. 4.7b. Despite a significant decrease in isolation at 1.0 THz, the isolation nevertheless remains greater than 29 dB across the WR-1.0 band. In addition, the filter response has not shifted in center frequency as with the coaxial filter. Lastly, it is interesting to note that the minimum isolation of the hammerhead filter with a $5 \mu\text{m}$ lateral

offset is greater than the maximum isolation of the coaxial filter with no offset. Because the hammerhead structure provides high isolation over the full waveguide band, is relatively insensitive to lateral offsets, and does not require an on-chip ground plane, it is chosen for the WR-1.0 probe bias filter.

4.4 Waveguide to Coaxial Transition

With the filter design complete, we now consider the waveguide to coaxial transition, depicted in Fig. 4.8. The transition is optimized through finite element simulation and the optimized dimensions are listed in Table 4.1, with the corresponding S-parameters shown in Fig. 4.9a. Given the increased concern over the effect of machining tolerances on RF performance, it is desired to improve the return loss, which is less than 15 dB at the WR-1.0 band edges.

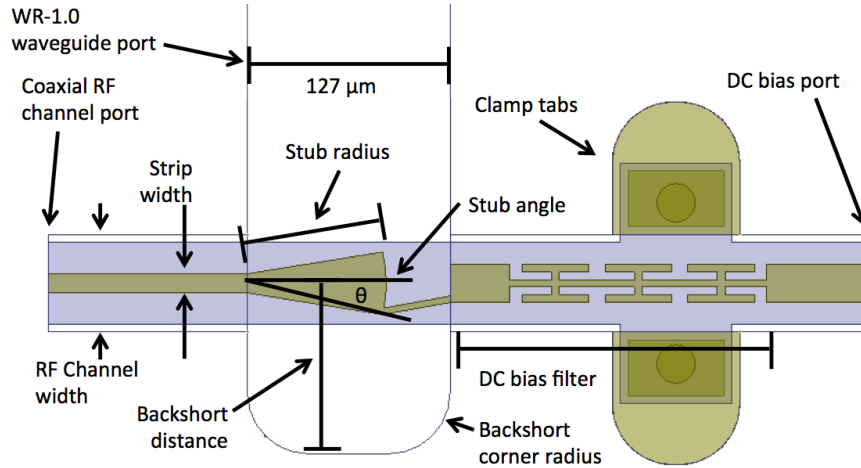


Figure 4.8: Parameters of HFSS simulation model for waveguide to coaxial transition.

Table 4.1: Dimensions of the waveguide to coaxial transition

RF channel width	61 μm	Backshort fillets	38 μm
Strip width	12 μm	Backshort distance	107 μm
Stub radius	87 μm	Stub angle	13°

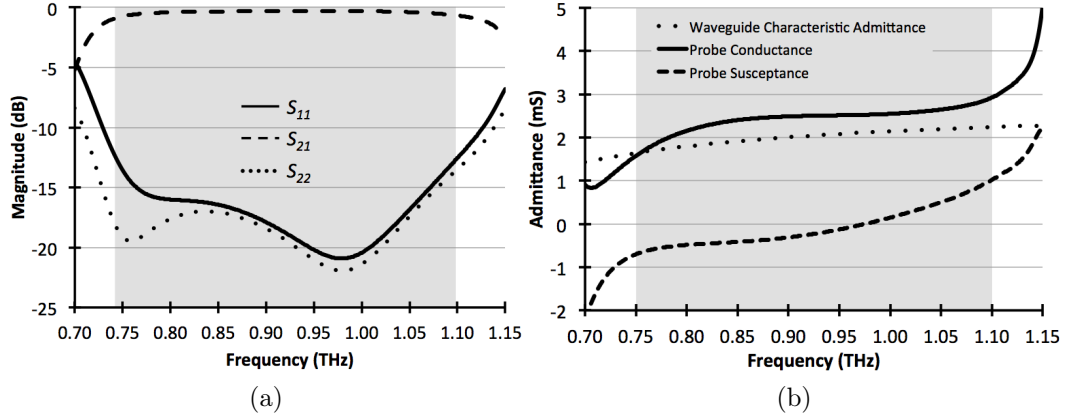


Figure 4.9: Finite element simulations of initial waveguide to coaxial transition design. The shaded area indicates the WR-1.0 band. (a): simulated S-parameters of the WR-1.0 waveguide to coaxial transition, (b): waveguide input admittance at the transition.

To examine the nature of the limited return loss, we consider the input admittance looking into the waveguide port, $Y_{in,wg}$ by transforming the waveguide reflection coefficient, S_{11} , using the well-known relation:

$$Y_{in,wg} = Y_{0,wg} \frac{(1 - S_{11})}{(1 + S_{11})}$$

where $Y_{0,wg}$ is the characteristic admittance of the waveguide and S_{11} has been de-embedded to the probe. By taking the real and imaginary parts, we find the input conductance and input susceptance, which are shown in Fig. 4.9b. The admittance shows an interesting characteristic: while the input conductance of the probe is relatively closely matched to the characteristic admittance of the waveguide, there is roughly ± 1 milliSiemens (mS) of susceptance at the band edges. If we can tune out this susceptance, it should improve the return loss of the waveguide transition.

4.4.1 Backshort Analysis

It is well understood that the waveguide backshort is a susceptive tuning element, and it is part of the waveguide transition. It was suggested that the residual susceptance shown in Fig. 4.9b was the result of an incorrect backshort length, and that with adjustment, it should be possible to tune it out. However, it was found that adjustment of the backshort length could only tune out the susceptance near one of the frequency band edges, but not both. To explore the limitations of the backshort as a susceptive tuning element, we first consider that the waveguide backshort is a shorted transmission line. Its input susceptance is well-known and can be expressed as:

$$B_{in,bs} = \text{Im} \left(\frac{1}{Z_{in,bs}} \right) = -Y_0 \cot(\theta_{bs}) \quad (4.3)$$

where θ_{bs} is the electrical length of the backshort. From this expression it is clear that, at a single frequency point, any susceptance value can be produced by choosing the appropriate electrical length. However, considering the equivalent circuit model shown in Fig. 4.10a, we must ensure the backshort does not short circuit the probe admittance at any frequency within the waveguide band. This restricts the available susceptance, requiring that the electrical length of the backshort is well within 0° and 180° at all frequencies within the waveguide band.

To determine the range of backshort susceptance, we plot Eq. 4.3 within the length bounds established above. The electrical length of a transmission line is the change in phase that occurs in a traveling wave over the physical length of the line. For a wave traveling in the z -direction, the electrical length may be expressed as $\theta = \beta_z l$, where β_z is the propagation constant and l is the length of the line. In rectangular waveguide, the propagation constant of the TE_{10}^z dominant mode is

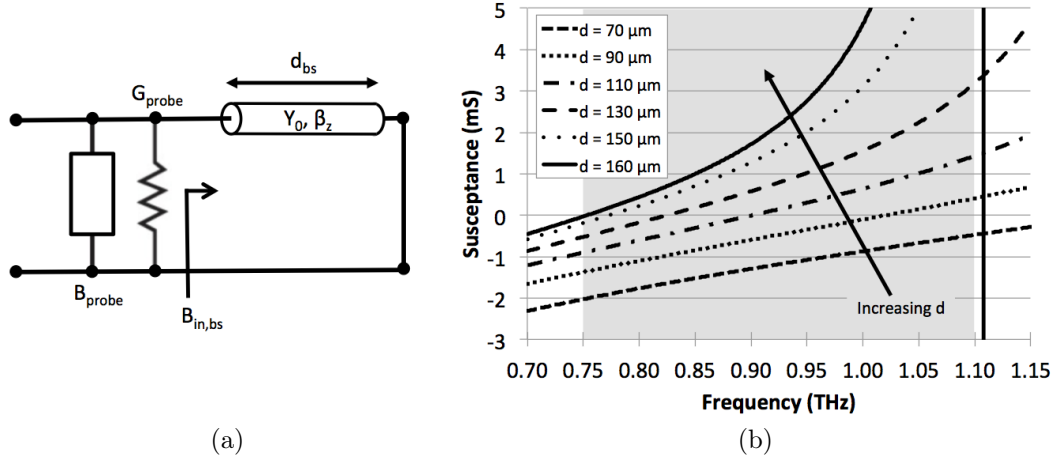


Figure 4.10: Waveguide backshort susceptance. (a): Equivalent circuit model of the waveguide transition. The backshort is in parallel with the probe. (b): Effect of distance on backshort susceptance.

well-known to be:

$$\beta_z = \sqrt{(2\pi f \sqrt{\mu_0 \epsilon_0})^2 - \left(\frac{\pi}{a}\right)^2} \quad (4.4)$$

where a is broad dimension of the waveguide and f is the frequency. For WR-1.0 waveguide, a is $254 \mu\text{m}$ (.0010 inch) and, at the maximum frequency of 1100 GHz, the propagation constant is $\beta_z = 1.12^\circ/\mu\text{m}$. Therefore, the backshort must be significantly less than $160 \mu\text{m}$ to be well-behaved near 1.1 THz.

Referring to Fig. 4.8, we see that the finite corner radius of the backshort sets a minimum machinable distance. To reduce the likelihood of end-mill breaking during machining, the channel depth should be approximately three times the corner radius or less, as a rule of thumb. As the probe housing is milled split along the E-plane of the waveguide, the milled waveguide channel depth is $127 \mu\text{m}$. Therefore, the backshort corner radius in the is set to $38 \mu\text{m}$ (.0015 inch), which results in a minimum machinable backshort length of approximately $70 \mu\text{m}$. It is important to note that the finite backshort corner radius does have an effect: as the backshort corner radius

increases, the backshort susceptance decreases. This can be understood intuitively through the capacitive effect of sharp corners: as the corner radius increases, the associated capacitance decreases, decreasing the susceptance. However, the finite corner radius simply reduces the effective length of the backshort, which does not affect this conceptual analysis and it is therefore neglected.

Within the above distance restrictions, we plot the backshort susceptance and the results are shown in Fig. 4.10b. Considering the frequency dependence of the transition and backshort susceptances, adjustment of the backshort distance can tune the susceptance at either end of the frequency band, but not both. In addition, it is interesting to note that the backshort cannot produce a purely capacitive susceptance (positive) over the entire rectangular waveguide band, though it is possible over smaller bandwidths. To improve the return loss of the transition, a different tuning structure is required.

4.4.2 Capacitive Step Analysis

In rectangular waveguide, a step in the height, as illustrated in Fig. 4.11a, has an equivalent circuit model of a shunt capacitor [42] and has been used to improve the bandwidth of waveguide transitions [28]. To evaluate its application as a susceptive tuning element, we consider the equivalent circuit model shown in Fig. 4.11b.

Because a shunt capacitor can only add positive susceptance, to provide a match the load susceptance must be negative and the load conductance should equal the characteristic admittance at the location of the step. To begin the design, we therefore consider the offset probe admittance, Y_{off} , as we move down the waveguide. The admittance at several distances is shown in Fig. 4.12, which indicates that an offset of approximately 40-60 μm produces a normalized input conductance,

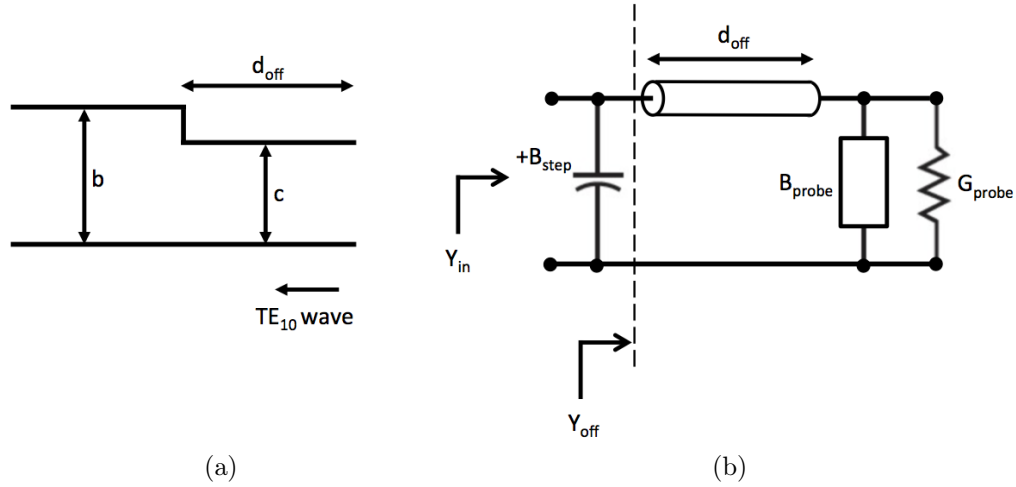


Figure 4.11: Waveguide capacitive step matching network. (a): The waveguide height increases from c to b . (b): Equivalent circuit model illustrating the capacitance associated with the change in height.

$y = \frac{G_{\text{off}}}{Y_0}$, near unity over most of the band. The susceptance at this offset is also purely inductive (negative), which can potentially be tuned out by the capacitive susceptance of the step.

The potential reduction of the load susceptance depends on its frequency dependence relative to the step susceptance. The susceptance associated with a step in waveguide height may be approximated by the expression [43]:

$$B_{\text{step}} = \frac{2a Y_0}{\lambda_g} \sum_{n=1}^{\infty} \frac{\sin^2(n\pi c/b)}{(n\pi c/b)^2 \sqrt{n^2 - (2b/\lambda_g)^2}} \quad (4.5)$$

where a is the waveguide width, λ_g is the guided wavelength, Y_0 is the waveguide characteristic admittance, c is the incident waveguide height, and b is the stepped waveguide height, as illustrated in Fig. 4.11a. The susceptance associated with several step heights is calculated according to Eq. 4.5 and is shown in Fig. 4.13a. To consider the effect of the step on the transition, we choose a step offset of $60 \mu\text{m}$ and plot the sum of the load and step susceptances, which is shown in Fig. 4.13b.

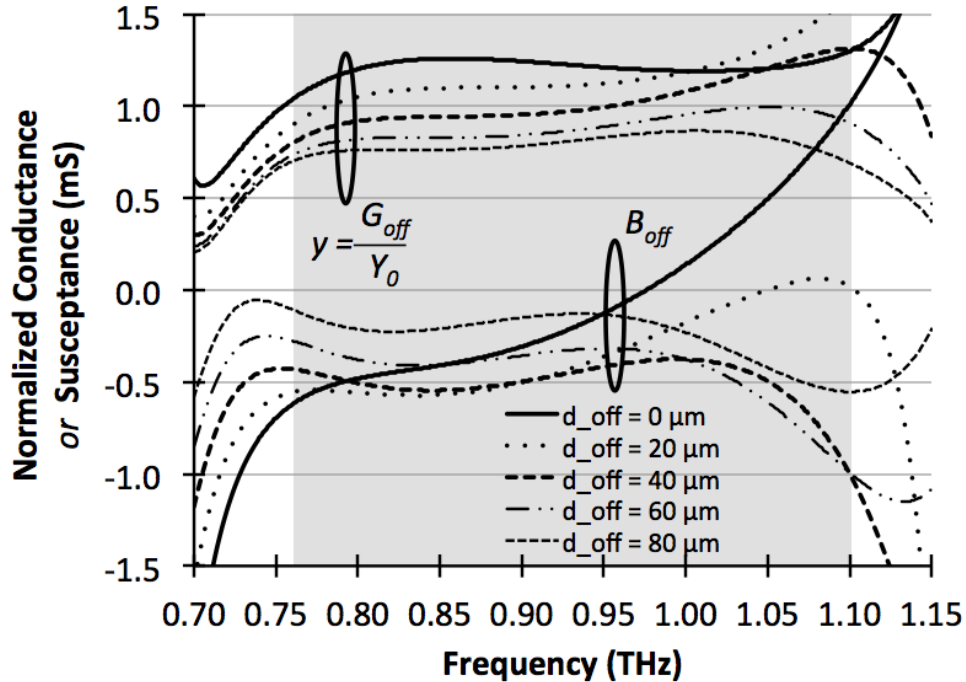


Figure 4.12: Effect of offset distance on offset admittance. The load conductance is normalized to the characteristic admittance of the waveguide.

The figure shows that a step height of approximately $30 \mu\text{m}$ should provide a total susceptance that is relatively close to zero across the band.

However, note that due to the finite corner radius required by the CNC end-milling of the waveguide channel, it is not possible to produce an abrupt step in the height of the waveguide as shown in Fig. 4.11a. To capture the effect of the corner radius, as well as to numerically optimize the true dimensions of the step, we include the machinable step geometry in the finite element simulation model, shown in Fig. 4.14, using the above results as a starting point for the optimization. The final dimensions of the optimized step are listed in Table 4.2 and the simulation results are shown in Fig. 4.15. The return loss of the transition is dramatically improved to greater than 20 dB across the full band, and the bias port isolation is greater than 50 dB. As shown in Fig. 4.15b, the capacitive step does, in fact, greatly reduce the

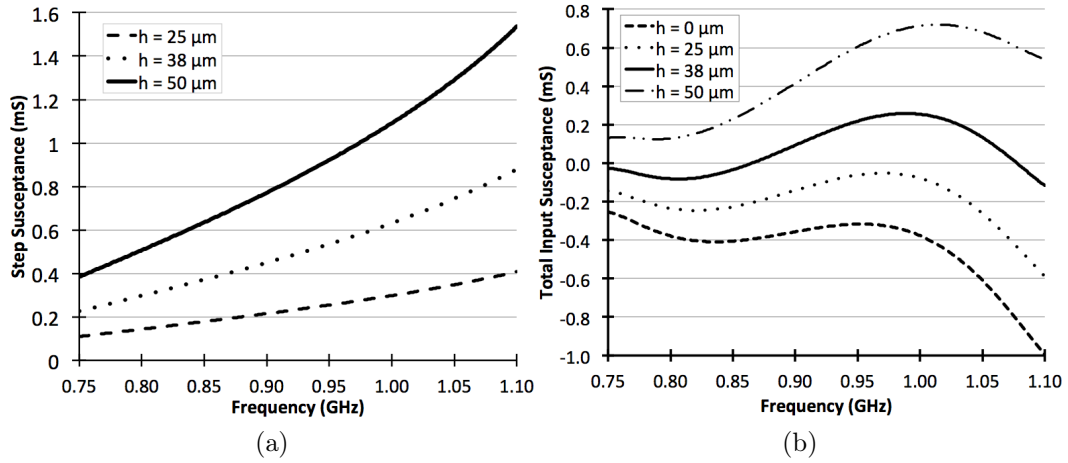


Figure 4.13: Capacitive step modeling. (a): Susceptance due to several step heights. (b): Resulting total probe input susceptance due to several step heights.

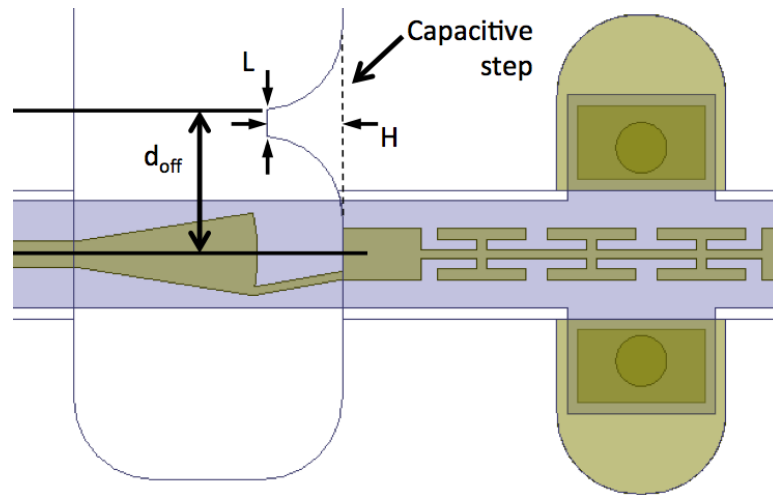


Figure 4.14: HFSS finite element simulation model of waveguide to coaxial transition including capacitive step.

Table 4.2: Optimized dimensions of capacitive step

Step length, L	Step height, H	Step offset, d_{off}
$13 \mu\text{m}$	$36 \mu\text{m}$	$69 \mu\text{m}$

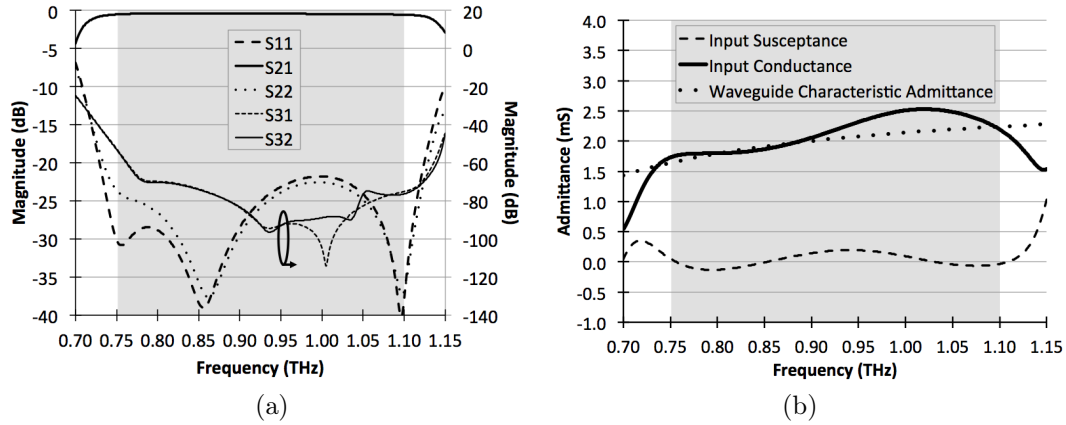


Figure 4.15: Final simulation of waveguide to coaxial transition including capacitive step. (a): Simulated S-parameters, port 1 is the WR-1.0 waveguide, port 2 is the coaxial port, and port 3 is the bias filter port. (b): Waveguide input admittance at the end of the coaxial step.

input susceptance to less than ± 0.2 mS across the full WR-1.0 waveguide band.

4.5 Coaxial to CPW Transition

To enable contact with the ground-signal-ground (GSG) contact pads used by many on-wafer devices, the rectangular coaxial mode must be converted into the coplanar waveguide mode (CPW). This coaxial to CPW transition of the probe chip is designed through finite element simulation. To provide a starting point for the optimization, we consider we consider the CPW geometry shown in Fig. 4.16a.

To reduce radiation and excitation of high-order modes, the ground-to-ground spacing of the CPW should be minimized. However, the probe pitch (center-to-center spacing between a ground-signal pair of the contact tips) affects the CPW ground-to-ground spacing, and it can not be made arbitrarily small. Referring back to Fig. 4.1, the ground-signal-ground contacts are supported by the silicon substrate, and the silicon is etched so that the individual contacts can be distinguished

when viewed from above. The silicon etch is performed as a backside processing step, and the resulting alignment with respect to the frontside gold (CPW conductors) is typically better than $\pm 5 \mu\text{m}$. To ensure segmentation and visibility of the tips and that ground-signal-ground conductors remain partially supported under backside misalignment, the minimum probe pitch is $25 \mu\text{m}$. The pitch requirement constrains the CPW geometry such that:

$$S + W = 25 \mu\text{m} \quad (4.6)$$

The characteristic impedance, Z_0 , of the CPW can be calculated according to [44]:

$$Z_0 = \frac{1}{c_0 C_{air} \sqrt{\varepsilon_{eff}}} = \frac{30\pi}{\sqrt{\varepsilon_{eff}}} \frac{K(k'_0)}{K(k_0)} \Omega \quad (4.7)$$

where the effective dielectric constant is:

$$\varepsilon_{eff} = 1 + q \frac{(\varepsilon_r - 1)}{2} \quad (4.8)$$

The dielectric constant of the silicon substrate is $\varepsilon_r = 11.8$, and q is the filling factor:

$$q = \frac{K(k_1)}{K(k'_1)} \frac{K(k'_0)}{K(k_0)} \quad (4.9)$$

where $K(k)$ is the complete elliptic integral of the first kind, and the elliptic moduli are defined by the CPW and substrate geometry:

$$k_1 = \frac{\sinh\left(\frac{\pi S}{4h}\right)}{\sinh\left(\frac{\pi(S+2W)}{4h}\right)}$$

$$k_0 = \frac{S}{S + 2W}$$

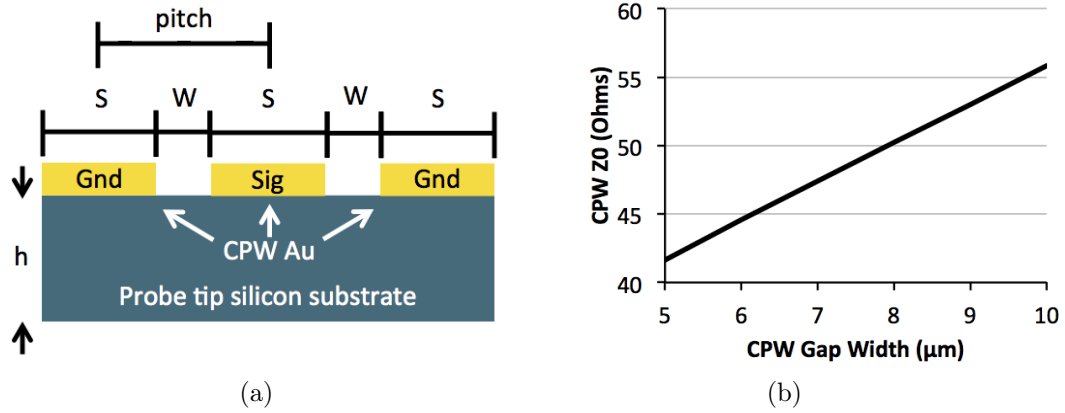


Figure 4.16: Probe tip CPW characteristic impedance. (a): CPW geometry illustrating signal and gap widths. (b): Calculated characteristic impedance for fixed 25 μm pitch.

$$k'_i = \sqrt{1 - k_i^2}$$

We plot the characteristic impedance of the CPW subject to the constraint of Eq. 4.6 above and the result is shown in Fig. 4.16b. This calculation shows that to produce 50 Ω in a 25 μm pitch format, a gap width of approximately 8 μm is required, resulting in a signal conductor width of 17 μm . These dimensions are used as a starting point in the simulation model, which is shown in Fig. 4.17a. In the simulation, all conductors are assumed gold and have been assigned a conductivity of 3.2×10^7 Siemens/meter. After optimization, the tip CPW dimensions are unchanged and the simulated S-parameters are shown in Fig. 4.17b, indicating an insertion loss between 1.7 and 2.6 dB and return loss greater than 18 dB across the band for the rectangular coaxial to CPW transition.

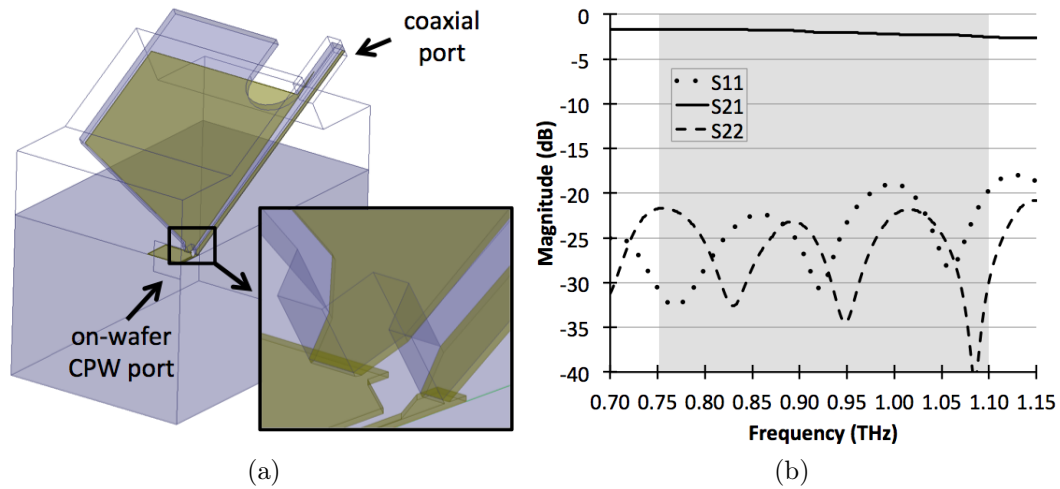


Figure 4.17: HFSS finite element simulation of coaxial to on-wafer CPW. (a): HFSS simulation model. (b) Simulated S-parameters, port 1 is the coaxial port, port 2 is the on-wafer CPW port.

4.6 Full Simulation

As described in the WR-1.2 work, a third simulation of a 30 degree H-plane junction is performed to capture the loss of the 20 mm waveguide channel and mismatch of the waveguide interface. By combining this simulation with the waveguide to coaxial and coaxial to CPW transitions, the full simulated S-Parameters of the probe are obtained and shown in Fig. 4.18a. The simulated insertion loss is less than 5.9 dB and return loss is greater than 17 dB across the full waveguide band. Not shown is the bias port isolation, which is simulated to be greater than 40 dB across the band.

The microstrip design process utilizes a similar approach and the final simulated performance of the microstrip design is shown in Fig. 4.18b. As expected, the predicted insertion loss is higher: 9.3 dB maximum at 1.1 THz. The microstrip design detail is provided in Appendix C.

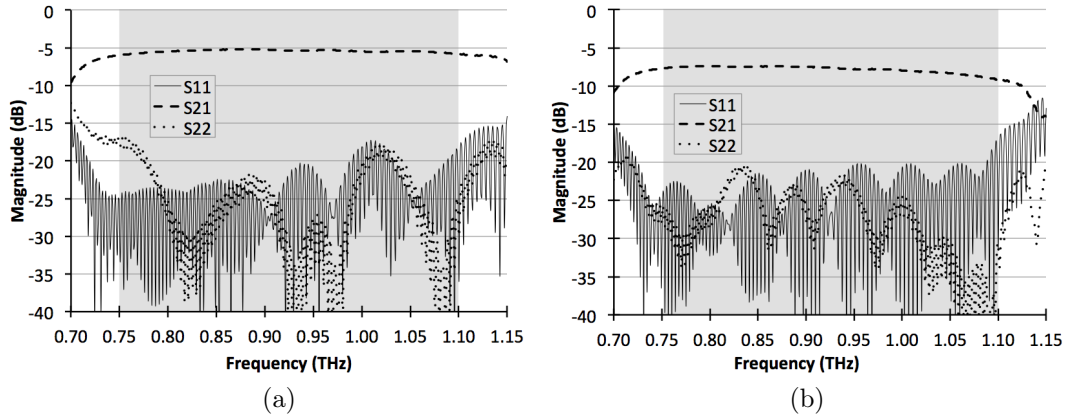


Figure 4.18: Predicted S-parameters of the full probe structure from the HFSS simulation models, (a): coaxial, (b): microstrip. Port 1 is at the WR-1.0 waveguide input, port 2 the on-wafer CPW, offset from from the contact pads by $40 \mu\text{m}$.

4.7 RF Characterization

The RF characterization experimental setup and procedure is identical to that described for the WR-1.2 probe work. However, the CPW calibration standards are revised and the details are summarized in Table 4.3. After performing the two-tier calibration process, S-parameters of the coaxial probe design are de-embedded and are shown in Fig. 4.19a. The measured insertion loss is less than 7 dB across most of the band, which agrees well with simulation. The measured return loss is less than simulation, but this is not unexpected due to uncertainties associated with the tolerances in machining of the waveguide housing, mounting of the probe chip into the waveguide housing, and alignment of the waveguide interfaces. Table 4.4 summarizes the simulated sources of loss and compares the total against measurement.

Table 4.3: WR-1.0 CPW calibration kit

Contact pad width	$13 \mu\text{m}$	CPW center conductor width	$4.2 \mu\text{m}$
Contact pad gap	$11 \mu\text{m}$	CPW center conductor gap	$4.0 \mu\text{m}$
Contact pad length	$5 \mu\text{m}$	CPW center ground width	$60 \mu\text{m}$
Taper length	$8.5 \mu\text{m}$	Delay short increment	$13.5 \mu\text{m}$

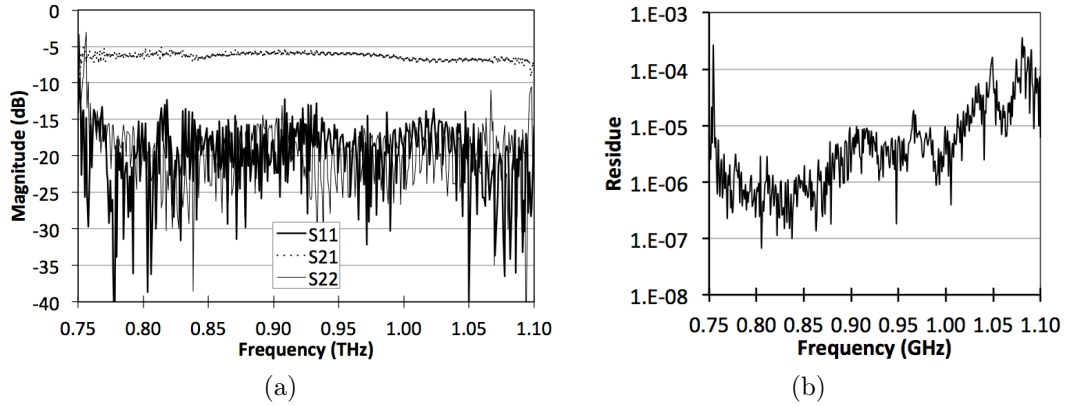


Figure 4.19: Second-tier on-wafer calibration. (a): De-embedded probe s-parameters, (b): Residue of the least-squares fit.

Table 4.4: Probe loss contributions at 925 GHz

WR-1.0 waveguide channel (20 mm length)	2.8 dB
Waveguide to coaxial transition	0.5 dB
Coaxial to on-wafer CPW transition	2.0 dB
Total simulated loss	5.3 dB
Total measured loss	5.8 dB

To verify the accuracy and repeatability of the on-wafer calibration, we remeasure the on-wafer CPW delay shorts after applying the calibration coefficients from the on-wafer calibration, and compare against the ideal response generated from finite element simulation. It should be noted that only three calibration standards are required for a fully determined system in a one-port calibration. Provided that the standards are sufficiently different (so they do not overlap at any frequency) and the measurement system is repeatable, remeasurement of the standards will simply return the ideal definitions of the standards, even if those definitions are incorrect. However, it should be noted that for the present case, all five delayed shorts are used to determine the three unknown error coefficients, and the set of calibration measurements yields an overdetermined system, with the error terms determined through a least-squares fit. As a result, it is not possible to fit the error coefficients

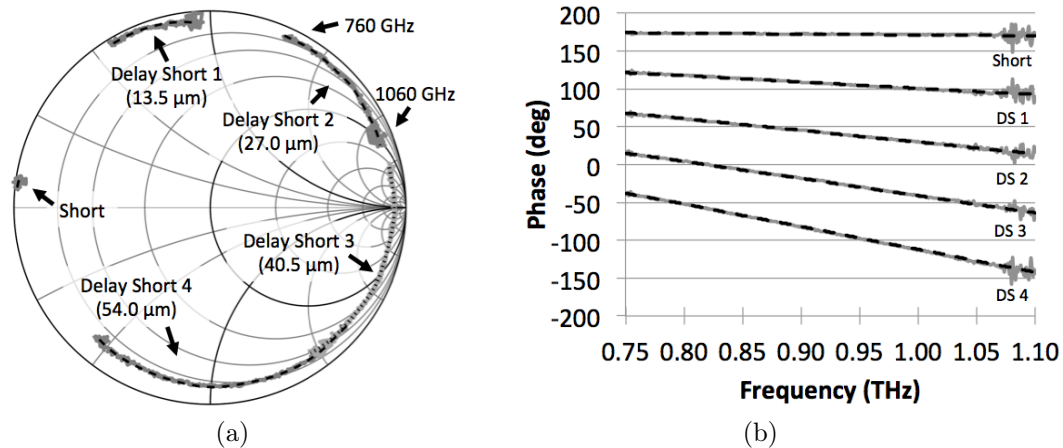


Figure 4.20: Error-corrected measurements of CPW delay shorts shown in magnitude (a) and phase (b). The dark dashed lines indicate the ideal response.

to arbitrarily-defined standards and the least-squares residual error is a measure of the accuracy with which the standards fit their corresponding models. The residual is shown in Fig. 4.19b, which shows a residue less than 10^{-5} over most of band and remeasurement of the standards is shown in Fig. 4.20.

Given the successful performance of the coaxial design, it was decided not to expend effort characterizing the microstrip design, which is expected to exhibit significantly higher insertion loss.

4.8 Diode Characterization

To demonstrate the utility of the WR-1.0 probe for on-wafer measurements, it is used to characterize an on-wafer GaAs Schottky diode for the first time at 1 THz. Shown in Fig. 4.21a is a GaAs Schottky diode terahertz phase shifter designed and fabricated by Naser Alijabbari [25]. The diode is integrated on a CPW transmission line with a shunt CPW open stub tuning element designed to maximize the available phase shift at 1 THz. Fig. 4.21b shows calibrated measurements of the diode

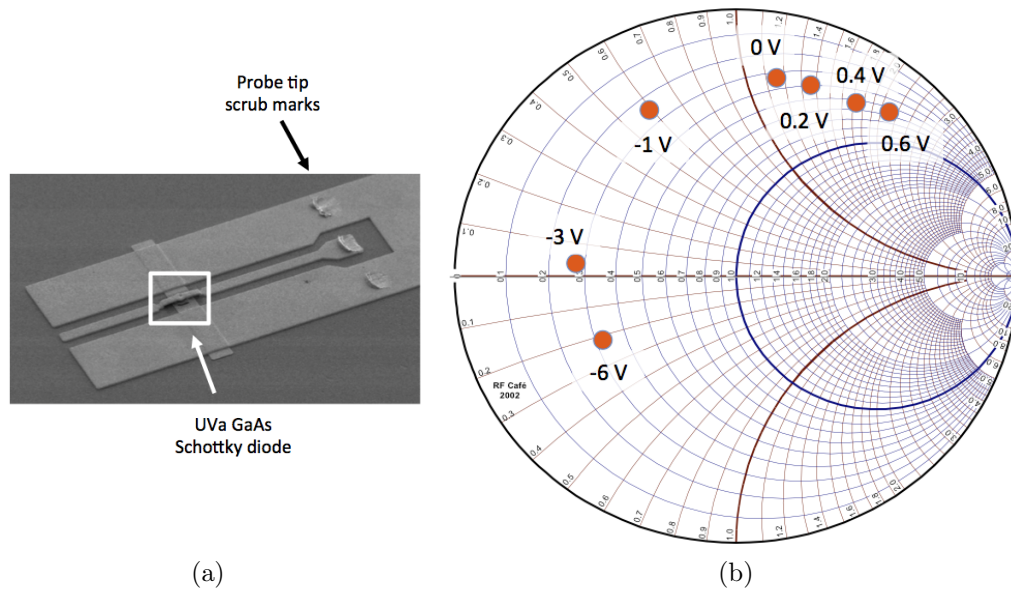


Figure 4.21: UVa GaAs Schottky diode THz phase shifter. (a) SEM image of CPW transmission line with integrated diode for on-wafer characterization (image courtesy of N. Alijabbari). (b) Calibrated on-wafer reflection coefficient of diode at 1.0 THz.

reflection coefficient, indicating a phase shift of nearly 180° as the diode bias is varied from -6 V to +0.6 V. This data is being used to develop measurement-based high frequency models of the diodes which will permit accurate design of more complex circuits such as multipliers and mixers.

4.9 Full Two-Port Calibration

Finally, we demonstrate the WR-1.0 probes in a full two-port on-wafer measurement system, as this measurement configuration is most useful. For example, two-port measurements are necessary for characterization of three-terminal devices such as transistors and for measurement of circuits with an input and output, such as amplifiers or filters. Therefore, it is important to establish two-port measurement capabilities.

At submillimeter-wave frequencies, multiline TRL (Thru-Reflect-Line) [45] is considered the most robust and reliable approach for two-port on-wafer calibrations. This is because it only requires uniform transmission lines, which are relatively easy to fabricate, and it is a “self-calibration” method, requiring minimal specifications from the user. Specifically, the physical lengths of the lines must be defined, an estimate of the phase velocity must be provided, and the phase of the reflect standard must be known to within $\pm 90^\circ$.

To maximize the overall dynamic range of the measurement, the probes are connected directly to the extenders using machined 90° waveguide polarization twists and the sample is lifted to the probe tips using a sample riser, as shown in Fig. 4.22. For this experiment, the structure of the calibration lines are the same as in the RF characterization of the probes, but instead, the CPW standards include a thru, short, $30\ \mu\text{m}$ thru line (80° long at 925 GHz), and a $45\ \mu\text{m}$ thru line (120° long at 925 GHz). After calibration, the error coefficients are applied and the thru and short are remeasured to determine the calibrated dynamic range of the system. As shown in Fig. 4.23, over much of the band there is 30 dB of dynamic range for

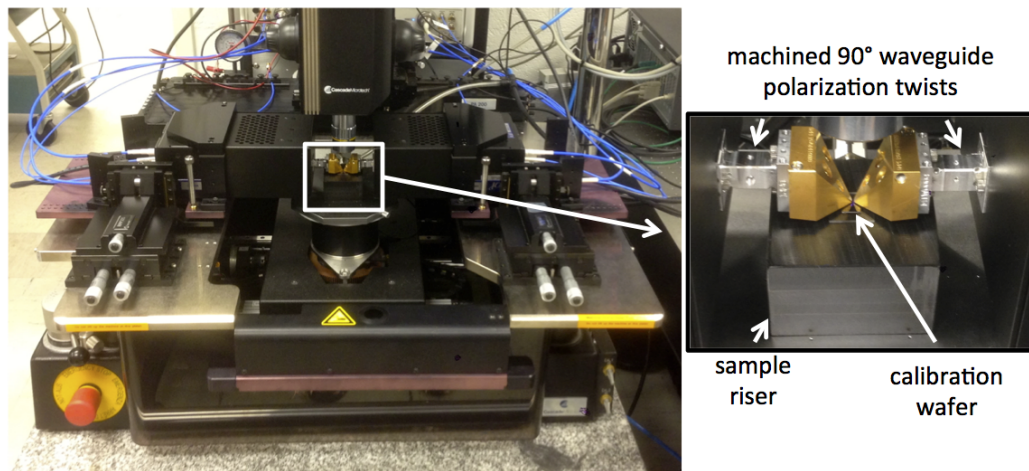


Figure 4.22: Full two-port on-wafer measurement setup on a commercial probe station using machined twists and a sample riser.

reflection, and 25 dB of dynamic range for transmission, which is comparable to a recent report of 30 dB in the 325 - 508 GHz range [46]. Remeasurement of the thru shows ± 0.1 dB transmission from approximately 760 to 1025 GHz, while the reflection from the short shows ± 0.5 dB peaks at 770 GHz, 830 GHz and 970 GHz, which are also visible in the isolation measurement (S_{21}). CPW is known to couple to substrate modes [47, 48], and because the calibration substrate is electrically thick (nearly three wavelengths thick at 925 GHz), it is suspected that these effects are due to coupling to substrate modes.

To investigate this hypothesis, we consider the section view of the CPW lines, shown in Fig. 4.24b. As shown in Fig. 4.24a, the silicon calibration wafer is mounted to a 850 μm thick borosilicate glass slide. In the region beneath the CPW metallization, this structure is a dielectric-coated conductor, and the dielectric boundary between the silicon and glass slide supports propagation of surface-guided waves. Because the slide is a thick, lossy dielectric (loss tangent, $\tan \delta = 0.05$ [49]), for the purposes of this analysis it is assumed to be infinitely thick. The propagation

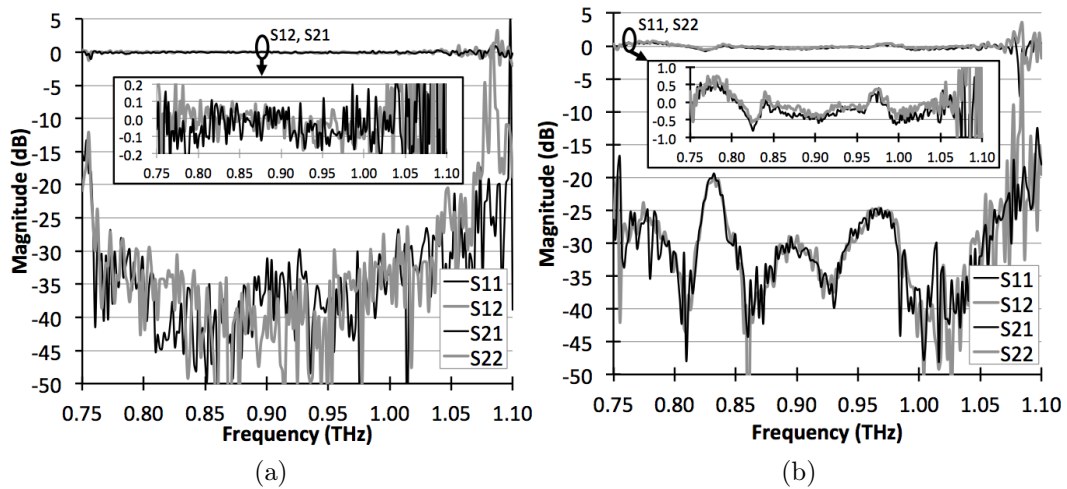


Figure 4.23: Calibrated dynamic range. (a): calibrated remeasurement of the thru, (b): calibrated remeasurement of the short.

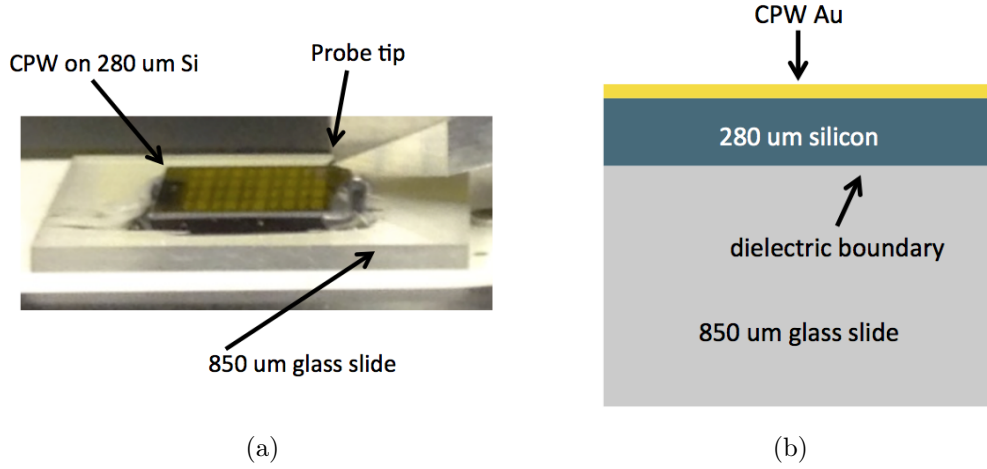


Figure 4.24: Analysis of surface waves in calibration substrate. (a): image of calibration substrate mounted to glass slide, (b): dielectric waveguide model based on calibration substrate.

constants for the TE_z and TM_z modes of such a structure may be expressed as [43]:

$$k_z = \sqrt{\omega^2 \varepsilon_d \mu_0 - k_{xd}^2} \quad (4.10)$$

where, for the TM^z modes, k_{xd} is the solution to the transcendental equation:

$$\frac{\varepsilon_1}{\varepsilon_2} k_{xd} t \tan(k_{xd} t) = \sqrt{(\omega t)^2 (\varepsilon_2 \mu_0 - \varepsilon_1 \mu_0) - (k_{xd} t)^2} \quad (4.11)$$

and for the TE^z modes, k_{xd} is the solution to:

$$-k_{xd} t \cot(k_{xd} t) = \sqrt{(\omega t)^2 (\varepsilon_2 \mu_0 - \varepsilon_1 \mu_0) - (k_{xd} t)^2} \quad (4.12)$$

where in all cases $\varepsilon_1 = 5.76$ is the permittivity of the borosilicate glass slide [49], $\varepsilon_2 = 11.8$ is the permittivity of the silicon, and $t = 280 \mu\text{m}$ is the thickness of the silicon.

We use Eqs. 4.10-4.12 to determine which modes have propagation constants

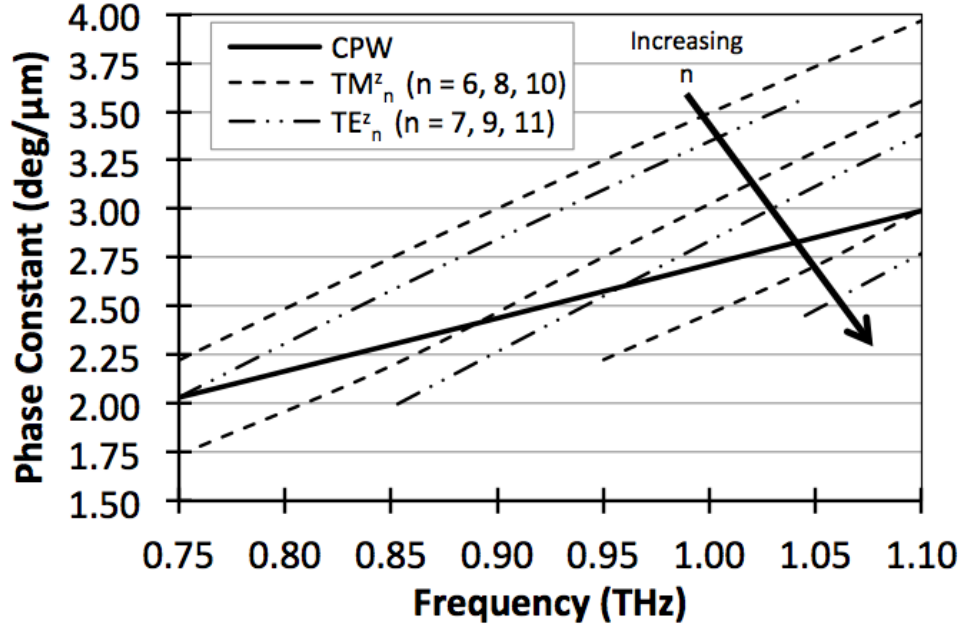


Figure 4.25: Propagation constants for substrate modes near the CPW mode.

that are in the vicinity of the CPW mode propagation constant and compare them in Fig. 4.25. The results show that at approximately 750, 870, 950 and 1100 GHz, the CPW propagation constant intersects the propagation constants of the TE_7^z , TM_8^z , TE_9^z , and TM_{10}^z modes, respectively. As a result, there is a potential for strong coupling between the CPW mode and substrate modes at these frequencies. While these frequencies are slightly different than those of the observed peaks, the close proximity and absence of other nearby modes strongly suggest that the transmission and reflection peaks shown in Fig. 4.23b are a result of substrate modes. In addition, this analysis is only an approximation, as the full width of the CPW and the glass thickness are both finite and mounting wax is used at the interface between the glass and silicon. Nevertheless, this simple analysis provides justification for exploring overall system performance on other calibration substrates. For example, the dynamic range characterization should be repeated using a single-mode propagation calibration substrate such as thin-film microstrip [50].

4.10 Conclusion

This work contributes the design of the first on-wafer probe for the WR-1.0 waveguide band (750 GHz - 1.1 THz). Through analysis of the RF channel allowed the design to be implemented on 15 μm Si, which provides a number of benefits over thinner substrates. In addition, an equivalent circuit model approach is used for the design and addition of a waveguide capacitive step, which dramatically improves the performance of the waveguide transition. The measured probe performance agrees well with simulation, yielding 7 dB of insertion loss, and approximately 15 dB of return loss over most of band. In a two-port configuration using a commercial probe station, the probes exhibit approximately 25-30 dB of calibrated dynamic range over most of the band, and spurious performance peaks were correlated with substrate modes. The result of this work has enabled for the first time on-wafer device measurements up to 1.1 THz, where at UVa, the probes are currently being used to validate circuit models of unique GaAs Schottky diodes structures to enable faster, more accurate development of complex diode-based circuits such as multipliers, mixers, and detectors. Elsewhere, the probes are being using to develop high frequency transistors for terahertz integrated circuits, which promise to open access to this largely untapped region of the electromagnetic spectrum.

Chapter 5

Conclusion

The terahertz frequency spectrum is a potential tool for many applications, and development of terahertz integrated circuits will enable access to this largely untapped region. However, until recently, the measurement infrastructure necessary for on-wafer characterization of devices and materials above 500 GHz was essentially non-existent. In 2010, the invention of the micromachined probe by Reck et. al [13] represented an important step toward establishing an on-wafer measurement infrastructure for the terahertz spectrum. The work in this thesis leverages that foundation to extend on-wafer measurement capabilities of micromachined probes to higher frequencies with improved performance and robustness. As a result, a new measurement tool exists that impacts an entire field of research.

Contributions of this Research

This work in this thesis makes the following contributions:

1. Chapter 2 described the identification of and solution to several micromachined probe robustness issues. The solutions outlined ensure: (1) that the

spring constant of the tip is linear, (2) the probe makes repeatable DC contact, (3) that the silicon does not fracture during normal use, and (4) that the probe does not cause delamination of the DUT contact pads. These issues are critical to the reliability of micromachined probes and allow their adoption as the basis for terahertz device characterization. In addition, the design of a new micromachined probe housing enables increased overall performance of the on-wafer measurement system.

2. Chapter 3 presented the design and characterization of the first WR-1.2 probe. This work successfully demonstrated the feasibility of using thinner ($5\ \mu\text{m}$) silicon substrates for micromachined probes, mitigation of the reduced tip spring constant through both length optimization and increased width, and expanded on-wafer capabilities to enable measurements to 900 GHz for the first time.
3. Chapter 4 details the design, characterization, and application of on the first on-wafer probe for the WR-1.0 waveguide band. Close analysis of the electromagnetic requirements enabled implementation of the design on $15\ \mu\text{m}$ thick silicon, which offers many benefits. Additionally, the design identified and addressed performance sensitivity issues associated with the bias filter, and this change was largely responsible for the successful full-band performance exhibited by the probe. The WR-1.0 probes enabled on-wafer measurements to 1.1 THz for the first time, with a demonstrated calibrated dynamic range of approximately 25-30 dB.

Future Work

The flexibility and precision afforded by the probe fabrication process could serve as foundation for future work in a number of areas, a few of which are described below.

Developing Higher Frequency Bands

The successful performance of the WR-1.0 probe design and the demonstration of micromachined probes on $5\ \mu\text{m}$ silicon substrates suggest that it should be possible to design a micromachined probe for operation beyond 1.1 THz. However, the probe is part of a measurement system, and should not be considered independently.

While rectangular waveguide has been used to WR-0.4 (1.8 - 2.8 THz) [51], the rapidly increasing attenuation of waveguide, shown in Fig. 5.1, exacerbates the declining output power and dynamic range of sources and receivers. In addition,

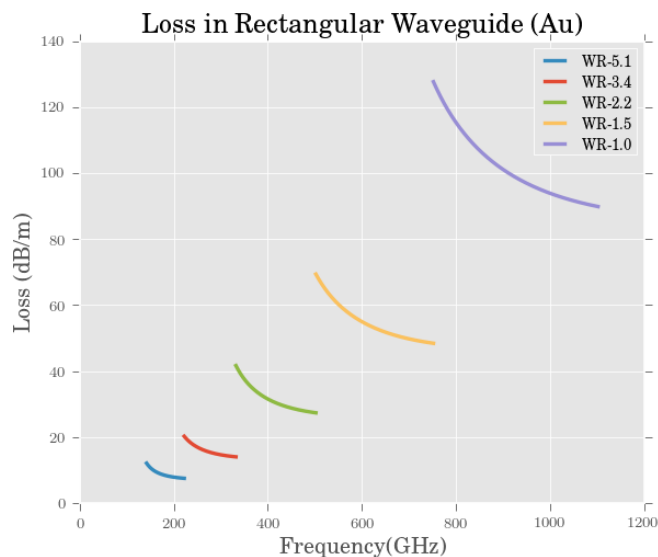


Figure 5.1: Rectangular waveguide attenuation (image generated by scikit-rf, courtesy of Alex Arsenovic).

beyond 1.1 THz, direct-contact rectangular waveguide interfaces are generally not preferred, as the misalignment associated with machining of the interface results in significant loss due to mismatch. Instead, waveguide based sources and receivers at these frequencies are typically quasi-optically coupled, where the waveguide is machined with an integral antenna termination and the circuitry is placed as close to the antenna as possible. Integration of such an antenna for quasi-optical coupling of the RF signal into the probe is conceivable, and may be a good option at sufficiently high frequencies. Therefore, while it may be possible to scale micromachined probes beyond 1.1 THz, the measurement system will need to be designed as a whole, likely placing the sources and receivers as close to the probe tips as possible.

Another interesting area of research on this front is investigation of other methods to mitigate the reduced spring constant associated with thinning of the silicon substrate. For example, it may be possible to add other materials to stiffen the probe tip. Or, it may be possible to use multi-layer silicon substrates to provide localized thinning in the RF channel.

Integration of Sensors and Devices

The microfabrication process of the probe tip lends itself to the integration of other circuit components. For example, Yu demonstrated the integration of strain sensors on the probe tip, shown in Fig. 5.2a, to permit sensing of contact force and probe tip planarity to improve measurement repeatability and extend probe tip lifetime [34, 52, 53]. Zhang reported a W-band probe that integrates a balun and common-mode matching network onto the probe tip, shown in Fig. 5.2b, for measurement of circuits with differential inputs [54].

Work by Alijabbari demonstrated GaAs Schottky diode-based frequency mul-

multipliers integrated on free-standing $15\ \mu\text{m}$ silicon substrates in a fabrication process compatible with that of the micromachined probes [25]. This is a potentially powerful capability, as it would allow integration of diode-based circuits such as multipliers, detectors, and mixers directly on the probe tip. For example, a 6-port reflectometer [55] or even a frequency extender could be integrated onto the probe [56], both alleviating the high loss associated with long waveguide sections. Research is already underway at the University of Virginia on the integrated 6-port reflectometer, as shown in Fig. 5.3.

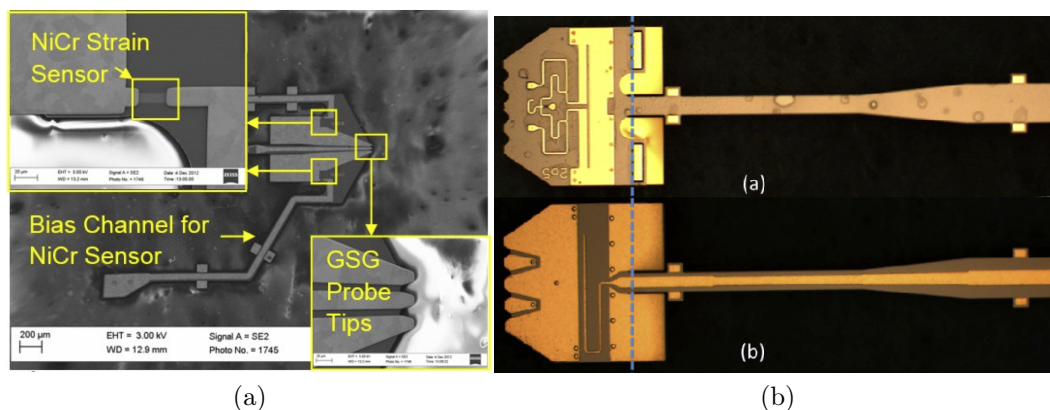


Figure 5.2: Micromachining probe circuit integration (a): integrated strain sensors, image from [53], (b): integrated balun with common-mode match, image from [54].

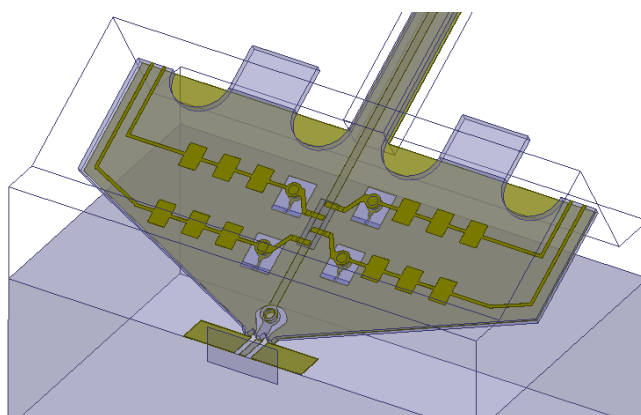


Figure 5.3: Simulation model of micromachined probe tip with integrated 6-port reflectometer.

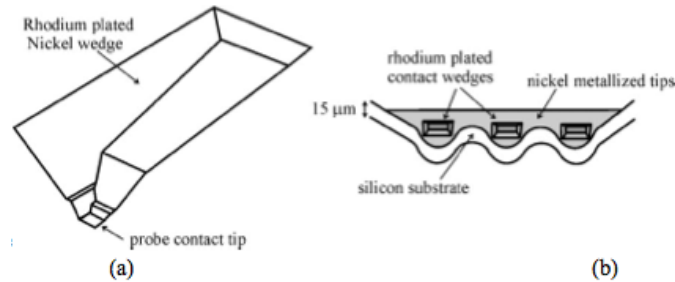


Figure 5.4: (a) Diagram of hard metal wedge utilized by Cascade Microtech for low-resistance contacts (image from [57]). (b) Cartoon illustrating rhodium plated wedges fabricated onto micromachined probe tips.

Engineering of the Tip Metallization

As discussed in Chapter 2, the probe tip contact resistance on aluminum is significantly less repeatable than on gold. To improve contact resistance to hard metal contacts, engineering of the probe tip metallization should be explored. The Cascade Microtech Infinity probe, which utilizes a wedge-shaped contact as shown in Fig. 5.4a, is well-known for its repeatable, low-resistance contact to aluminum pads. The outer surface of the wedge is rhodium, which is a hard (6.0 Mohs scale), non-oxidizing metal, with higher conductivity than nickel (2.3×10^7 S/m vs 1.4×10^7 S/m), and is therefore ideal for probe tip contacts. Integration of such a structure on the micromachined probe tips, as illustrated in Fig. 5.4b, may allow improved performance on aluminum. While metal structures of uniform cross-section are readily integrated into the current probe fabrication process, integration of a wedge-like is more difficult. The tip structures would most likely need to be fabricated separately on a sacrificial substrate. For example, anisotropic wet etching of silicon produces a pyramidal trench that could be plated with rhodium and/or nickel. A more complex structure such as the wedge shown in Fig. 5.4a would likely require an imprint tool to create a mold for plating. In both cases, the tip structures must

be transferred to the probe chip wafer to complete processing, requiring planarization, alignment, and bonding mechanisms. Both the formation and transfer of tip structures would require significant work.

Bibliography

- [1] P. Siegel, “Terahertz technology,” *Microwave Theory and Techniques, IEEE Transactions on*, vol. 50, no. 3, pp. 910–928, Mar. 2002.
- [2] Z. D. Taylor, R. S. Singh, M. O. Culjat, J. Y. Suen, W. S. Grundfest, and E. R. Brown, “THz imaging based on water-concentration contrast,” J. O. Jensen, H.-L. Cui, D. L. Woolard, and R. J. Hwu, Eds., vol. 6949, no. 1. SPIE, 2008, p. 69490D. [Online]. Available: <http://link.aip.org/link/?PSI/6949/69490D/1>
- [3] E. L. Jacobs, S. Moyer, C. C. Franck, F. C. DeLucia, C. Casto, D. T. Petkie, S. R. Murrill, and C. E. Halford, “Concealed weapon identification using terahertz imaging sensors,” D. L. Woolard, R. J. Hwu, M. J. Rosker, and J. O. Jensen, Eds., vol. 6212, no. 1. SPIE, 2006, p. 62120J. [Online]. Available: <http://link.aip.org/link/?PSI/6212/62120J/1>
- [4] V. Radisic, K. Leong, X. Mei, S. Sarkozy, W. Yoshida, and W. Deal, “Power amplification at 0.65 THz using InP HEMTs,” *Microwave Theory and Techniques, IEEE Transactions on*, vol. 60, no. 3, pp. 724–729, Mar. 2012.
- [5] W. Deal, K. Leong, V. Radisic, S. Sarkozy, B. Gorospe, J. Lee, P. Liu, W. Yoshida, J. Zhou, M. Lange, R. Lai, and X. Mei, “Low noise amplification

- at 0.67 THz using 30 nm InP HEMTs,” *Microwave and Wireless Components Letters, IEEE*, vol. 21, no. 7, pp. 368–370, Jul. 2011.
- [6] M. Seo, M. Urteaga, J. Hacker, A. Young, Z. Griffith, V. Jain, R. Pierson, P. Rowell, A. Skalare, A. Peralta, R. Lin, D. Pukala, and M. Rodwell, “InP HBT IC technology for terahertz frequencies: Fundamental oscillators up to 0.57 THz,” *Solid-State Circuits, IEEE Journal of*, vol. 46, no. 10, pp. 2203–2214, oct. 2011.
- [7] Waveguide infinity probe. [Online]. Available: <http://www.cmicro.com/products/probes/rf-microwave/infinity-probe/waveguide-infinity-probe/waveguide-infinity-probe>
- [8] Picoprobe model 220 high performance microwave probe. [Online]. Available: <http://ggb.com/220.html>
- [9] A. Rumiantsev and R. Doerner, “Rf probe technology: History and selected topics,” *Microwave Magazine, IEEE*, vol. 14, no. 7, pp. 46–58, Nov 2013.
- [10] A. Tessmann, A. Leuther, V. Hurm, I. Kallfass, H. Massler, M. Kuri, M. Riessle, M. Zink, R. Loesch, M. Seelmann-Eggebert, M. Schlechtweg, and O. Ambacher, “Metamorphic hemt mmics and modules operating between 300 and 500 ghz,” *Solid-State Circuits, IEEE Journal of*, vol. 46, no. 10, pp. 2193–2202, Oct 2011.
- [11] A. Safwat, M. Andrews, L. Hayden, K. Gleason, and E. Strid, “A probe technology for 110+ ghz integrated circuits with aluminum pads,” in *ARFTG Conference Digest, Spring 2002. 59th*, June 2002, pp. 60–66.

- [12] S. Liu and G. Boll, “A new probe for w-band on-wafer measurements,” in *Microwave Symposium Digest, 1993., IEEE MTT-S International*, June 1993, pp. 1335–1338 vol.3.
- [13] T. J. Reck, L. Chen, C. Zhang, C. Groppi, H. Xu, A. Arsenovic, N. S. Barker, A. Lichtenberger, and R. M. Weikle, “Micromachined on-wafer probes,” in *Microwave Symposium Digest, 2010., IEEE MTT-S International*, June 2010.
- [14] T. Reck, L. Chen, C. Zhang, A. Arsenovic, C. Groppi, A. Lichtenberger, R. Weikle, and N. Barker, “Micromachined probes for submillimeter-wave on-wafer measurements-part I: Mechanical design and characterization,” *Terahertz Science and Technology, IEEE Transactions on*, vol. 1, no. 2, pp. 349–356, Nov. 2011.
- [15] —, “Micromachined probes for submillimeter-wave on-wafer measurements-part II: RF design and characterization,” *Terahertz Science and Technology, IEEE Transactions on*, vol. 1, no. 2, pp. 357–363, Nov. 2011.
- [16] R. Bass, A. Lichtenberger, R. Weikle, S. Pan, E. Bryerton, and C. Walker, “Ultra-thin silicon chips for submillimeter-wave applications,” in *Fifteenth International Symposium on Space THz Technology*, 2004, pp. 392–399.
- [17] X. Li, T. Kasai, S. Nakao, H. Tanaka, T. Ando, M. Shikida, and K. Sato, “Measurement for fracture toughness of single crystal silicon film with tensile test,” *Sensors and Actuators A: Physical*, vol. 119, no. 1, pp. 229 – 235, 2005.
- [18] T. Reck, “Submillimeter Wavelength Metrology Components,” Ph.D. dissertation, University of Virginia, 2010.

- [19] L. Chen, "Micromachined Millimeter- and Submillimeter-wave Circuits for Test and Integration," Ph.D. dissertation, University of Virginia, 2012.
- [20] L. Chen, C. Zhang, T. J. Reck, A. Arsenovic, M. Bauwens, C. Groppi, A. W. Lichtenberger, R. M. Weikle, and N. S. Barker, "Terahertz micromachined on-wafer probes: Repeatability and reliability," *Microwave Theory and Techniques, IEEE Transactions on*, vol. PP, no. 99, pp. 1–9, 2012.
- [21] L. Chen, C. Zhang, T. Reck, C. Groppil, A. Arsenovic, A. Lichtenberger, R. Weikle, and N. Barker, "Terahertz micromachined on-wafer probes: Repeatability and robustness," in *Microwave Symposium Digest (MTT), 2011 IEEE MTT-S International*, june 2011, pp. 1–4.
- [22] C. Zhang, "Development of Single-ended and Balun Integrated Probes for THz Applications," Ph.D. dissertation, University of Virginia, 2014.
- [23] W. Haynes, *CRC Handbook of Chemistry and Physics, 94th Edition*, 2014.
- [24] G. S. Ferguson, M. K. Chaudhury, G. B. Sigal, and G. M. Whitesides, "Contact adhesion of thin gold films on elastomeric supports: Cold welding under ambient conditions," *Science*, vol. 253, no. 5021, pp. pp. 776–778, 1991.
- [25] N. Alijabbari, "Submillimeter-Wave Quasi-Vertical GaAs Schottky Diodes Integrated on Silicon Membranes," Ph.D. dissertation, University of Virginia, 2014.
- [26] L. Chen, A. Arsenovic, J. Stanec, T. Reck, A. Lichtenberger, R. Weikle, and N. Barker, "A micromachined terahertz waveguide 90 degree twist," *Microwave and Wireless Components Letters, IEEE*, vol. 21, no. 5, pp. 234–236, May 2011.

- [27] F. Beer, J. Johnston, J. DeWolf, and D. Mazurek, *Mechanics of Materials*. McGraw-Hill Education, 2014.
- [28] J. Kooi, G. Chattopadhyay, S. Withington, F. Rice, J. Zmuidzinas, C. Walker, and G. Yassin, “A full-height waveguide to thin-film microstrip transition with exceptional rf bandwidth and coupling efficiency,” *International Journal of Infrared and Millimeter Waves*, vol. 24, no. 3, pp. 261–284, 2003.
- [29] A. Arsenovic, L. Chen, M. Bauwens, H. Li, N. Barker, and R. Weikle, “An experimental technique for calibration uncertainty analysis,” *Microwave Theory and Techniques, IEEE Transactions on*, vol. 61, no. 1, pp. 263–269, Jan 2013.
- [30] J. Bauer, R.F. and P. Penfield, “De-embedding and unterminating,” *Microwave Theory and Techniques, IEEE Transactions on*, vol. 22, no. 3, pp. 282–288, Mar 1974.
- [31] D. Blackham, “Application of weighted least squares to osl vector error correction,” in *ARFTG Conference Digest, Spring 2003. 61st*, June 2003, pp. 11–21.
- [32] A. Tessmann, A. Leuther, H. Massler, and M. Seelmann-Eggebert, “A high gain 600 ghz amplifier tmic using 35 nm metamorphic hemt technology,” in *Compound Semiconductor Integrated Circuit Symposium (CSICS), 2012 IEEE*, Oct 2012, pp. 1–4.
- [33] J. Hacker, M. Urteaga, M. Seo, A. Skalare, and R. Lin, “Inp hbt amplifier mmics operating to 0.67 thz,” in *Microwave Symposium Digest (IMS), 2013 IEEE MTT-S International*, June 2013, pp. 1–3.
- [34] Q. Yu, M. Bauwens, A. Lichtenberger, R. Weikle II, and N. Barker, “Measurement uncertainty characterization of terahertz large wafer probing,” in

- Microwave Symposium Digest (IMS), 2014 IEEE MTT-S International*, June 2014.
- [35] K. Schmalz, J. Borngraber, R. Wang, Y. Mao, C. Meliani, W. Debski, and W. Winkler, "Subharmonic 245 ghz sige receiver with antenna," in *Microwave Integrated Circuits Conference (EuMIC), 2013 European*, Oct 2013, pp. 121–124.
- [36] F. Golcuk, O. Gurbuz, and G. Rebeiz, "A 0.39-0.44 thz 2x4 amplifier-quadrupler array with peak eirp of 3-4 dbm," *Microwave Theory and Techniques, IEEE Transactions on*, vol. 61, no. 12, pp. 4483–4491, Dec 2013.
- [37] R. Han and E. Afshari, "A broadband 480-ghz passive frequency doubler in 65-nm bulk cmos with 0.23mw output power," in *Radio Frequency Integrated Circuits Symposium (RFIC), 2012 IEEE*, June 2012, pp. 203–206.
- [38] C. Balanis, *Advanced Engineering Electromagnetics*, ser. CourseSmart Series. Wiley, 2012.
- [39] T. McMaster, M. Schneider, and W. SNELL, "Millimeter-wave receivers with subharmonic pump," *Microwave Theory and Techniques, IEEE Transactions on*, vol. 24, no. 12, pp. 948–952, Dec 1976.
- [40] P. Siegel, J. Oswald, R. Dengler, D. Sheen, and S. Ali, "Measured and computed performance of a microstrip filter composed of semi-insulating gaas on a fused quartz substrate," *Microwave and Guided Wave Letters, IEEE*, vol. 1, no. 4, pp. 78–80, April 1991.
- [41] J. Oswald and P. Siegel, "The application of the ftd method to millimeter-wave filter circuits including the design and analysis of a compact coplanar

- strip filter for thz frequencies,” in *Microwave Symposium Digest, 1994., IEEE MTT-S International*, May 1994, pp. 309–312 vol.1.
- [42] N. Marcuvitz and I. of Electrical Engineers, *Waveguide Handbook*, ser. IEE electromagnetic waves series. McGraw-Hill, 1951.
- [43] R. F. Harrington, *Time-harmonic electromagnetic fields*, ser. IEEE press series on electromagnetic wave theory. Piscataway, NJ: J. Wiley and sons New York Chichester Weinheim, 2001.
- [44] R. Simons, *Coplanar Waveguide Circuits, Components, and Systems*, ser. Wiley Series in Microwave and Optical Engineering. Wiley, 2004.
- [45] D. Williams, C. Wang, and U. Arz, “An optimal multiline trl calibration algorithm,” in *Microwave Symposium Digest, 2003 IEEE MTT-S International*, vol. 3, June 2003, pp. 1819–1822 vol.3.
- [46] A. Fung, L. Samoska, D. Pukala, D. Dawson, P. Kangaslahti, M. Varonen, T. Gaier, C. Lawrence, G. Boll, R. Lai, and X. Mei, “On-wafer s-parameter measurements in the 325-508 GHz band,” *Terahertz Science and Technology, IEEE Transactions on*, vol. 2, no. 2, pp. 186 –192, Mar. 2012.
- [47] D. Kasilingam and D. Rutledge, “Surface-wave losses of coplanar transmission lines,” in *Microwave Symposium Digest, 1983 IEEE MTT-S International*, May 1983, pp. 113–116.
- [48] E. Godshalk, “Surface wave phenomenon in wafer probing environments,” in *ARFTG Conference Digest-Fall, 40th*, vol. 22, Dec 1992, pp. 10–19.

- [49] Y. Zhu, S. Vegesna, V. Kuryatkov, M. Holtz, M. Saed, and A. A. Bernussi, “Terahertz bandpass filters using double-stacked metamaterial layers,” *Opt. Lett.*, vol. 37, no. 3, pp. 296–298, Feb 2012.
- [50] D. Williams, A. Young, and M. Urteaga, “A prescription for sub-millimeter-wave transistor characterization,” *Terahertz Science and Technology, IEEE Transactions on*, vol. 3, no. 4, pp. 433–439, July 2013.
- [51] J. Hesler, H. Xu, T. Reck, and T. Crowe, “Development and testing of a 2.5 thz schottky mixer,” in *Infrared, Millimeter and Terahertz Waves (IRMMW-THz), 2011 36th International Conference on*, Oct 2011, pp. 1–2.
- [52] Q. Yu, M. Bauwens, C. Zhang, A. Lichtenberger, R. Weikle, and N. Barker, “Integrated strain sensor for micromachined terahertz on-wafer probe,” in *Microwave Symposium Digest (IMS), 2013 IEEE MTT-S International*, June 2013, pp. 1–4.
- [53] —, “Improved micromachined terahertz on-wafer probe using integrated strain sensor,” *Microwave Theory and Techniques, IEEE Transactions on*, vol. 61, no. 12, pp. 4613–4620, Dec 2013.
- [54] C. Zhang, M. Bauwens, N. Barker, R. M. Weikle, and A. W. Lichtenberger, “A w-band balun integrated probe with common mode matching network,” in *Microwave Symposium (IMS), 2014 IEEE MTT-S International*, June 2014, pp. 1–4.
- [55] G. F. Engen, “The six-port reflectometer: An alternative network analyzer,” *Microwave Theory and Techniques, IEEE Transactions on*, vol. 25, no. 12, pp. 1075–1080, Dec 1977.

- [56] R. Majidi-Ahy, M. Shakouri, and D. Bloom, “100 ghz active electronic probe for on-wafer s-parameter measurements,” *Electronics Letters*, vol. 25, no. 13, pp. 828–830, June 1989.
- [57] R. Gleason, M. Bayne, K. Smith, T. Lesher, and M. Koxxy, “Membrane probing method using improved contact,” Dec. 5 2013, uS Patent App. 13/901,328.

List of Publications

- [1] M. Bauwens, L. Chen, C. Zhang, A. Arsenovic, N. Alijabbari, A. Lichtenberger, N. Barker, and R. Weikle II, “Characterization of micromachined on-wafer probes for the 600 - 900 ghz waveguide band,” *Terahertz Science and Technology, IEEE Transactions on*, vol. 4, no. 4, pp. 527–529, July 2014.
- [2] M. F. Bauwens, N. Alijabbari, A. W. Lichtenberger, N. Barker, and R. M. Weikle, “A 1.1 thz micromachined on-wafer probe,” in *Microwave Symposium (IMS), 2014 IEEE MTT-S International*, June 2014, pp. 1–4.
- [3] Q. Yu, M. Bauwens, C. Zhang, A. Lichtenberger, R. Weikle, and N. Barker, “Improved micromachined terahertz on-wafer probe using integrated strain sensor,” *Microwave Theory and Techniques, IEEE Transactions on*, vol. 61, no. 12, pp. 4613–4620, Dec 2013.
- [4] R. Weikle, N. Barker, A. Lichtenberger, and M. Bauwens, “Micromachined probes for on-wafer measurement of millimeter- and submillimeter-wave devices and components,” in *Global Conference on Signal and Information Processing (GlobalSIP), 2013 IEEE*, Dec 2013, pp. 707–710.
- [5] S. Hawasli, M. Bauwens, A. Lichtenberger, N. Barker, and R. Weikle, “Characterization of submillimeter-wave schottky diodes in the 500 - 750 ghz band using

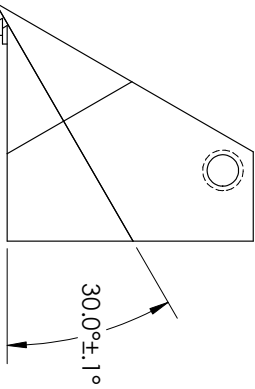
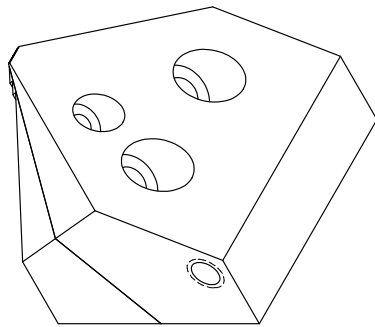
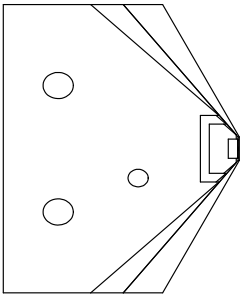
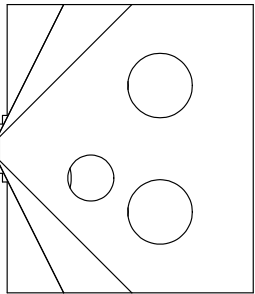
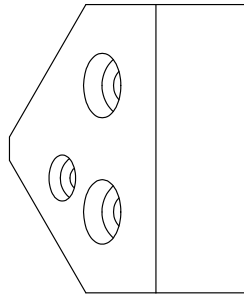
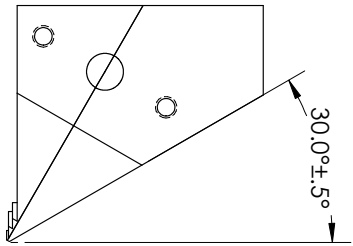
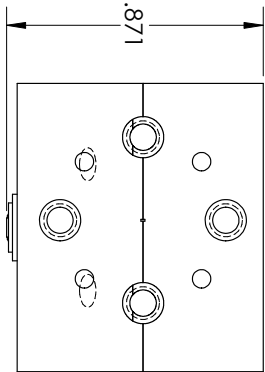
- micromachined on-wafer probes,” in *Microwave Symposium Digest (IMS), 2013 IEEE MTT-S International*, June 2013, pp. 1–4.
- [6] A. Arsenovic, L. Chen, M. Bauwens, H. Li, N. Barker, and R. Weikle, “An experimental technique for calibration uncertainty analysis,” *Microwave Theory and Techniques, IEEE Transactions on*, vol. 61, no. 1, pp. 263–269, Jan 2013.
- [7] M. Bauwens, L. Chen, C. Zhang, A. Arsenovic, A. Lichtenberger, N. Barker, and R. Weikle, “A terahertz micromachined on-wafer probe for wr-1.2 waveguide,” in *Microwave Integrated Circuits Conference (EuMIC), 2012 7th European*, Oct 2012, pp. 88–91.
- [8] L. Chen, C. Zhang, T. Reck, A. Arsenovic, M. Bauwens, C. Groppi, A. Lichtenberger, R. Weikle, and N. Barker, “Terahertz micromachined on-wafer probes: Repeatability and reliability,” *Microwave Theory and Techniques, IEEE Transactions on*, vol. 60, no. 9, pp. 2894–2902, Sept 2012.
- [9] R. Weikle II, N. Barker, A. Lichtenberger, T. Reck, L. Chen, C. Zhang, A. Arsenovic, and M. Bauwens, “Micromachined probes for on-wafer characterization of terahertz and submillimeter-wave components,” in *Infrared, Millimeter and Terahertz Waves (IRMMW-THz), 2011 36th International Conference on*, Oct 2011, pp. 1–2.

Appendix A

WR-1.2 Probe Housing Mechanical Drawings

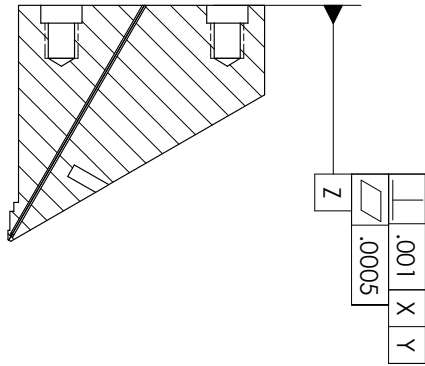
All dimensions listed in inches.

Assembly -
 External Overview
 All tolerances $\pm .009$
 unless otherwise noted



Rear - waveguide
flange detail

Sheet scale 6:1

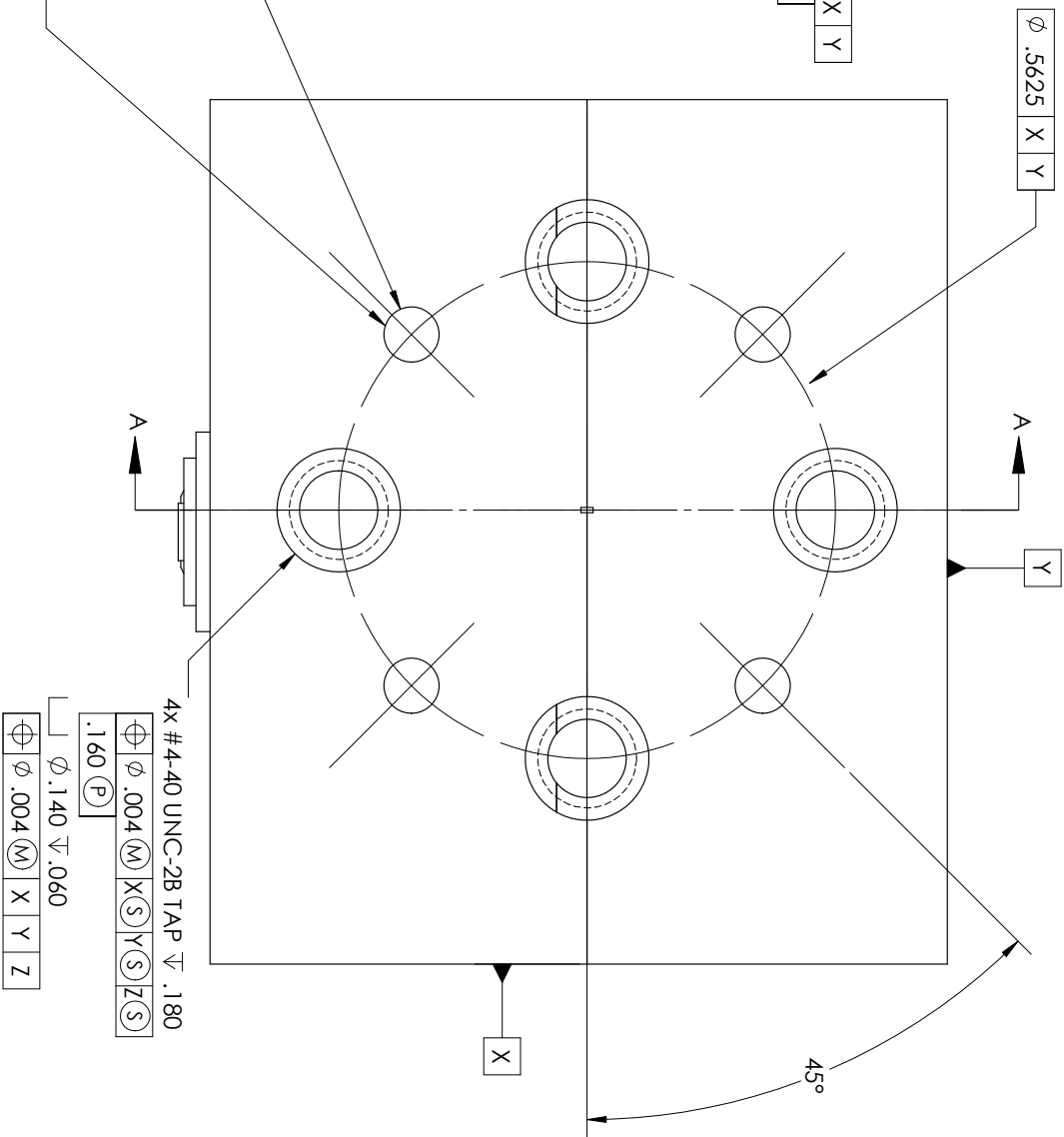


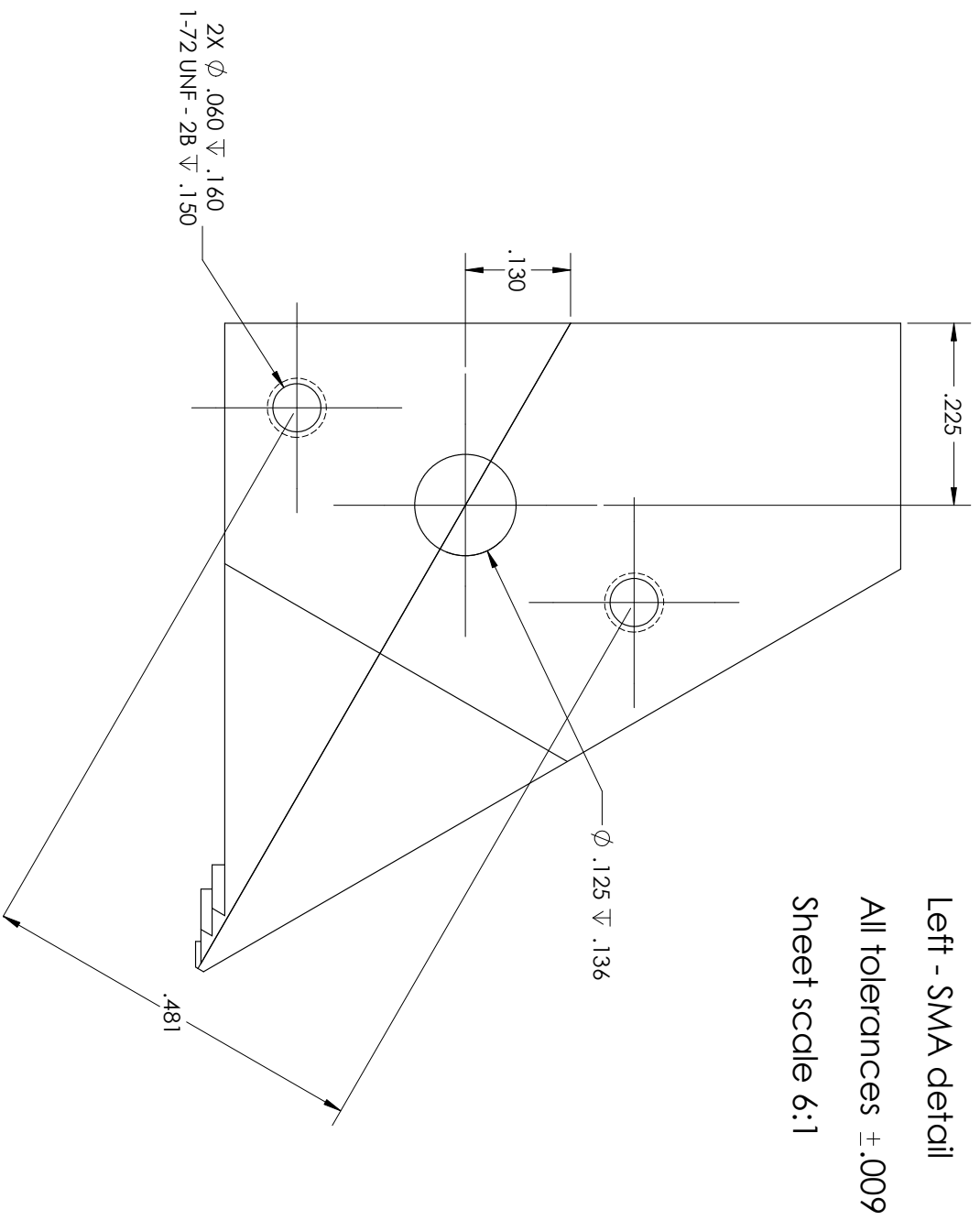
SECTION A-A
SCALE 2:1

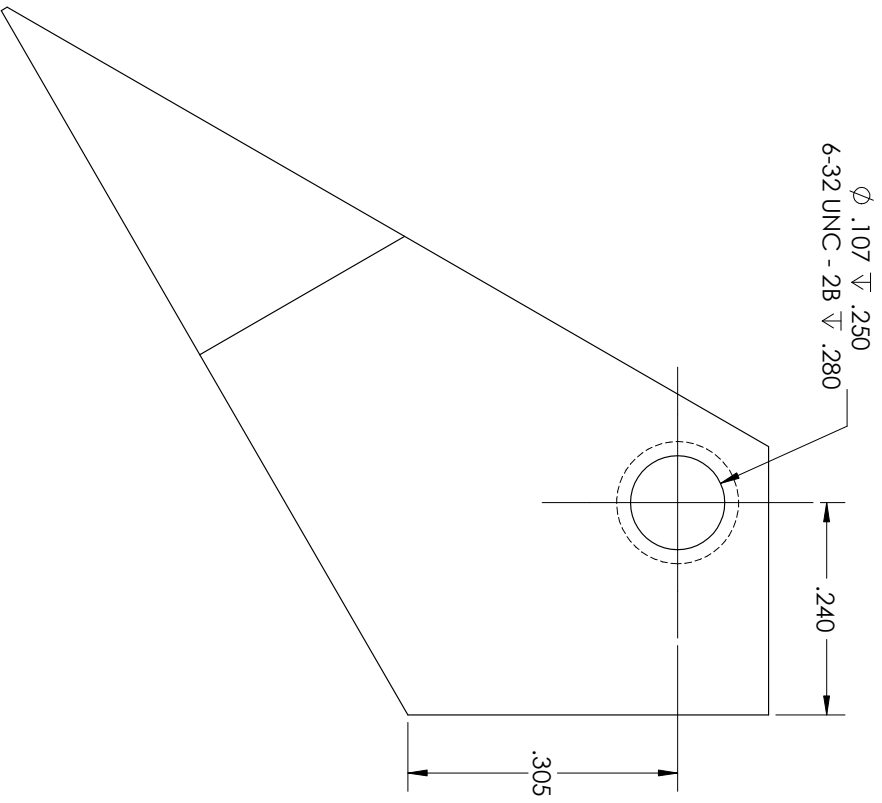
4X $\phi .0625^{+.0003}_{-.0000}$ $\nabla .180$

$\phi .001$	M	X	S	Y	S	Z	S
.160	P						

 NOTE THAT ALL 4 HOLES ARE
 TO ACCEPT SLIP FIT DOWEL PINS
 NO PINS WILL BE INSTALLED







Top piece

Right side - mounting hole

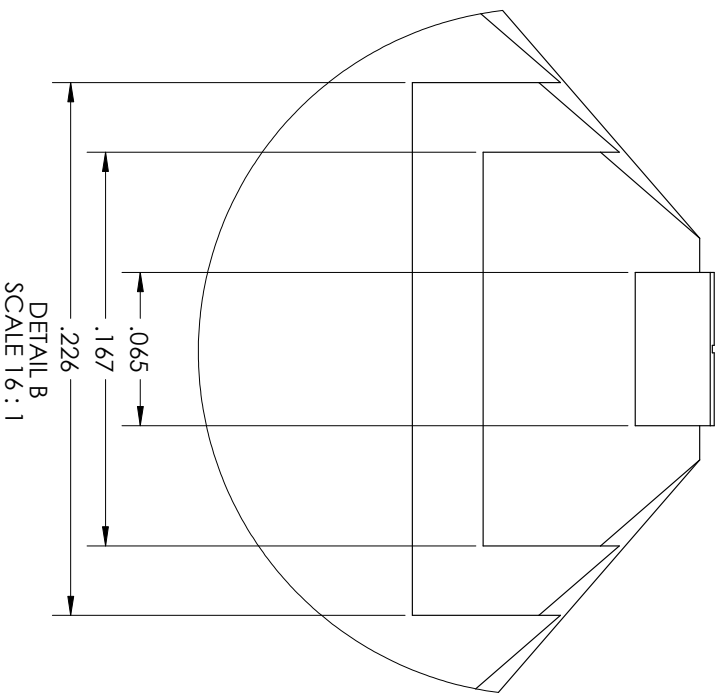
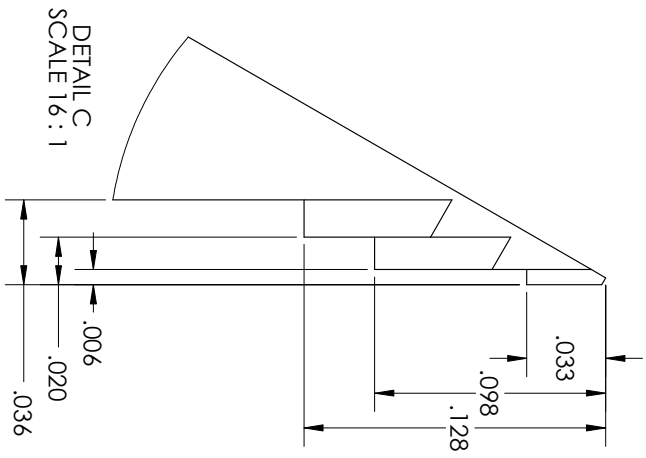
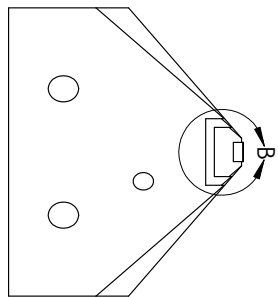
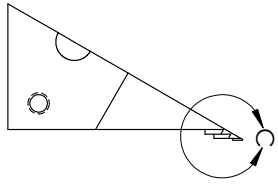
All tolerances $\pm .009$

Sheet scale 6:1

Bottom piece - stepped relief detail

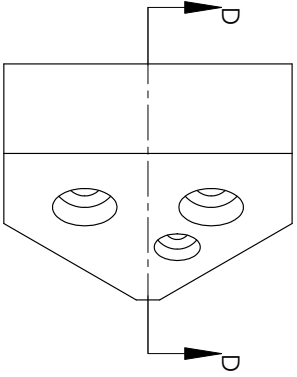
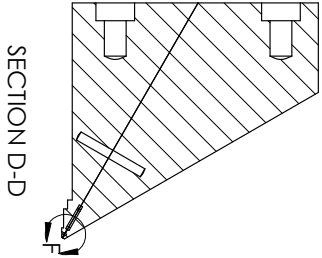
All tolerances $\pm .002$

Sheet scale 2:1

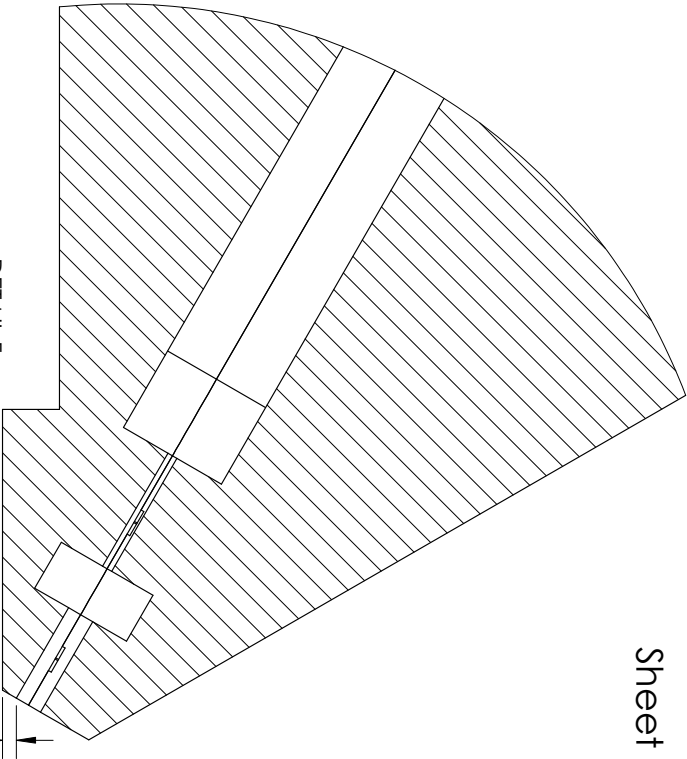


Tip section detail

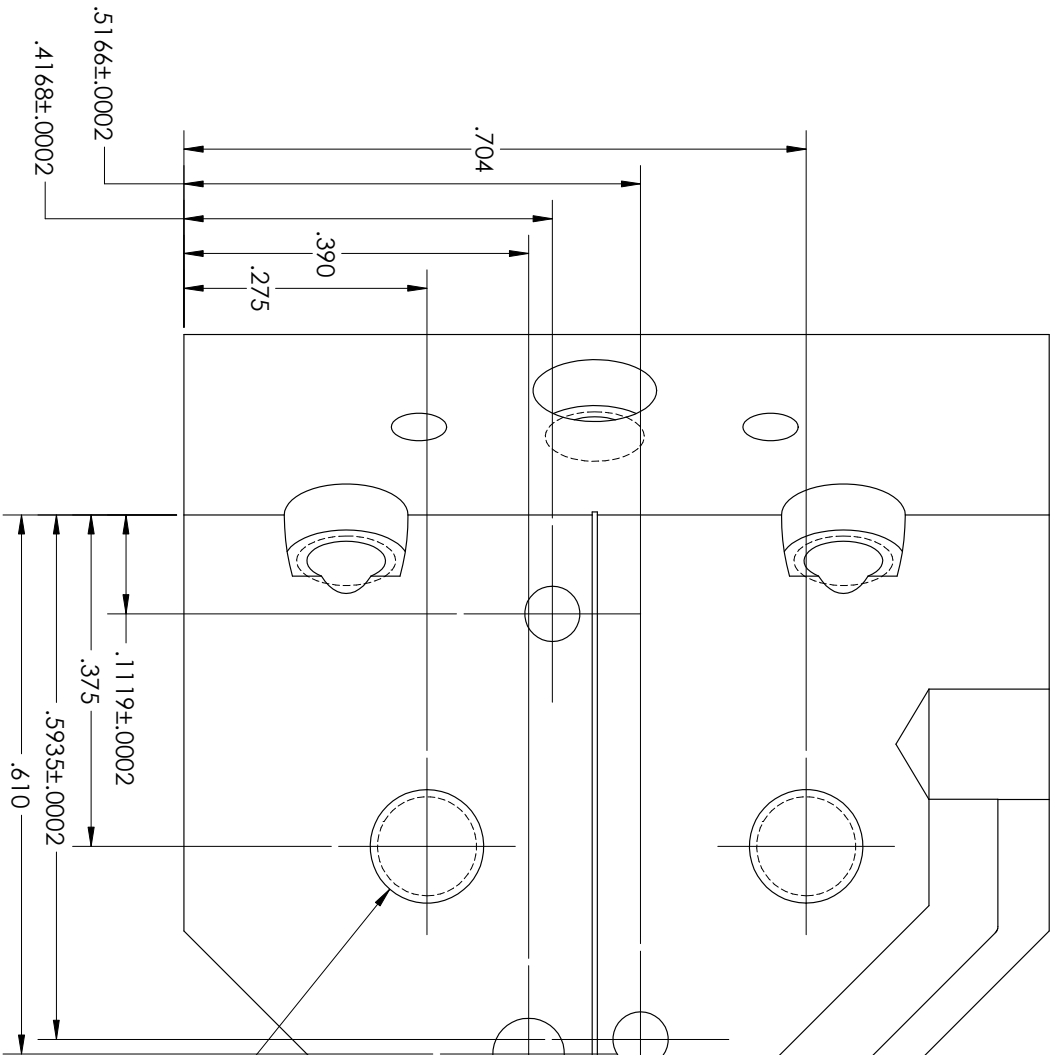
Sheet scale 2:1



DETAIL F
SCALE 60:1



$.0016^{+.0004}$
 $-.0000$



Top hole locations

View: Top half, looking down on split plane

All tolerances $\pm .009$ unless otherwise notec

Sheet scale 6:1

2x drill ~ 0.125 " deep for $\sim 1/16$ " x $1/4$ " dowel pin, SLIP FIT

#1 clearance hole

2x #4 clearance hole

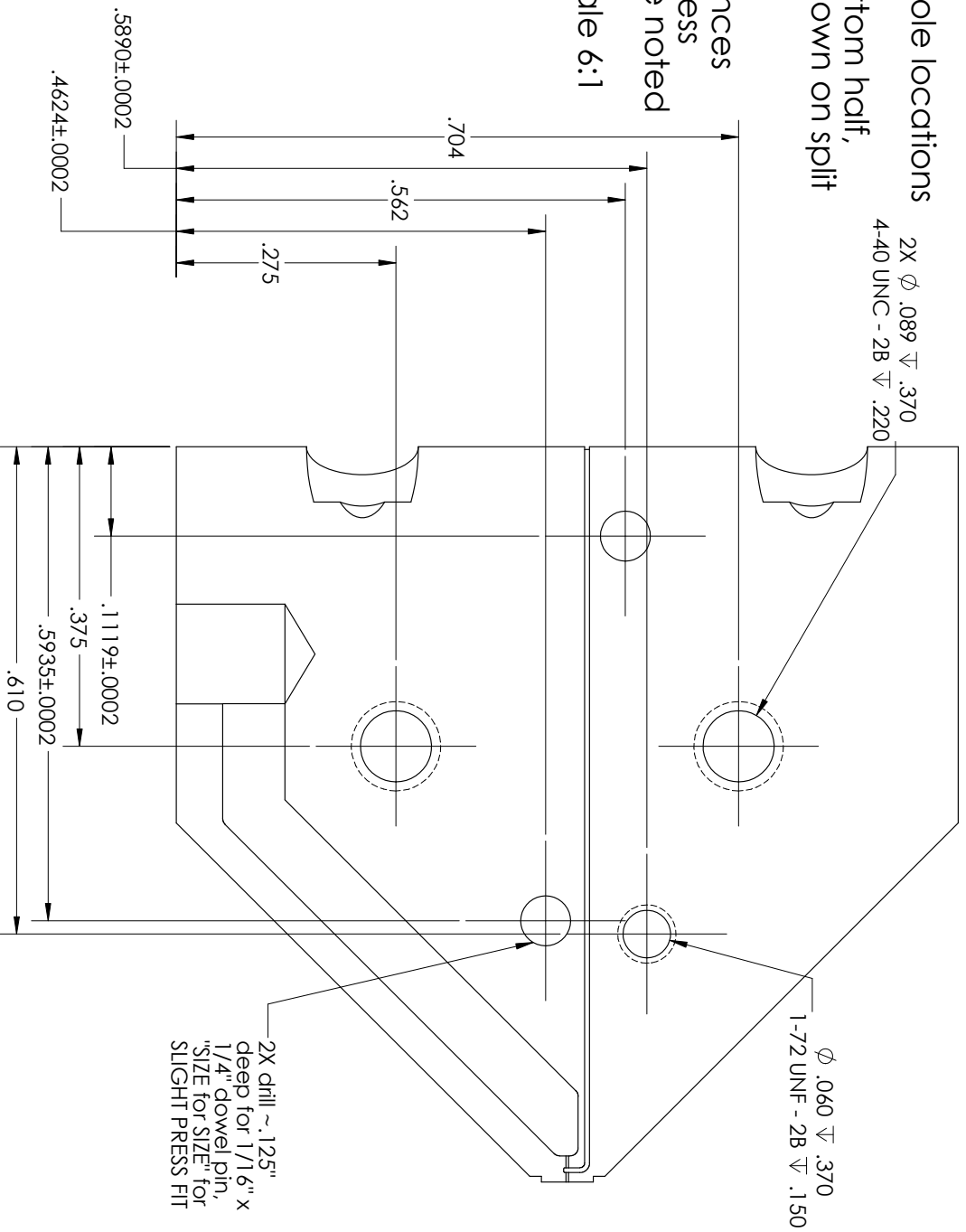
Bottom hole locations

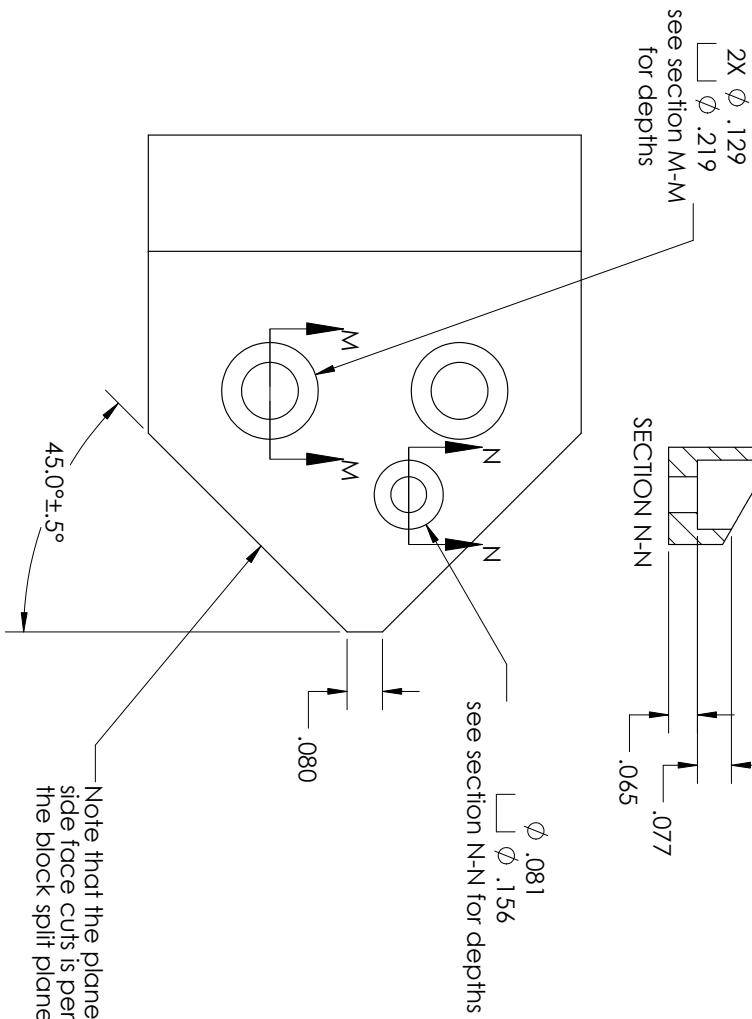
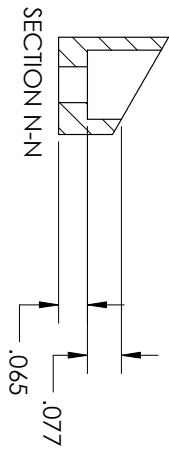
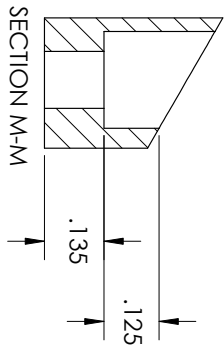
2X ϕ .089 ∇ .370
4-40 UNC - 2B ∇ .220

View: Bottom half,
looking down on split
plane

All tolerances
 \pm .009 unless
otherwise noted

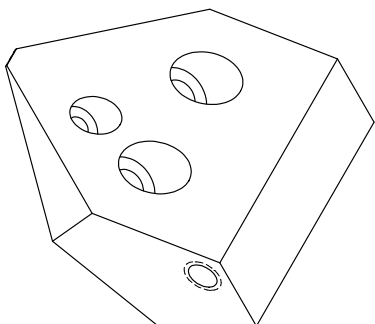
Sheet scale 6:1

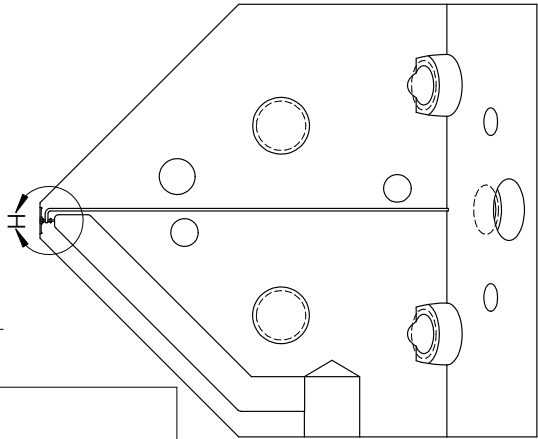




Face cuts,
counterbore, and
clearance hole detail
All tolerances $\pm .002$
unless otherwise
noted

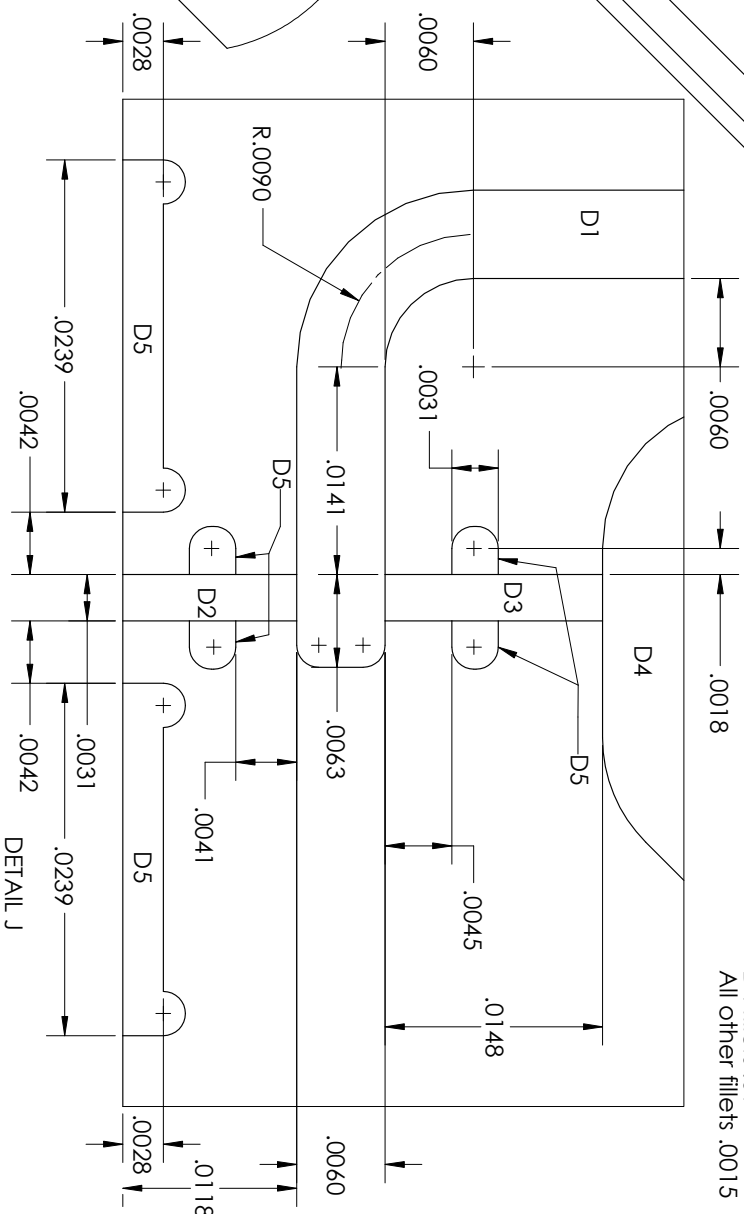
Sheet scale 3:1





Top channel/waveguide detail
 View: Top half, looking down on split plane
 All tolerances $\pm .0001$ unless otherwise noted

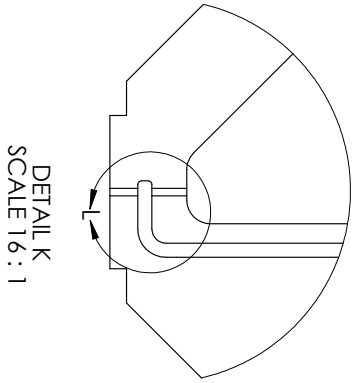
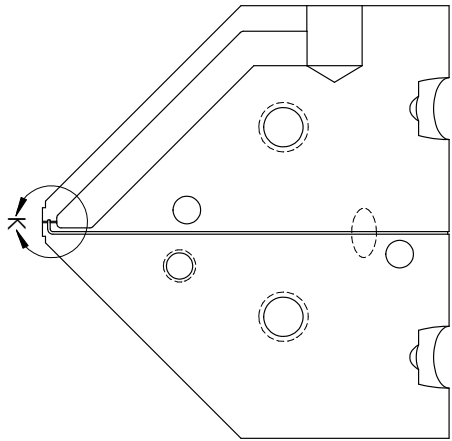
Sheet scale 3:1



DETAIL H
 SCALE 16:1

DETAIL J
 SCALE 100:1

- DEPTH TOLERANCES
 D1 - $.0060$
 D2 - $.0016$
 D3 - $.0006$
 D4 - $.0128$
 D5 - $.0003$
- DEPTH TOLERANCES
 D1-D3, D5 - $\pm .0001$
 D4 - $\pm .0005$
- D4 fillets .01
 All other fillets .0015



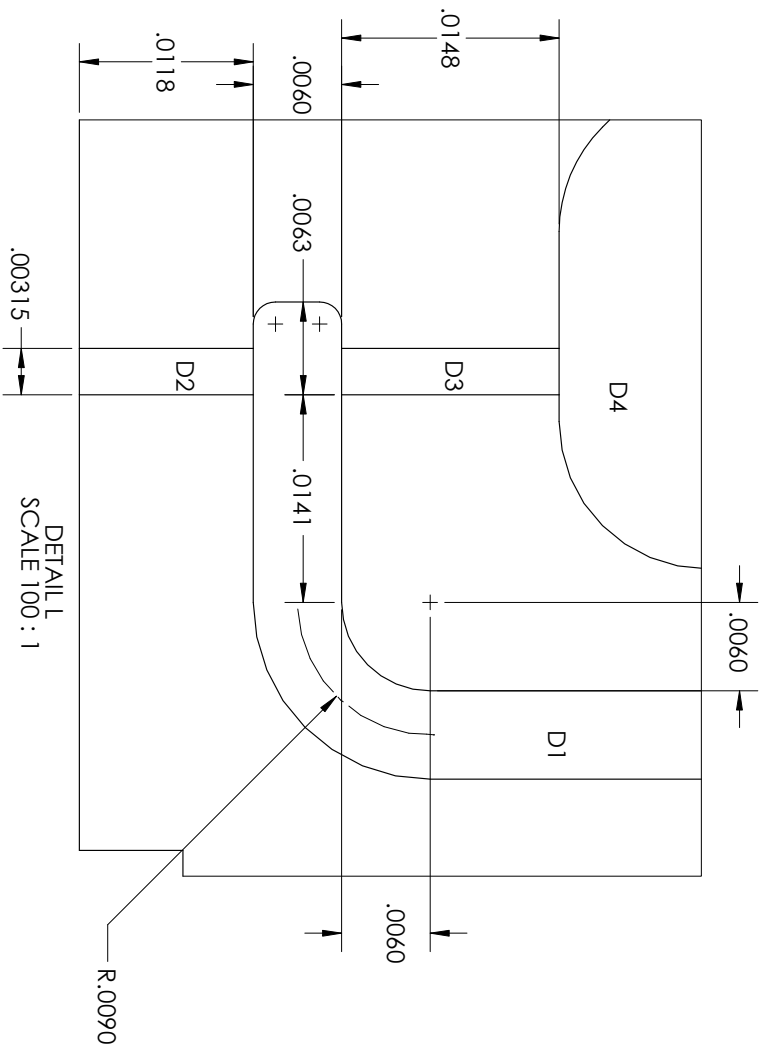
DETAIL K
SCALE 16 : 1

Bottom channel/waveguide detail
View: Bottom half, looking down on split plane

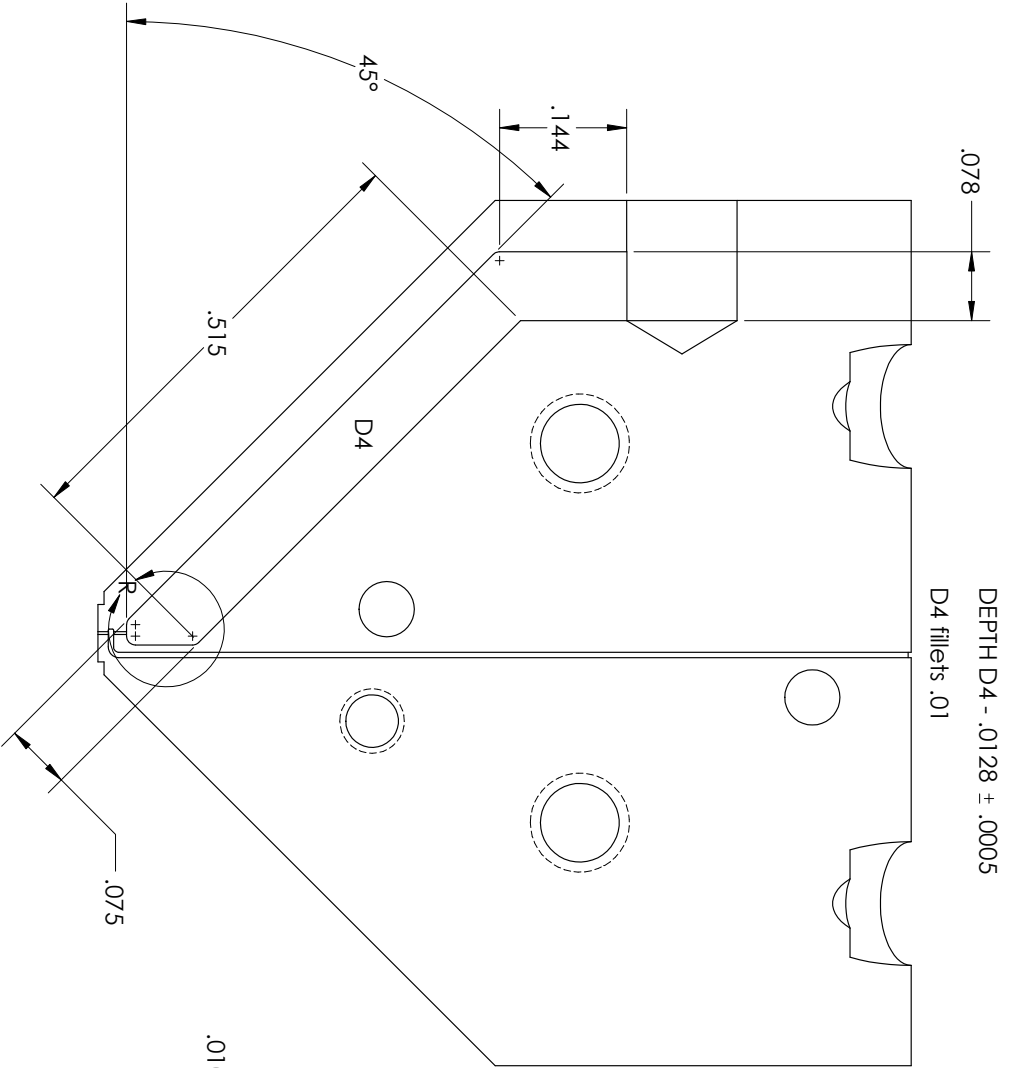
All tolerances $\pm .0001$ unless otherwise noted
Sheet scale 3:1

DEPTH TOLERANCES
D1 - .0060
D2 - .0016
D3 - .0006
D4 - .0128

DEPTH TOLERANCES
D1-D3 - $\pm .0001$
D4 - $\pm .0005$
D4 fillets .01
All other fillets .0015



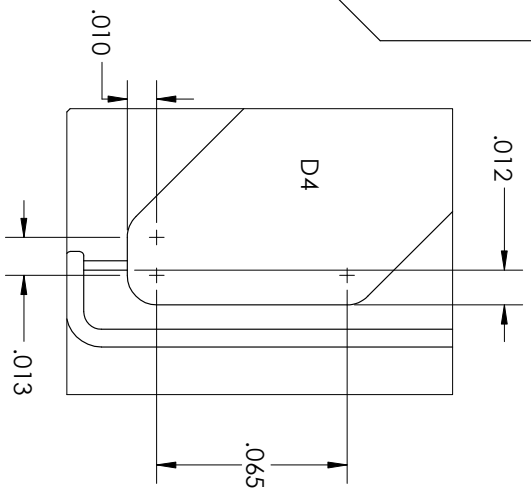
DETAIL L
SCALE 100 : 1



DEPTH D4 - $.0128 \pm .0005$
 D4 fillets .01

Bias channel detail
 View: Bottom half,
 looking down on
 split plane

All tolerances $\pm .001$
 unless otherwise noted
 Sheet scale 6:1



DETAIL R
 SCALE 20 : 1

Appendix B

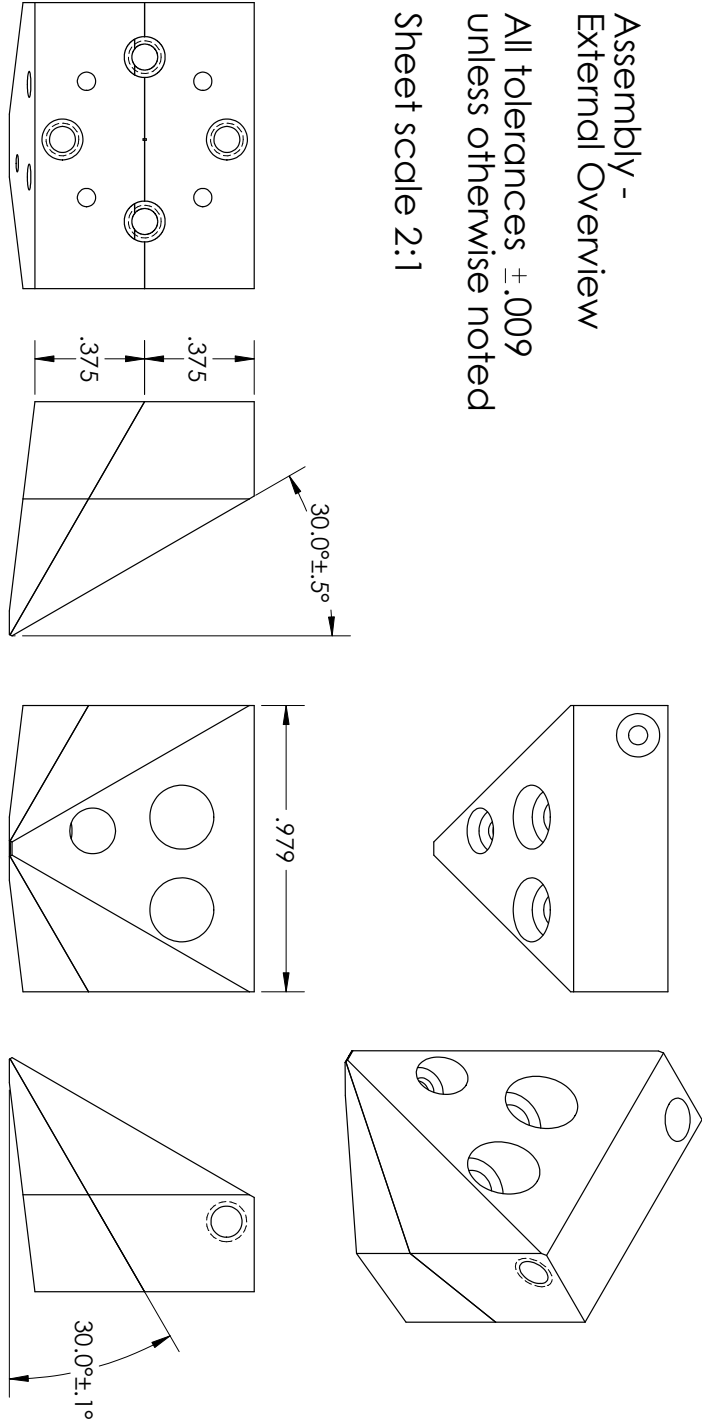
WR-1.0 Probe Housing Mechanical Drawings

All dimensions listed in inches.

Assembly - External Overview

All tolerances $\pm .009$
unless otherwise noted

Sheet scale 2:1

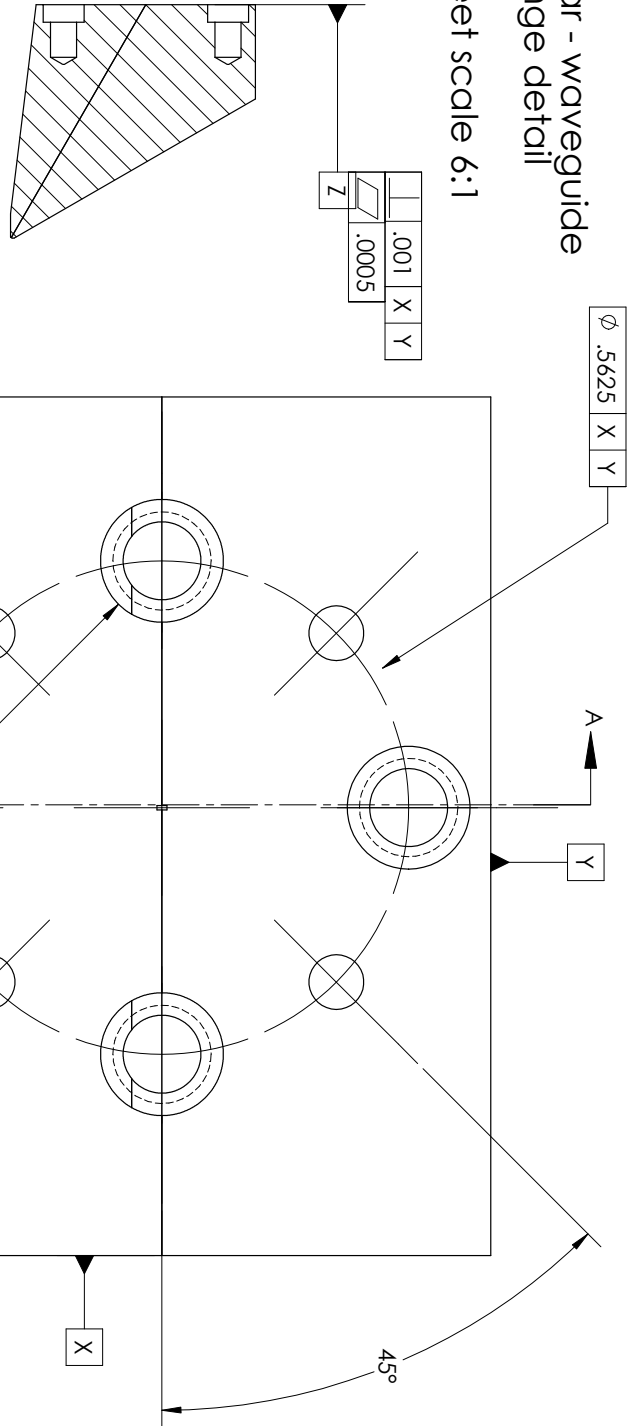


- The blocks should be gold-plated. The gold should be Grade A for wire-bonding:
- A. Zincation: Zincation of Aluminum surface to enable subsequent platings.
 - B. Barrier Layer: Nickel, Semi-bright 20-60 micro-inch (0.5-1.5 um) thick.
 - C. Gold Plate: 99.9% Min Purity, 75-125 micro-inch (1.9-3.1 um) thick.
(Knoop Hardness 90 max, Grade A).

Specified dimensions refer to the finished parts after plating.

Rear - waveguide
flange detail

Sheet scale 6:1



SECTION A-A
SCALE 2:1

4X $\phi .0625^{+.0003}_{-.0000} \nabla .180$
 $\phi .001$ (M) (X) (S) (Y) (S) (Z) (S)
 $\phi .160$ (P)

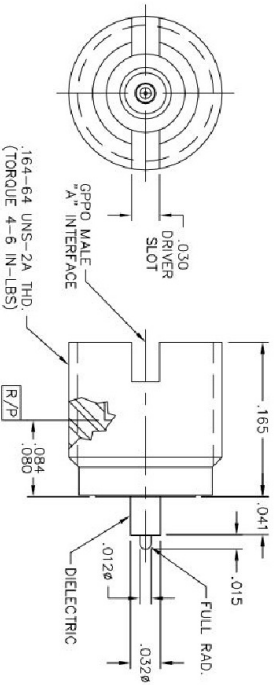
NOTE THAT ALL 4 HOLES ARE
TO ACCEPT SLIP FIT DOWEL PINS
NO PINS WILL BE INSTALLED

4X #4-40 UNC-2B TAP $\nabla .180$
 $\phi .004$ (M) (X) (S) (Y) (S) (Z) (S)
 $\phi .160$ (P)
 $\phi .140 \nabla .060$
 $\phi .004$ (M) (X) (Y) (Z)

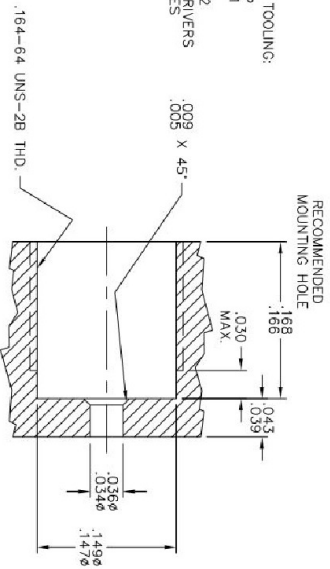
DATE REVISION: 12/5/00

PROTO NUMBER	"A" INTERFACE
B003-L33-01	FULL DETENT
B003-L35-01	SMOOTH BORE

MATERIAL AND FINISH: CRES 303; PASSIVATED
 SHROUD AND BUSHING: B&Q: GOLD PLATE 50-100 ? INCHES
 CENTER CONTACT: OVER NICKEL PLATE 50 ? INCHES MIN.
 DIELECTRIC: VIRGIN PTFE (TEFLON)

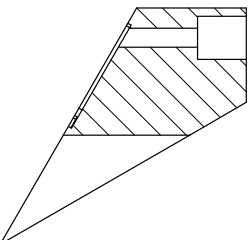


RECOMMENDED TOOLING:
 -STARTING TAP
 B099-A99-01
 -BOTTOM TAP
 B099-A99-02
 -THREAD-IN DRIVERS
 B097-A SERIES



GPPPO MALE THREAD-IN STRAIGHT TERMINAL (TAB DETENT)	IDENT CODE: 82316	GILBERT ENGINEERING
	REVISION: A	
SOURCE FILE: SK-1805	DWG. NO.: OL-B003-L3X-01	ASSY. PROC: -

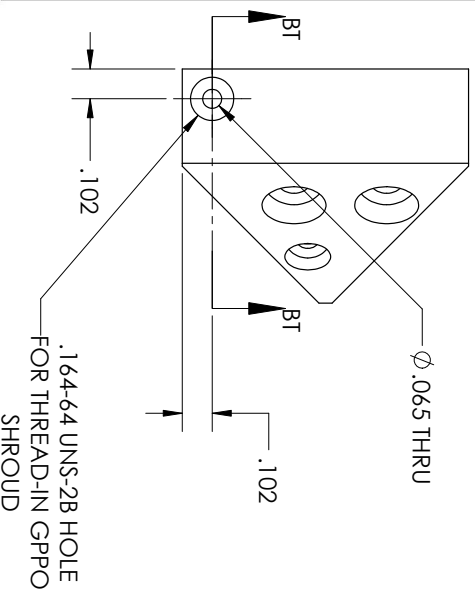
MANUFACTURER INFORMATION FOR THREAD-IN GPPPO SHROUD

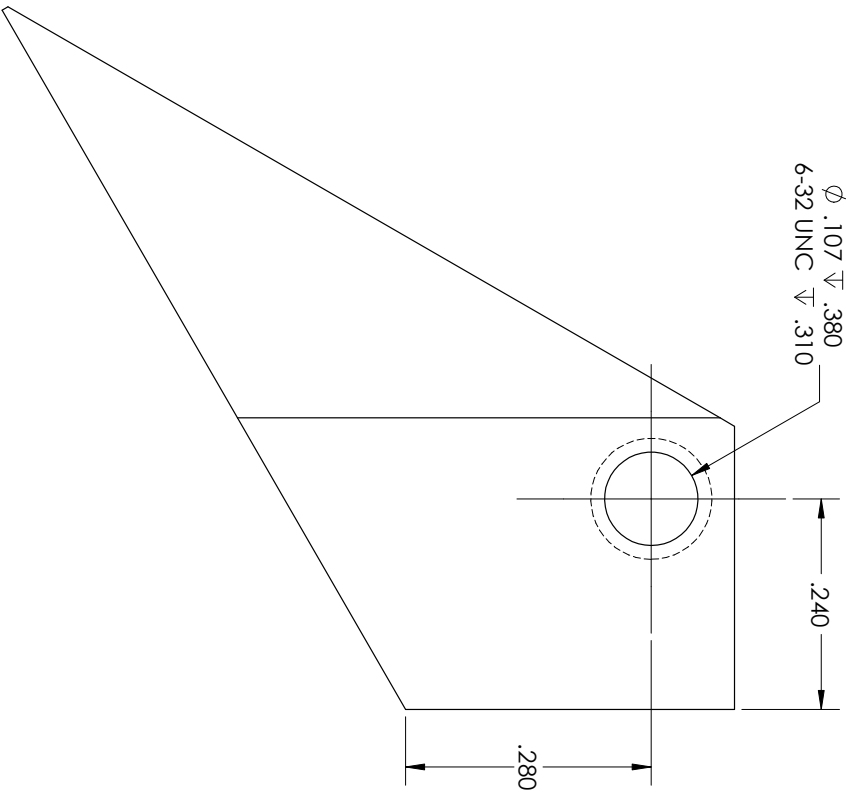


SECTION BT-BT
 SCALE 2 : 1

Manufacturer info provided for reference. GPPPO hole geometry does not necessarily need to be exactly as shown. All that is important is that the connector "seats" flush with (erring above) the top of the probe block.

GPPPO mount and hole
 All tolerances ±.009
 Sheet scale 2:1





Top piece

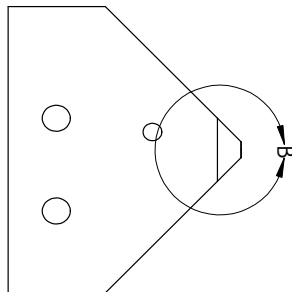
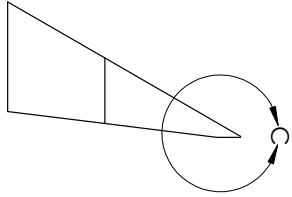
Right side - mounting
hole

All tolerances $\pm .009$

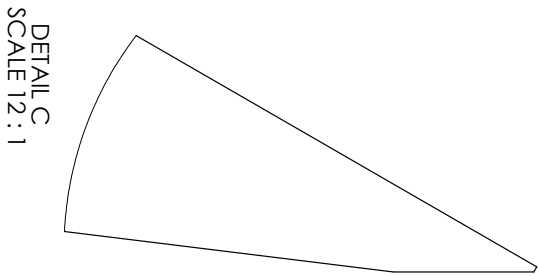
Sheet scale 6:1

Bottom piece - angled
relief detail

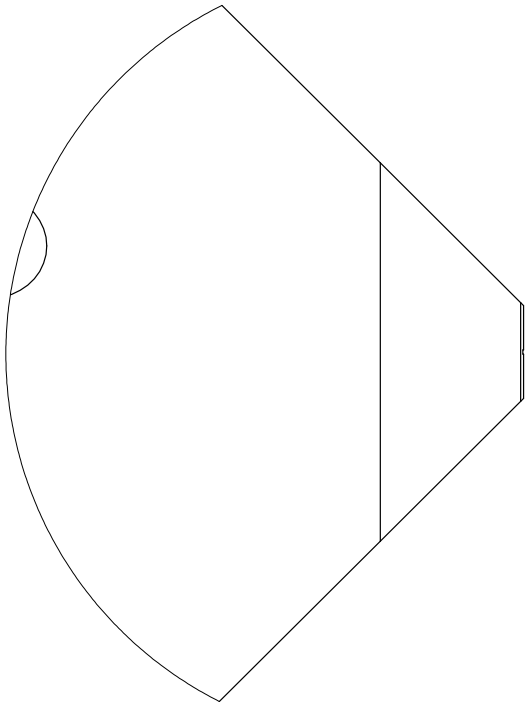
Sheet scale 2:1



$.080 \pm .010$

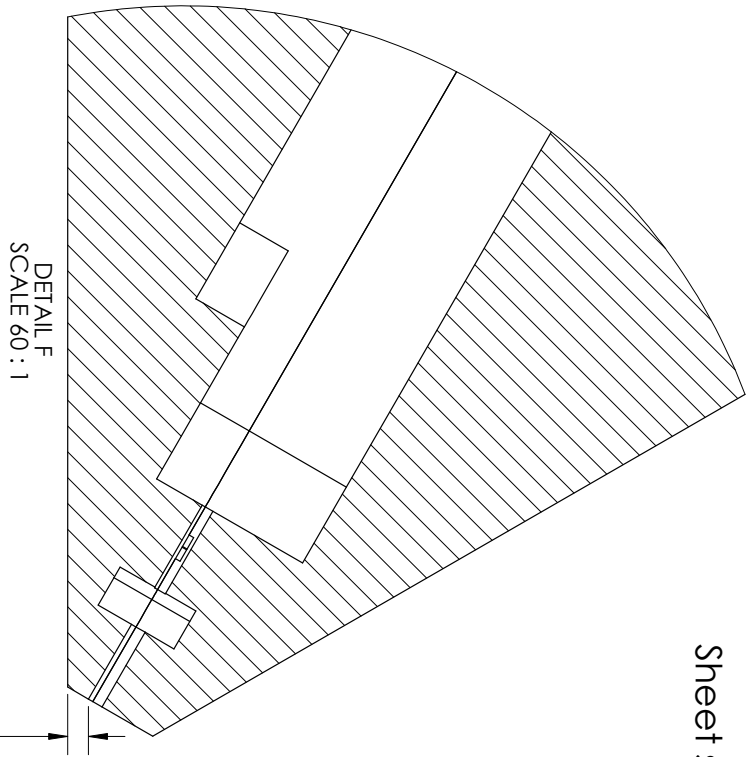
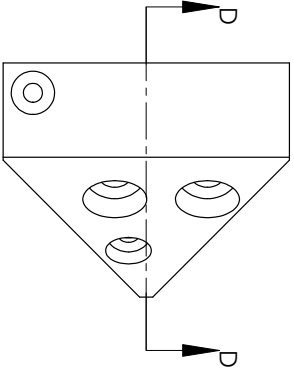
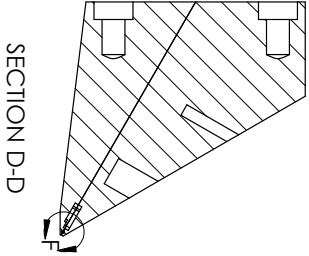


DETAIL C
SCALE 12:1

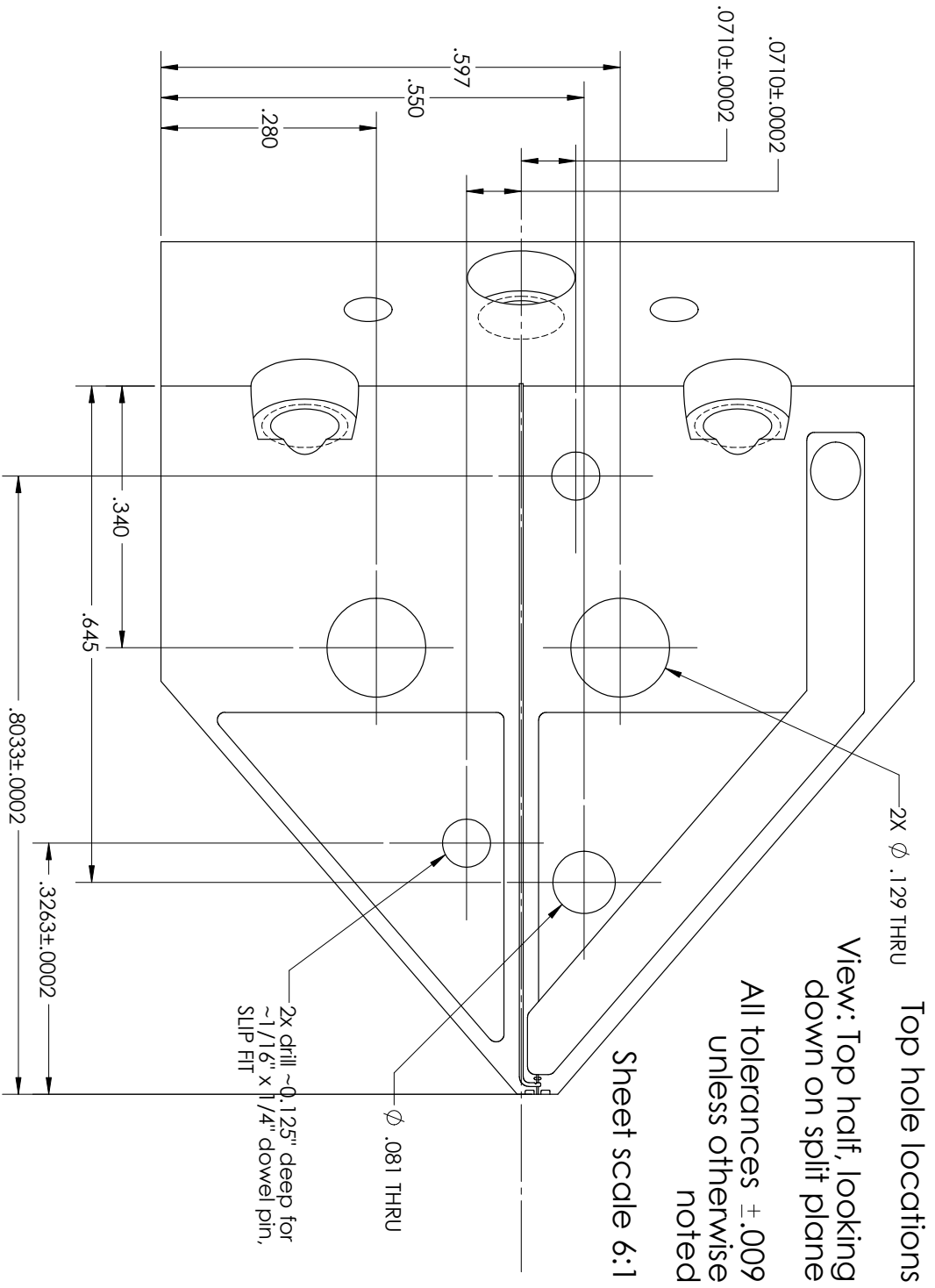


DETAIL B
SCALE 12:1

Tip section detail
Sheet scale 2:1



.0024⁺.0004
-.0000



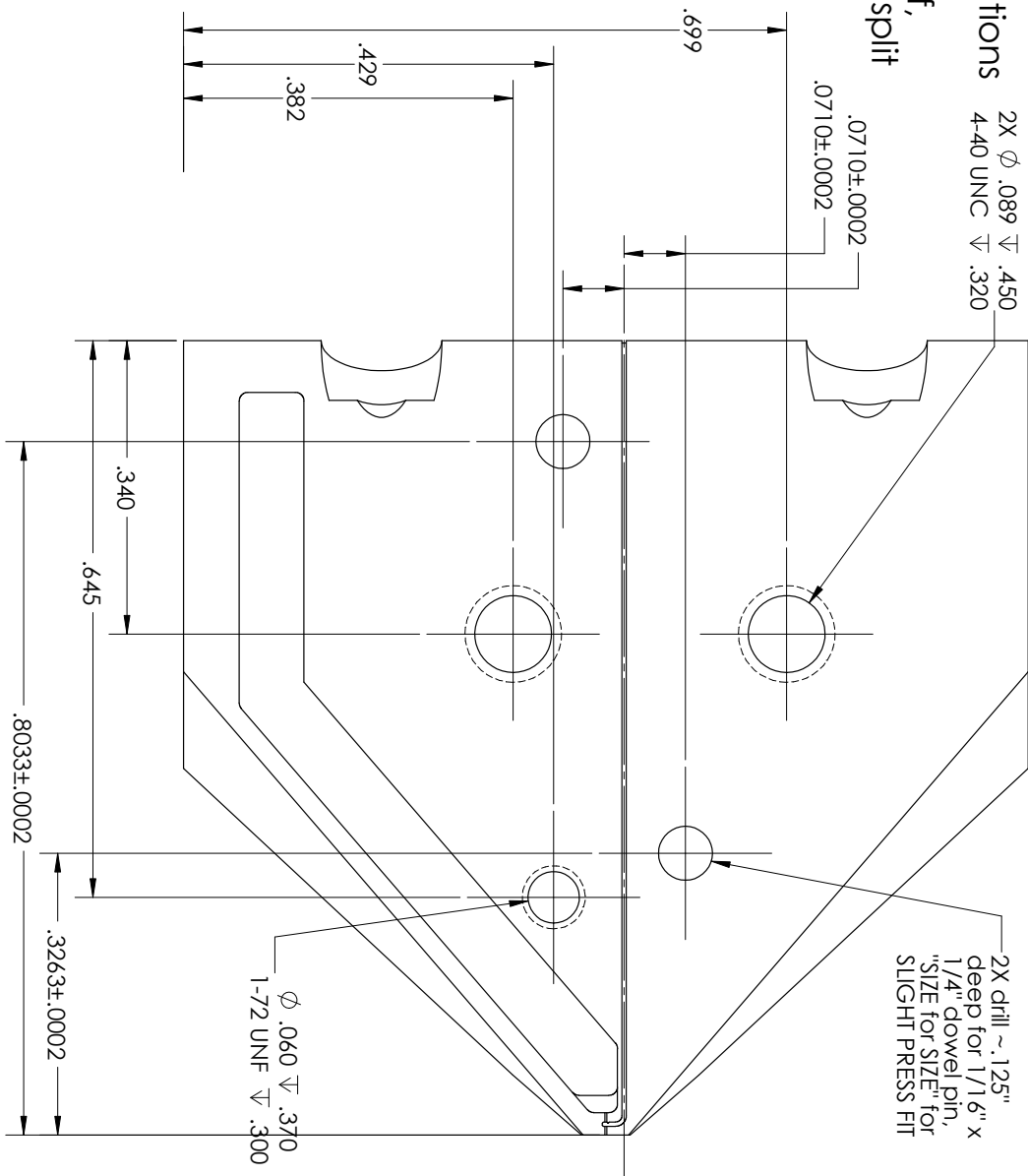
Bottom hole locations

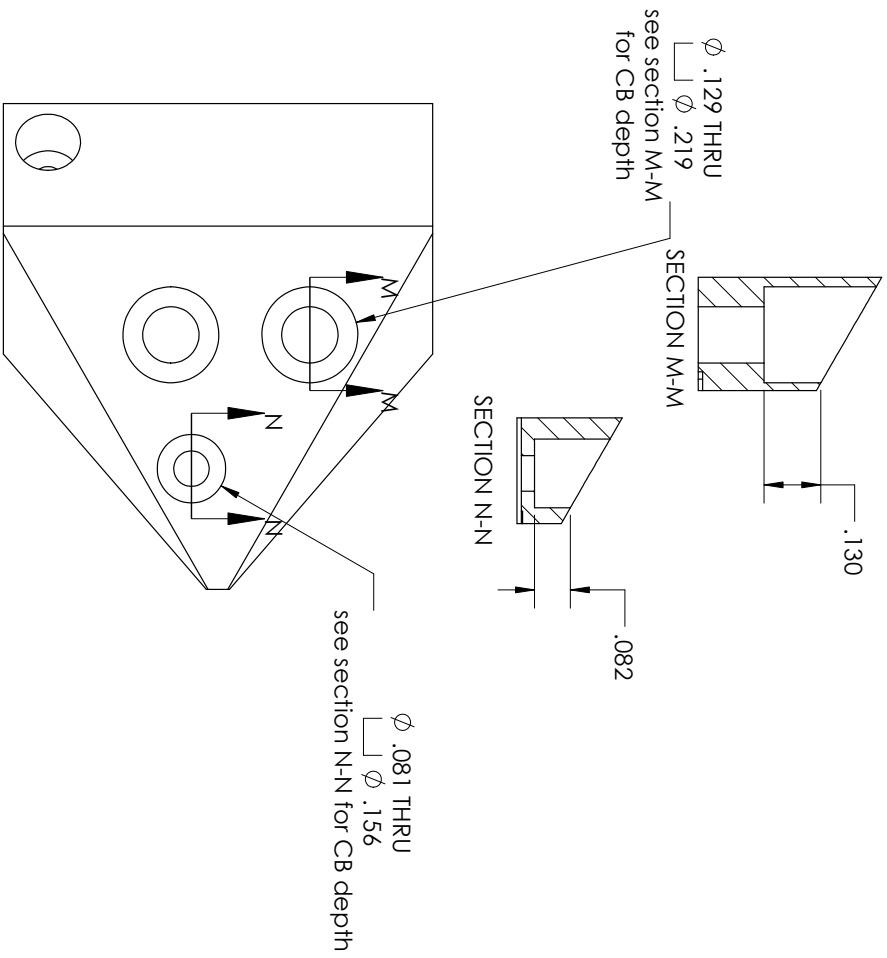
2X ϕ .089 ∇ .450
4-40 UNC ∇ .320

View: Bottom half,
looking down on split
plane

All tolerances
 \pm .009 unless
otherwise noted

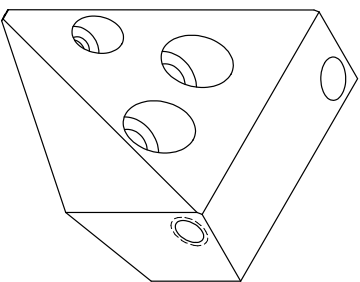
Sheet scale 6:1

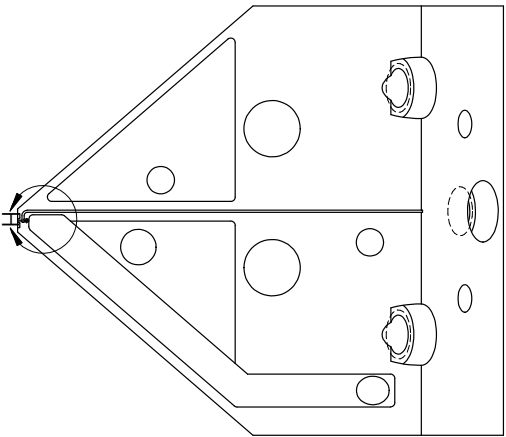




Counterbore and
 clearance hole detail
 All tolerances $\pm .009$
 unless otherwise
 noted

Sheet scale 3:1



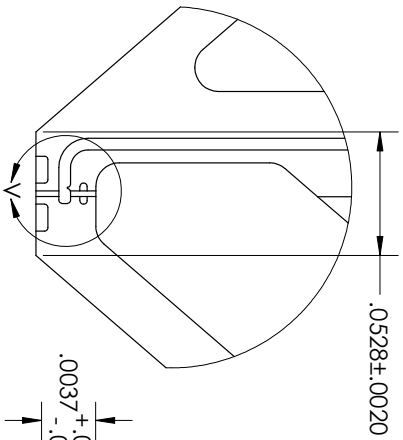


Top channel/waveguide detail
View: Top half, looking down on split plane

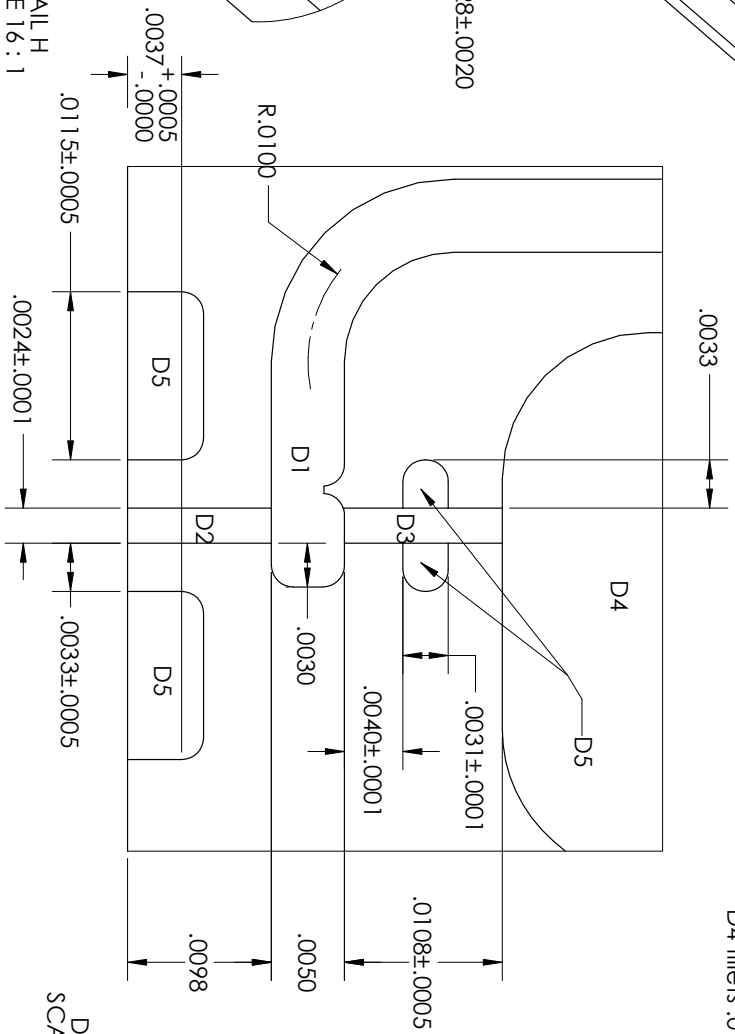
All tolerances $\pm .0002$ unless otherwise noted

Sheet scale 3:1

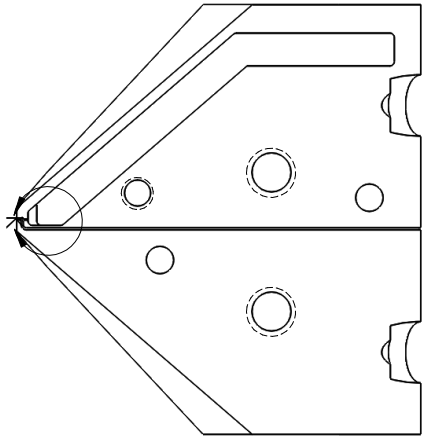
DEPTHS
 D1 - .0050
 D2 - .0012 \pm .0001
 D3 - .0010 \pm .0001
 D4 - .0128 \pm .0005
 D5 - .0006 \pm .0001
 D1, D5 fillets .0015
 D4 fillets .01



DETAIL H
SCALE 16:1



DETAIL V
SCALE 100:1

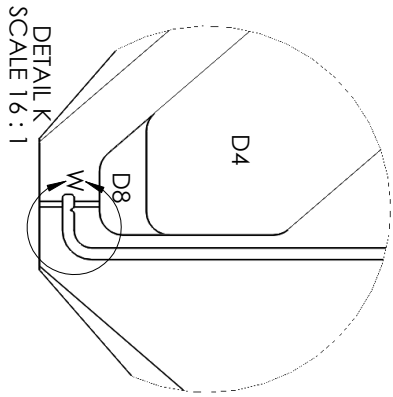


Bottom channel/waveguide detail
View: Bottom half, looking down on split plane

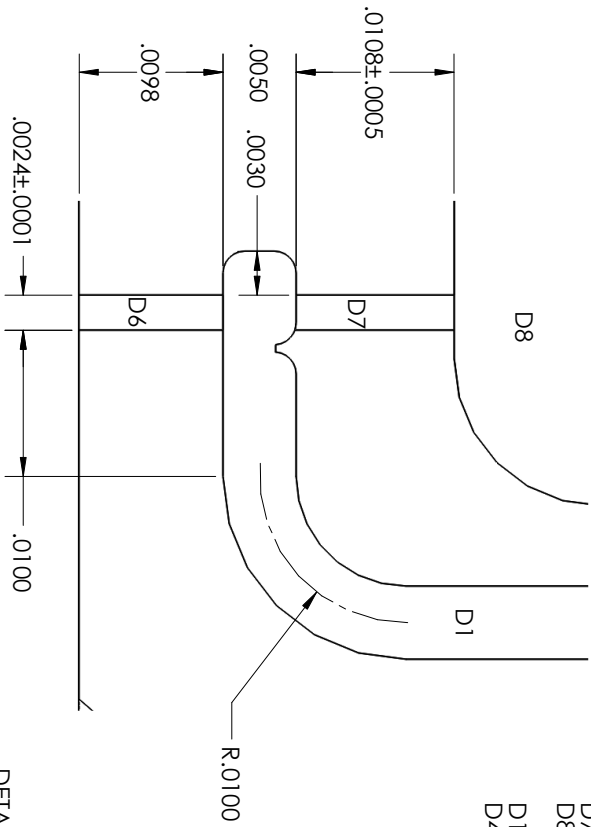
All tolerances $\pm .0002$ unless otherwise noted
Sheet scale 3:1

- DEPTHS
- D1 - .0050
 - D4 - .0128 $\pm .0005$
 - D6 - .0006 $\pm .0001$
 - D7 - .0004 $\pm .0001$
 - D8 - .0054 $\pm .0005$

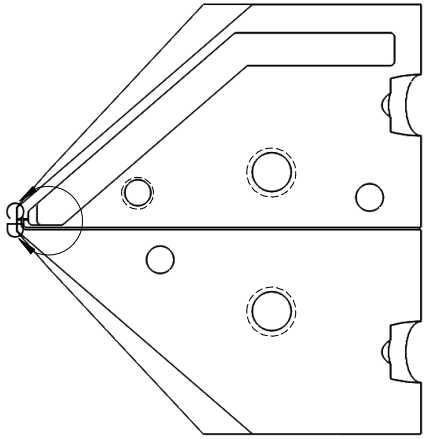
- D1 fillets .0015
- D4, D8 fillets .01



DETAIL K
SCALE 16 : 1

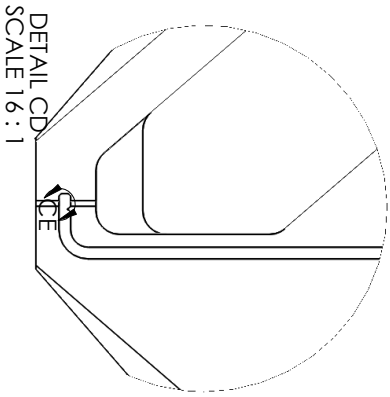


DETAIL W
SCALE 100 : 1

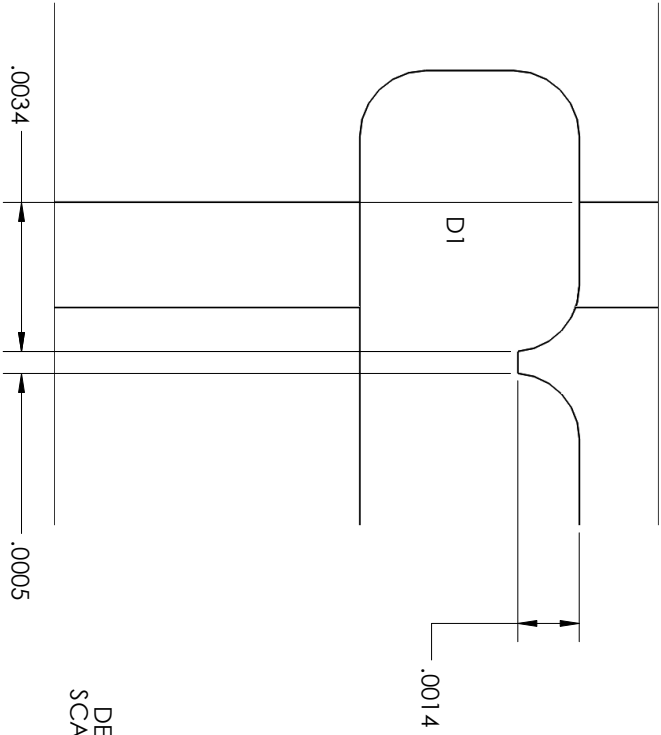


Capacitive step detail
View: Bottom half, looking down on split plane

All tolerances $\pm .0002$ unless otherwise noted
Sheet scale 3:1

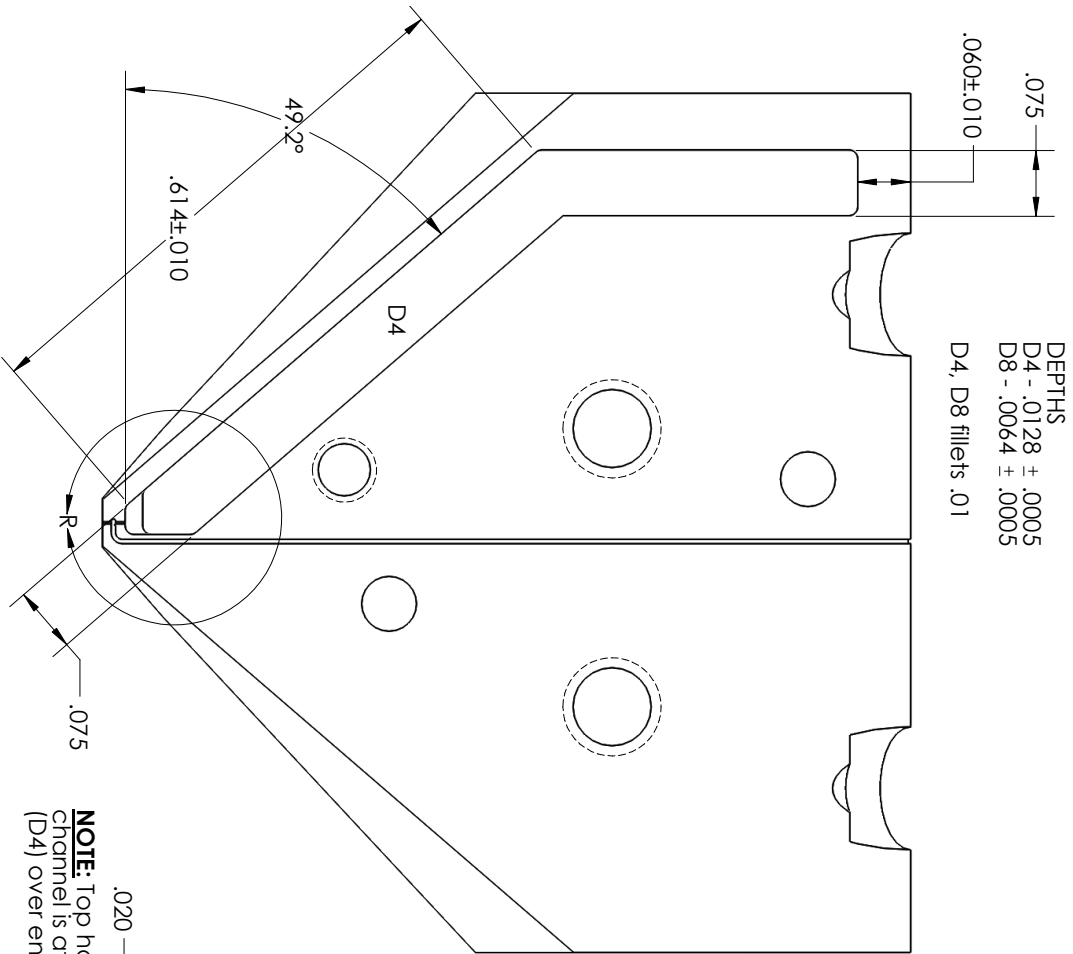


DETAIL CD
SCALE 16:1



DETAIL CE
SCALE 300:1

DEPTH D1 - .0005
D1 fillets .0015

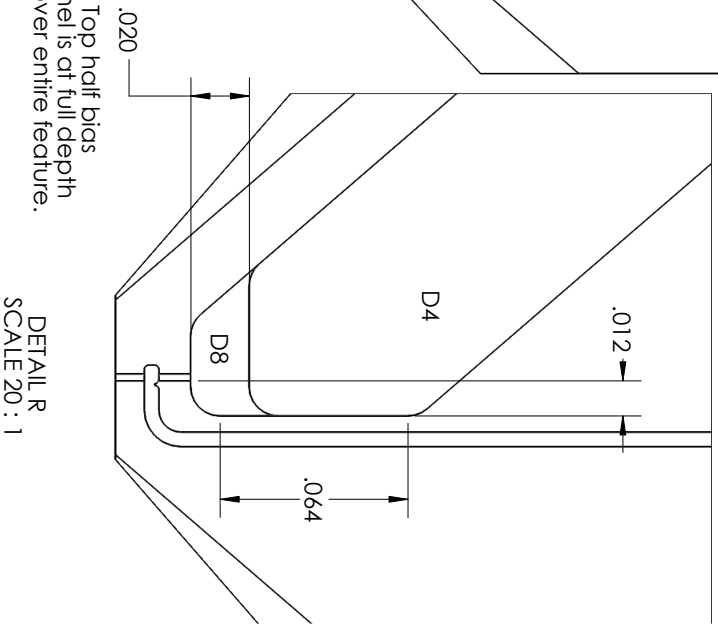


DEPTHS
 D4 - .0128 ± .0005
 D8 - .0064 ± .0005
 D4, D8 fillets .01

Bias channel detail
 View: Bottom half,
 looking down on
 split plane

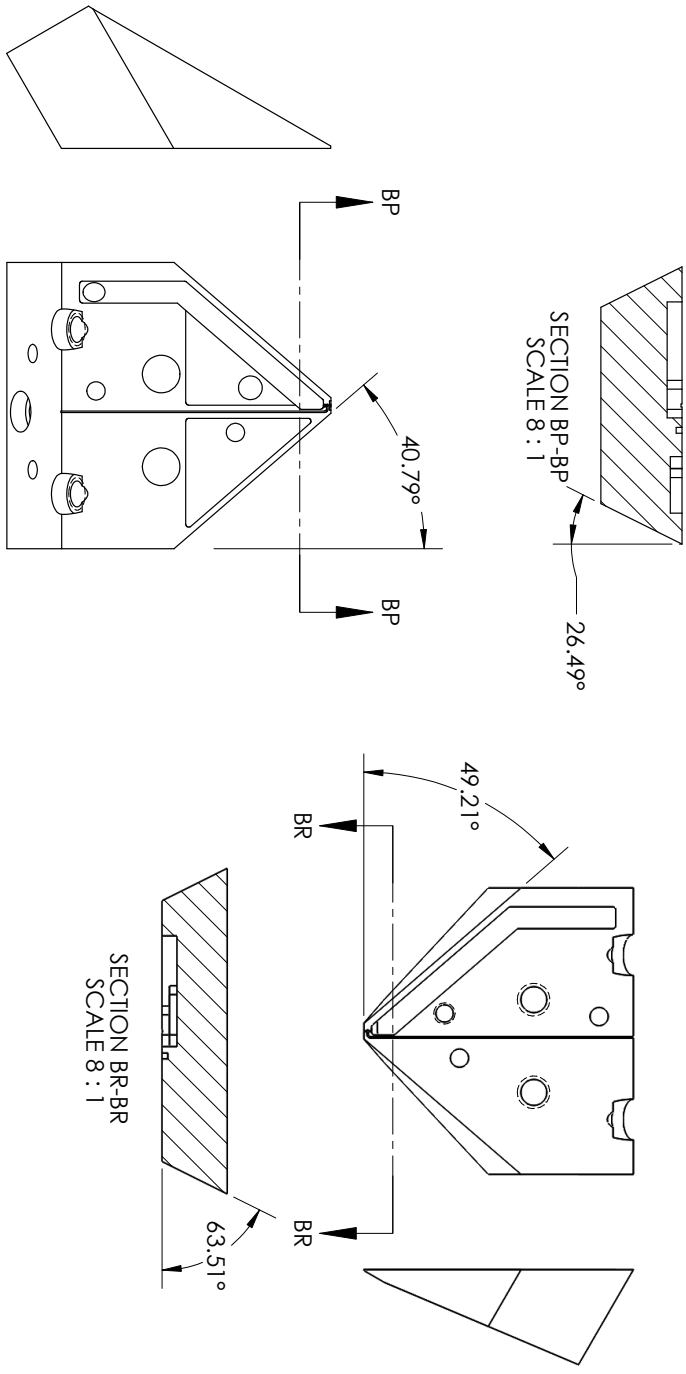
All tolerances ±.001
 unless otherwise noted
 Sheet scale 6:1

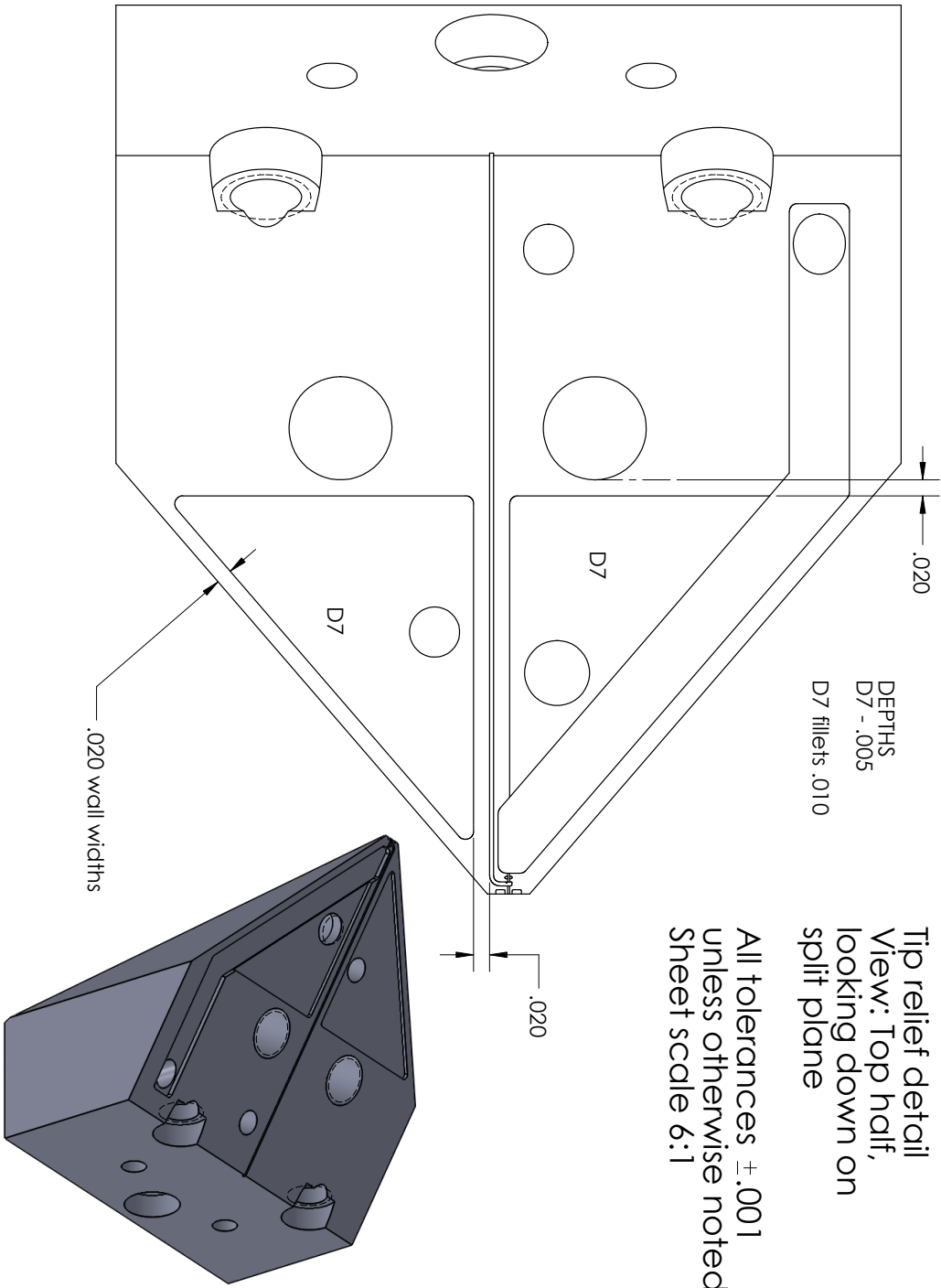
NOTE: Top half bias
 channel is at full depth
 (D4) over entire feature.



DETAIL R
 SCALE 20 : 1

Angled face cut detail
Sheet scale 2:1





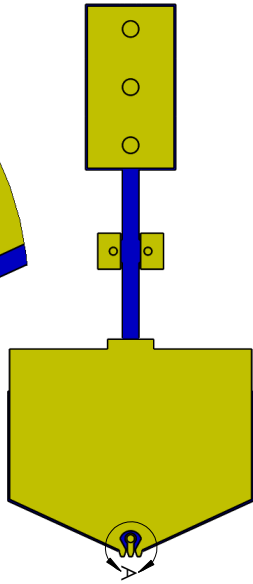
Appendix C

WR-1.0-Microstrip-Design

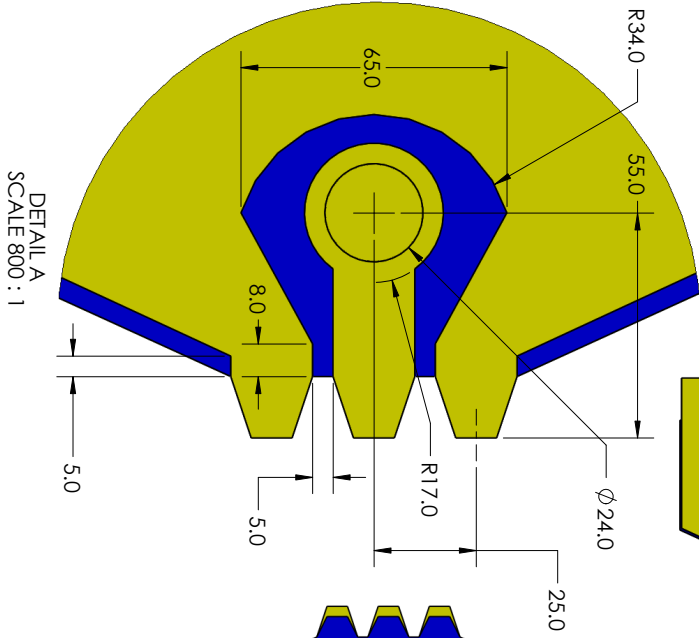
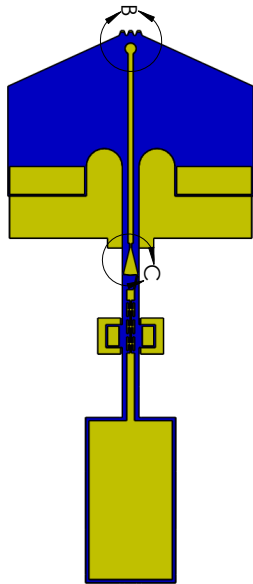
The following drawing illustrates the RF design dimensions unique to the microstrip design.

WR-1.0 MICROSTRIP DESIGN

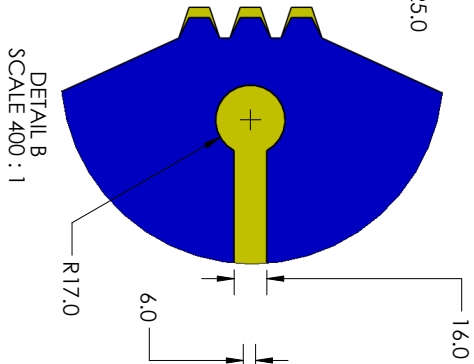
FRONTSIDE



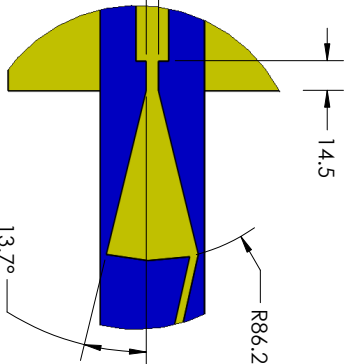
BACKSIDE



DETAIL A
SCALE 800 : 1



DETAIL B
SCALE 400 : 1



DETAIL C
SCALE 400 : 1

This drawing illustrates the WR-1.0 RF design dimensions unique to the microstrip design. All dimensions listed in microns.